

**THE EFFECT OF BIOMASS PARTICLE SIZE ON PRODUCT DISTRIBUTION OF THE HYDROTHERMAL LIQUEFACTION OF PINE WOOD**

A Major Qualifying Project Report:

Submitted to the Faculty

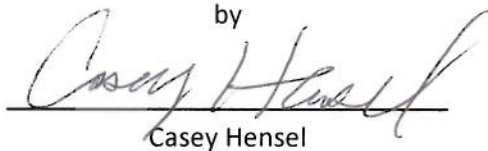
of the

WORCESTER POLYTECHNIC INSTITUTE

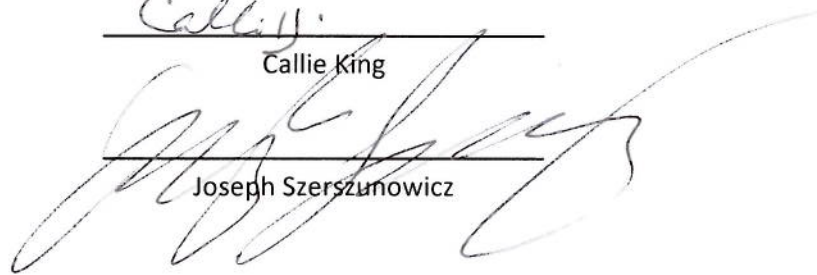
In partial fulfillment of the requirements for the

Degree of Bachelor of Science in Chemical Engineering

by

  
Casey Hensel

  
Callie King

  
Joseph Szerszunowicz

Date: March 7<sup>th</sup>, 2014

Approved:

  
Prof. Michael T. Timko, Major Advisor

1. Hydrothermal Liquefaction
2. Pine
3. Particle Size

  
Prof. Aaron N. Deskins, Co-Advisor

## Table of Contents

Acknowledgments.....	iv
Abstract.....	v
Table of Figures.....	vi
Table of Tables.....	viii
1. Introduction.....	1
2. Background.....	3
2.1 Hydrothermal Liquefaction Process.....	3
2.2 Role of Water in the HTL Process.....	4
2.3 Biomass Feedstock.....	5
2.3.1 Cellulose.....	5
2.3.2 Hemicellulose.....	6
2.3.3 Lignin.....	7
2.4 Key Reaction Pathways.....	8
2.4.1 Cellulose Decomposition.....	8
2.4.2 Lignin Decomposition.....	13
2.4.3 Hemicellulose Decomposition.....	14
2.5 Modeling Key Reactions of the HTL Process.....	14
2.6 Optimum Conditions for Bio-oil Yield.....	16
2.6.1 Residence Time.....	16
2.6.2 Temperature and Pressure.....	17
2.6.3 Heating Rate.....	17
2.6.4 Particle Size.....	17
2.7 Previous Methods, Biomasses, and Analysis Techniques.....	18
3. Experimental.....	20
3.1 Equipment.....	20
3.1.1 Reactor.....	20
3.1.2 HPLC.....	21
3.1.3 Rotary Evaporator.....	21
3.2. Procedure and Analytical Technique.....	22
3.2.1 Feed Stock Preparation.....	23

3.2.2	Converting Biomass .....	23
3.2.3	Sample Retrieval and Analyzing Product .....	24
3.2.4	HPLC Methodology .....	24
3.2.5	FT-IR Methodology.....	25
3.2.6	Raman Methodology.....	25
3.2.7	Total Organic Carbon Analysis Methodology.....	25
3.2.8	Modeling Thermochemistry.....	26
5.	Results and Discussion .....	27
5.1	Physical Observations and Mass Balance .....	27
5.2	HPLC, UV/Vis, and ELSD Analysis .....	33
5.3	FT-IR Analysis .....	39
5.4	Raman Analysis .....	43
5.5	Total Organic Carbon Analysis .....	45
5.6	Computations.....	48
5.7	Final Discussion and Considerations .....	51
6.	Conclusions .....	55
7.	Recommendations .....	56
8.	References .....	57
9.	Appendices.....	61
9.1	Appendix A: Additional Tables and Figures .....	61
9.1.1	FT-IR Spectrums .....	61
9.1.2	Final Molecule Geometries.....	64
9.1.3	Raw Liquid HPLC Chromatograms.....	71
9.1.4	Concentrated Liquid HPLC Chromatograms .....	77

## **Acknowledgments**

We would like to begin by thanking our advisors, Professor Michael Timko and Professor Aaron Deskins, Department of Chemical Engineering at Worcester Polytechnic Institute, for giving us the opportunity to work on this project. They have supported our efforts throughout the duration of this MQP and allowed us to guide the fate of the project.

We appreciate the guidance and moral support we received by Geoff Tompsett and Alex Maag. Their previous research and laboratory techniques were extremely helpful in guiding us towards our objectives and laboratory methodology. Our work would not have gone as smoothly without their assistance.

We would also like to thank Andrew Butler and Professor Jeanine Plummer for assisting in the analysis of our products. Lastly, thank you Huyen Vu for assisting us in standard development.

## Abstract

Hydrothermal liquefaction (HTL) of pine wood was studied in a batch setting to understand the effects of particle size on bio-oil yield and compound distribution. It was expected that mass transfer limitations would decrease with decreasing particle sizes, leading to greater yields and full biomass conversion. Pine wood milled to 106-150  $\mu\text{m}$ , 212-300  $\mu\text{m}$ , and 1680-2000  $\mu\text{m}$  particle sizes were fed to a 500 mL Parr reactor with a pine to water ratio of 1:10 by weight. The reactor and contents were heated to 300  $^{\circ}\text{C}$  and approximately 1500 psig at a heating rate varying between 3.5-4.5  $^{\circ}\text{C}/\text{min}$ . The reactor and contents were left to cool immediately after reaching target temperature. The liquid product was filtered and solid products were washed with acetone and dried. Liquid product carbon concentration was determined using a Total Organic Carbon (TOC) analyzer. Liquid product was rotary evaporated and the concentrated products were analyzed using a High Pressure Liquid Chromatograph (HPLC) with a UV/Vis detector and Evaporating Light Scattering Detector (ELSD). Solid products were analyzed using both Raman spectroscopy and Fourier Transform Infrared spectroscopy (FT-IR). Computational methods were investigated to identify levels of theory suitable for quickly approximating key reactions in the HTL process. Analysis of concentrated liquid products revealed that the solution was comprised mostly of C3-C6 sugars, 5-HMF, and furfural. A comparison of HPLC chromatograms between different particle sizes indicated that there were insignificant differences between them. FT-IR and Raman spectrums revealed that solid products left from the hydrothermal liquefaction of pine were composed mostly of lignin structures. Particle size has a negligible effect on product yield and compound distribution within the parameters studied. Under these conditions, all saccharides appear to depolymerize. B3LYP 6-31G\* and Hartree-Fock 6-31G\* were identified as the most suitable computational theories for approximating key reactions in the hydrothermal liquefaction of wood. However, reaction energies involving larger sugar molecules like glucose and fructose are very sensitive to model geometry and can easily result in incorrect energies.

## Table of Figures

Figure 1: Hydrothermal Liquefaction Process Adapted from Peterson (Peterson, 2011) .....	3
Figure 2: A Typical Cellulose Chain Adapted from Pandey (Pandey, 1999) .....	6
Figure 3: Examples of Hydroxyl Group Differences in $\alpha$ and $\beta$ Glucose Rings .....	6
Figure 4: One Example of a Typical Hemicellulose Structure Adapted from Pandey (Pandey, 1999).....	7
Figure 5: One possibility of lignin content adapted from Glazer (Glazer, 1995) .....	8
Figure 6: Reaction Pathway for Cellulose Decomposition Adapted from Sasaki (Sasaki, 1998) .....	9
Figure 7: Proposed Reaction Mechanism of Microcrystalline Cellulose in Supercritical Water. (1) Swelled (or Dissolved) Cellulose, (2) Cellooligosaccharides, (3) Glucose, (4) Erythrose, (5) Glycolaldehyde, (6) Fructose, (7) Glyceraldehyde, (8) Dihydroxyacetone, (9) Pyruvaldehyde, (10) 5-HMF, (11) 2-Furfural, (12) Glucopyranosyl-erythrose, (13) Glucopyranosyl-glycolaldehyde, (14) Anhydro-cellooligosaccharides, and (15) Levoglucosan. (Matsumura, 2006) .....	11
Figure 8: Detailed Glucose Decomposition Adapted from Aida (Aida, 2007).....	12
Figure 9: Lignin Decomposition Adapted from Liu (Liu, 2006) .....	13
Figure 10: Reaction Mechanism of the Degradation of Xylose Adapted from Aida (Aida, 2010) .....	14
Figure 11: Reactor Set Up .....	20
Figure 12: Experimental and Analytical Procedure.....	22
Figure 13: Feed Stock Particle Size.....	23
Figure 14: Bio-char from Three Different Particle Sizes; Top Left 106-150 $\mu\text{m}$ ; Top Right 212-300 $\mu\text{m}$ ; Bottom 1680-2000 $\mu\text{m}$ .....	28
Figure 15: Liquid Products; Left Raw Liquid Product; Middle Concentrated Liquid from Rotary Evaporator; Left Evaporated Liquid from Rotary Evaporator .....	29
Figure 16: Mass of Liquids and Solids Directly Measured. Mass of Material Lost, Unaccounted for, or Produced as Gas. Reactor was Initially Filled with 100g of Water and 10g of Biomass. ....	30
Figure 17: Percentage Weight of Initial Biomass Feed Converted into Different Phases of Product with Error Bars .....	31
Figure 18: Plot Showing Temperature of Reactor over Time .....	32
Figure 19: ELSD Chromatograms of Sugars: Cellobiose, Glucose, Xylose, and Fructose each of 0.05 Wt % in Water. ....	34
Figure 20: UV/Vis Chromatograms of 0.05 Wt % 5-HMF and Furfural in Water.....	34
Figure 21: ELSD Chromatogram for the Bio-oil Produced by 1680-2000 $\mu\text{m}$ #1 Pine Particles.....	35
Figure 22: ELSD Chromatogram for the Bio-oil Produced by 1680-2000 $\mu\text{m}$ #1 Pine Particles Zoomed ...	36
Figure 23: UV/Vis Chromatogram of Concentrated Bio-oil Produced from 1680-2000 $\mu\text{m}$ #1 Pine Particles .....	37
Figure 24: Plot of Overlapped ELSD Chromatograms Produced for each Particle Size .....	38
Figure 25: HPLC Chromatogram Comparing Degradation of Samples .....	39
Figure 26: FT-IR Spectrum of Two Separate 212-300 $\mu\text{m}$ Experiments with Normalized Baseline.....	40
Figure 27: FT-IR Spectrum Overlapped for Each Particle Size and Raw Pine wood.....	41
Figure 28: Raman Spectra for Bio Char of all Particle Sizes and Runs .....	44
Figure 29: Carbon Concentration of Raw Filtered Liquid Removed from Reactor upon Experiment Completion.....	46

Figure 30: Carbon Concentration of Bio-oil Produced from Pine Wood .....	47
Figure 31: TOC Concentration Compared to Heating Rate when the Reactor Temperature was Increasing Above 200 °C.....	48
Figure 32: Six Reactions Modeled Using Various Levels of Theory.....	49
Figure 33: Enthalpy Landscape Diagram Comparing Calculation Methods for Glucose to Fructose Isomerization and Fructose to 5-HMF .....	50

## Table of Tables

Table 1: Enthalpies and Free Energies Calculated for Several Reactions Using the G4 method.....	15
Table 2: Literature Summary of HTL Processes .....	19
Table 3: Hydrothermal Liquefaction Reaction Parameters .....	23
Table 4: Chemicals and Weight Percentages in Water Used for Standard Solution Development. All standards were injected using an injection volume of 30 $\mu$ L .....	25
Table 5: Outline of Overall Average Heating Rate (HR Overall), Average Heating Rate While the Reactor Temperature was Increasing Above 200 $^{\circ}$ C (HR Above 200 $^{\circ}$ C), and Residence Time While the Reactor was Above 200 $^{\circ}$ C (RT Above 200 $^{\circ}$ C) for each Experiment.....	32
Table 6: FT-IR spectra of bio-char (Byrd, 2014) .....	42
Table 7: Particle Size and Intensity Ratio .....	45
Table 8: Energies Calculated for 2 Reactions Compared to the Same Reactions Modeled Using the G4 Theory. $\Delta E(e)$ Represents Total Electronic Energy, $\Delta E(0)$ Represents Reaction Energy Changes with Zero Point Energy Included, $\Delta H(298K)$ Represents Reaction Enthalpy at 298K, and $\Delta G(298K)$ Represents Free Energy Changes at 298K. Reaction 1 is the Glucose to Fructose Isomerization. Reaction 2 is the Reaction of Fructose to 5-HMF.....	49
Table 9: Energies Calculated for 3 Reactions Compared to the Same Reactions Modeled Using the G4 Theory. $\Delta H(298K)$ Represents Reaction Enthalpy at 298K, and $\Delta G(298K)$ Represents Free Energy Changes at 298K. Reaction 3 is the Conversion of Glucose to Erythrose and Glycolaldehyde. Reaction 4 is the Conversion of Fructose to Glyceraldehyde and Dihydroxyacetone. Reaction 5 is the Conversion of Glyceraldehyde to Pyruvaldehyde and Water.....	51
Table 10: Energies Calculated for Reaction 6, the Conversion of Xylose to Furfural and Water. $\Delta E(e)$ Represents Total Electronic Energy, $\Delta E(0)$ Represents Reaction Energy Changes with Zero Point Energy Included, $\Delta H(298K)$ Represents Reaction Enthalpy at 298K, and $\Delta G(298K)$ Represents Free Energy Changes at 298K. Calculated Energies Are Compared to Calculated Reaction Energy from Nimlos et al..	51

## 1. Introduction

With the world demand for energy expected to double between 2000 and 2050, the research and development for implementing reliable second-generation bio-fuel energy sources has increased, since petroleum reserves are diminishing (Lange, 2007). An advantageous option to pursue is renewable energy due to the resulting decrease of CO<sub>2</sub> emissions compared to fossil fuels, and an overabundance of resources. As a result, scientists and engineers have been developing technologies to use various energy sources including hydroelectric, solar, wind, and biomass (Lange, 2007). Since a single replacement for fossil fuels is unlikely, each option must be studied. Additionally, for any of these second-generation possibilities to be scaled up and implemented, tradeoffs would need to be made whether the tradeoff is affordability, land accessibility, or social stability (Lange, 2007).

Focusing on biomasses as an alternative, wood is of particular interest since its cell walls are composed of lignocellulose which includes cellulose (45-50%), hemicellulose (25-35%), and lignin (25-35%) (Malherbe, 2013). The breakdown of lignocellulose proceeds by multiple reactions, the selectivity of which is dependent upon the parameters of the reaction. Most importantly are the degradation of cellulose and hemicellulose, which represent approximately three quarters of the lignocellulose by weight. When depolymerized and deoxygenated, the fermentable sugars from cellulose and hemicellulose are released and can be collected as bio-oil, which can be further processed for bio-fuel (Lange, 2007). Unlike cellulose and hemicellulose, lignin does not produce sugars, and due to the lignocellulose structure, it interferes with easily isolating the cellulose and hemicellulose. Consequently, many treatments have been studied in order to identify the most effective method of lignocellulose degradation in terms of cost, manufacturability, and product quality (Peterson, 2008).

Conversion of wood biomass into an energy source can be primarily broken up into pyrolysis and hydrothermal treatment. Specifically hydrothermal liquefaction, as the name implies, allows water to be used as the solvent. Water is considered an ideal solvent because it is abundant, environmentally safe, and possesses the ability to act as a catalyst as it approaches its critical temperature. As water is heated to near-critical conditions, the dielectric constant lowers and the ionization constant increases, allowing water to dissolve organic compounds and provide an acidic medium for hydrolysis reactions (Kumar, 2010). Additionally, using water implies that wet biomass materials can be used, as opposed to having an added costly operation of drying the biomass, like the case with pyrolysis. Pyrolysis is a biomass conversion process that takes place without a solvent medium and without the presence of oxygen. Pyrolysis typically occurs at higher temperatures than hydrothermal liquefaction.

In hydrothermal liquefaction many types of wood under different operational parameters have been studied by varying particle size, biomass feed to solvent ratio, reactor temperature, and heat up rate. Adjusting the conditions led to different process conversion efficiencies (Mosteiro-Romero, 2014). Intuitively, utilizing smaller particle sizes for biomass feed would lower mass

transfer limitations due to increased surface area. This would then lead to complete conversion of biomass. Hydrothermal liquefaction is thought to undergo several reactions with many intermediate steps. It is possible then, that larger feed particles may inhibit the full conversion of biomass leading to loss of product. However, utilizing smaller particles means there is a significant added cost of reducing the particle size of the feed by grinding or milling. It is important to understand to what extent particle size influences product yield and compound distribution. To better understand the experimental products and reaction pathways, computational models can be performed hand-in-hand to identify the most favorable products and mechanisms.

The objective of this project was to study the effect particle size of pine wood has on the product phase distribution and compound distribution through hydrothermal liquefaction batch experiments. Particle sizes studied included 106-150  $\mu\text{m}$ , 212-300  $\mu\text{m}$ , and 1680-2000  $\mu\text{m}$  which were placed in a 500 mL Parr reactor and heated to sub-critical water conditions at a temperature of 300°C. Pine was selected as it is abundant softwood in the northern hemisphere, (Cheng, 2001). Alongside the experimental study, computational models within the WebMO interface were used to study the predominant reactions. Specifically, the thermochemistry of key reactions was modeled using different levels of theory and was compared to literature values. A modeling theory suitable for quickly approximating the energetics of reactions was identified.

## 2. Background

### 2.1 Hydrothermal Liquefaction Process

The hydrothermal liquefaction (HTL) process is able to use a variety of biomass feedstocks or organic materials in a reactor under relatively mild temperature (200-400 °C) and high pressure (100-200 atm) conditions, compared to pyrolysis which can be performed from 400-600 °C (Lange, 2007), (Sanna, 2013). Once the hydrolysis temperature and pressure conditions are achieved in the vessel, the reactions occur to give desirable products of high energy density bio-oil or bio-crude (Faeth, 2013). Solid bio-char is also a product of the HTL process. Bio-oil has an energy density approximately two times higher than that of the wood feedstock, 35-37 MJ/kg and 18-23 MJ/kg, respectively (Vardon, 2012). The concept behind HTL is that the water and biomass are heated until water reaches conditions where it can act like a solvent, reactant, and catalyst for the system.

To achieve maximum quantity of high energy bio-oil, the process must be optimized in a laboratory setting studying both batch and continuous processes, as continuous would be ideal for large scale production. In batch processes, typical bio-oil yields range from 40-70% by mass of initial feedstock, depending on the reaction parameters (Mosteiro-Romero, 2014). To show the general overview of the HTL process, Figure 1 is displayed below.

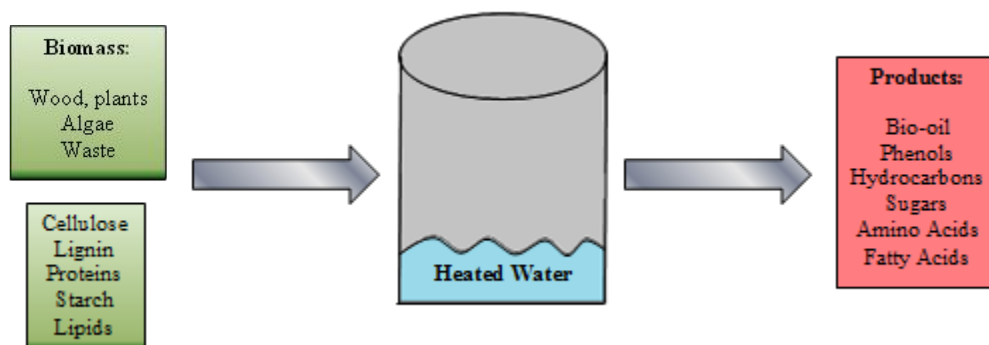


**Figure 1: Hydrothermal Liquefaction Process Adapted from Peterson (Peterson, 2011)**

Many benefits of the HTL process exist, making it worthy of further investigation. Unlike other processes, HTL accepts dry and liquid biomass. This is advantageous since it eliminates the need for a drying stage, as pyrolysis requires, which is very time and energy consuming, and therefore cost efficient for HTL. Algae, waste, and wood are just a few examples of the variety of what has been studied thus far (Faeth, 2013), (Smith), (Monsteiro-Romero, 2014). The process has potential to produce high quantities of bio-oils at high energy densities between 35-37 MJ/kg (Vardon, 2012). Also bio-char has an energy density of 28 MJ/kg, compared to coal at 28-40 MJ/kg, making the HTL process an attractive option (Kumar, 2010), (Anderson, 2013). The output of the system will also exclude any bacteria or viruses due to the high temperature of the

reaction. The process is also environmentally friendly. Using water as a catalyst eliminates the need for harmful chemicals, since the water can be recovered and recycled back through the system. Lastly, having the HTL process produce bio-oil directly makes storage simple after production. The bio-oil can either be used as it was produced, or existing refinery technology can upgrade it thermally to obtain diesel, gasoline, or jet fuel (Aarhus University, 2013).

The HTL process brings multiple challenges which must be further studied. First, while the bio-oil is being produced, there are many unknown and uncharacterized reaction pathways and kinetics occurring simultaneously. Reaction pathways differ based on the specific biomass injected into the reactor, which lead to a variety of products. These products include acids and sugars in the bio-oil which would need to be further refined prior to commercial use (Mosteiro-Romero, 2014). With this, a second disadvantage of this process is the scale up. To date, many laboratory experiments at universities and industries have been performed on small pilot scales, primarily with batch, stirred batch, semi-continuous, and tubular continuous reactors (Mosteiro-Romero, 2014). But, no full size manufacturing plant exists. Therefore the large scale process conditions and costs are currently estimated, and may be inaccurate. This uncertainty is due to the process still being developed. For example, high pressures in HTL are necessary, and thus, safety concerns require equipment that can handle the high pressure. Consequently, the designed equipment will be high in cost. This same concept also holds true for technology that must be developed which will process and separate the products. There are other cost concerns such as equipment handling the high temperatures, waste water disposal, land, and storage. In conclusion, this leaves the overall cost highly variable, and currently unreliable (Smith).

## 2.2 Role of Water in the HTL Process

In the HTL process, water plays a critical role as the solvent, reactant, and catalyst for the system (Zhang, 2010). Under standard conditions, water is a polar solvent with a dielectric constant of 78.5. However, heating the water to 300 °C, as performed in this study, changes the water's properties as it is approaching its critical point (374 °C). With heating, the dielectric constant rapidly decreases, resulting in the water molecules behaving more like a nonpolar liquid (Kumar, 2010). This means that the water solubilizes most organic compounds and oxygen. Additionally, the auto-dissociation of water increases quickly with the increase in temperature. Chemically, the hydrogen bonding is weakening so that dissociation occurs, splitting water into  $\text{H}_3\text{O}^+$  and  $\text{OH}^-$  ions. Therefore, the rates of acid and base-catalyzed decomposition reactions are increased significantly due to the increase in temperature (Zhang, 2010).

In bio-oil production, one main objective is to reduce the composition of oxygen from the original source of biomass, which typically accounts for 40-60 wt% of the dried biomass feedstock (Peterson, 2008). The purpose of this is for improving the biomass energy density, which has been shown to increase to two times that of the biomass feedstock when converted to bio-oil (Vardon, 2012). In the presence of water at elevated temperature and pressure, oxygen is removed via dehydration and decarboxylation. Dehydration removes oxygen in the form of

water, which is ideal since it leads to a greater carbon yield of biofuel per biomass. This dehydration is predominately noticeable with longer reaction times in the HTL process (Kumar, 2010). Decarboxylation removes oxygen as carbon dioxide. This allows the bio-oil product to increase the hydrogen to carbon ratio. Removing oxygen via water or carbon dioxide is ideal since neither cause a loss in the heating value. The HTL process enhances oxygen removal, typically leaving the bio-oil product with less than 1 wt % oxygen (Peterson, 2008).

## 2.3 Biomass Feedstock

The pine sawdust feedstock is a natural and abundant renewable biomass feedstock that is a common byproduct from other processes (mills, lumber, construction, etc.). Wood biomass as well as other plant matter biomass is composed of lignocellulose. Lignocellulose is made up of a combination of carbohydrate polymers (cellulose and hemicellulose) and aromatic polymers (lignin). In order to generate bio-fuels, lignocellulose must be broken down to access the carbohydrate polymers contained within its structure (Akhtar, 2011). The desired products are the simple sugars that compose the cellulose and hemicellulose carbohydrate structures, such as glucose. Glucose, a monosaccharide, is a key unit in the chemical structure of cellulose and hemicellulose provided in woods and other biomasses. This simple sugar can be readily fermented to create ethanol which can then be used as a fuel source (Lange, 2007). Glucose is the most abundant sugar due to the high cellulosic content in lignocellulose biomasses. The ethanol yield from glucose is greater than other more complex sugars. These two factors make glucose the ideal option for ethanol synthesis from lignocellulose feedstock. The challenge present in isolating the glucose is breaking down the extremely uniform cellulose networks. The uniformity of cellulose makes the process of hydrolyzing the networked bonds very difficult (Kumar, 2010).

Lignocellulose is composed of three networks; lignin, hemicellulose, and cellulose (Malherbe, 2013). The amounts of each vary depending on the raw material being used as biomass. For soft woods, like pine wood, the lignin, hemicellulose, and cellulose compositions are 25-30%, 25-35%, and 45-50% by weight respectively (Malherbe, 2013). The actual structure and network of these polysaccharides and aromatics determines how well they can be hydrolyzed. Breaking these structures down produces simple sugars such as glucose and xylose which can be converted into a liquid fuel source with an energy density similar to gasoline and diesel fuel products.

### 2.3.1 Cellulose

The importance of cellulose lies in its massive quantity of glucose molecules within its structure. Cellulose is composed of chains of  $\beta$ -D-glucose rings, as shown below in Figure 2.

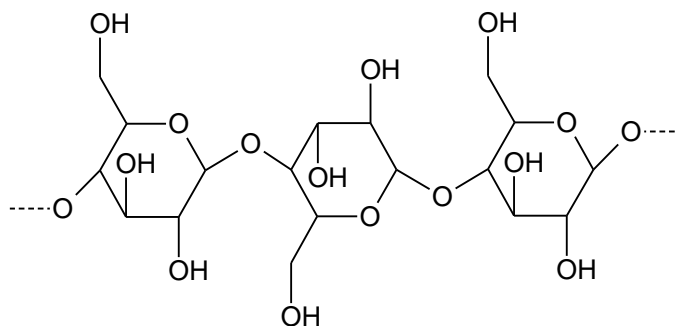


**Figure 2: A Typical Cellulose Chain Adapted from Pandey (Pandey, 1999)**

This is different from the  $\alpha$  ring formation by the orientation of the hydroxyl at the 1 and 4 carbon sites along the ring. The  $\beta$  ring has opposite hydroxyl groups, while in the  $\alpha$  formation these groups are facing the same direction, as seen in Figure 3.

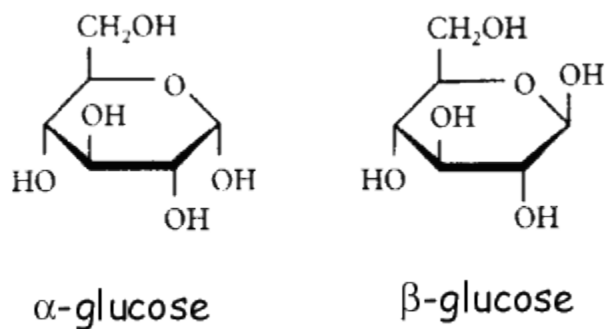


**Figure 3: Examples of Hydroxyl Group Differences in  $\alpha$  and  $\beta$  Glucose Rings**

This is important because a chain of  $\alpha$ -D-glucose rings form starch, a material which is easily enzymatically broken down, whereas  $\beta$ -D-glucose rings form cellulose which is a much more resilient compound. This is why cellulose is found to hold structures of cell walls in plants.

### 2.3.2 Hemicellulose

Hemicellulose is chemically related to cellulose by the trait of having the same  $\beta$ -D-glucose ring backbone. However, hemicellulose is a heterogeneous polymer and is comprised of other sugars. Hemicellulose is made of many C5 and C6 sugars (pentoses and hexoses) such as xylan, xyloglucan, mannans, and glucomannans. Hemicellulose is a very low polymerized compound and is highly amorphous in shape, as shown below in Figure 4 (Scheller, 2013). Unlike the straight and symmetric chains of cellulose, hemicellulose is branched and not uniform making it more susceptible for hydrolysis. Hemicellulose bonds to cellulose and contributes to the strength of cell walls in biomass.

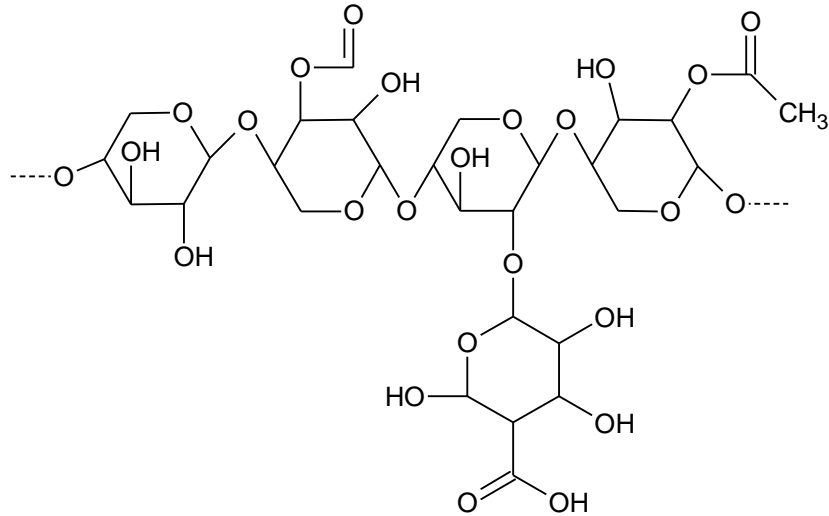


**Figure 4: One Example of a Typical Hemicellulose Structure Adapted from Pandey (Pandey, 1999)**

### 2.3.3 Lignin

Lignin has a more complex structure than hemicellulose and cellulose. It consists of many combinations of aromatic substances that can be ordered randomly as seen in Figure 5. The lignin structural network changes with respect to the feedstock biomass, making it a complex polymer. The carbon content of lignin tends to be greater than 60% and oxygen content is approximately 30% (Zhang, 2010). The difficulty present with lignin is its resistance to being broken down by thermochemical and biological processes. In wood biomasses, lignin surrounds the cellulose and hemicellulose structures leading to increased durability and complications in hydrolysis. Lignin ensures aggressive hydrolysis conditions must be used to isolate glucose molecules.

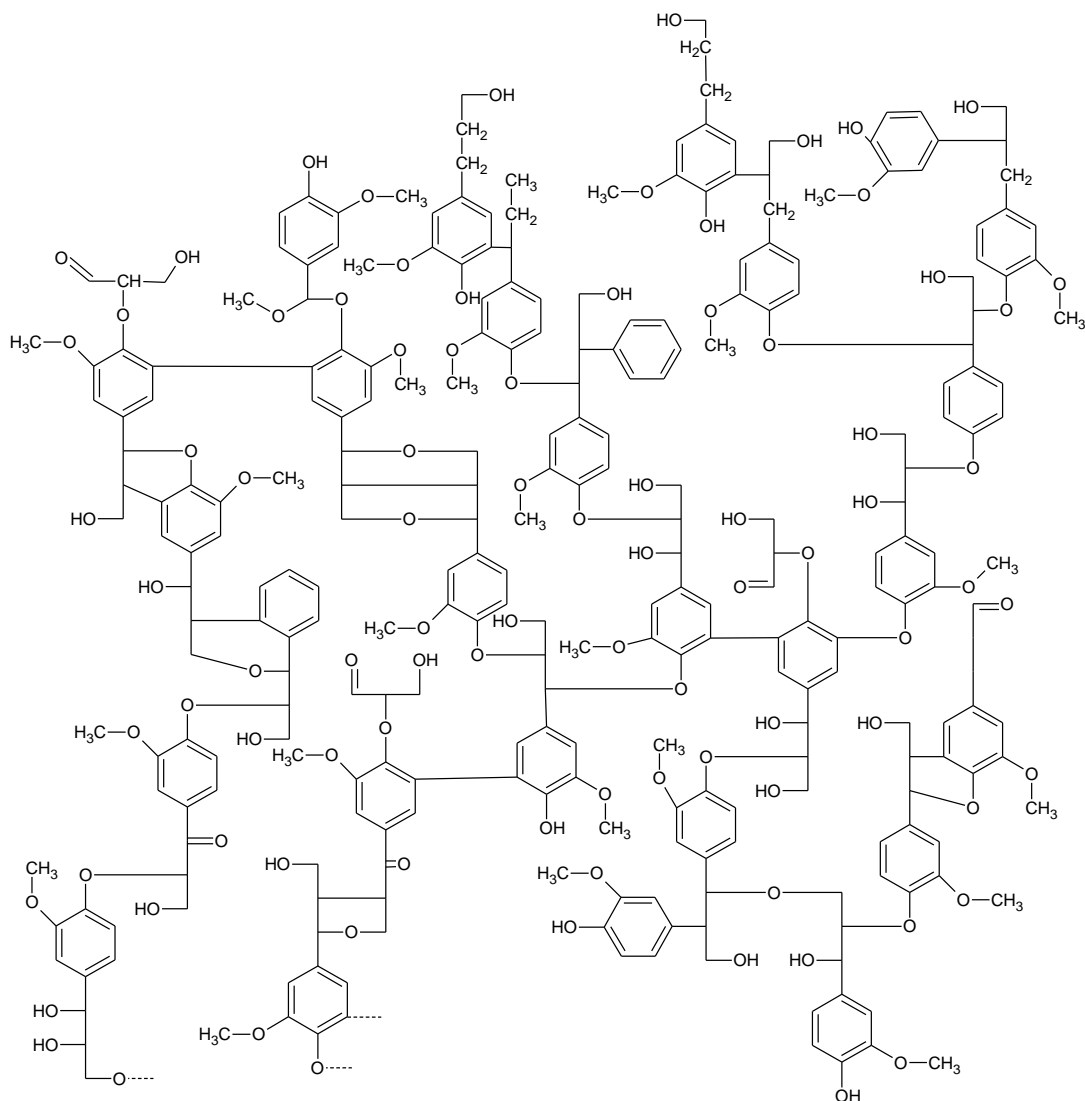


Figure 5: One possibility of lignin content adapted from Glazer (Glazer, 1995)

## 2.4 Key Reaction Pathways

The main biomass materials responsible for breaking down into sugars include cellulose and hemicellulose. On the other hand, lignin can decompose into more complex aromatic compounds under hydrothermal conditions. To model and understand the kinetics of the reactions leading to useful sugars like glucose and fructose, the reaction pathways must be understood.

### 2.4.1 Cellulose Decomposition

Many reaction mechanisms have been proposed for the depolymerization of cellulose into glucose and further breakdown of glucose into numerous molecules under hydrothermal conditions. Reaction mechanisms proposed in literature agree that cellulose will depolymerize into oligomers and then decompose into glucose via a series of hydrolysis reactions. Further decomposition can occur, as represented by the adapted reaction mechanism featured in Figure 6, proposed by Sasaki (Sasaki, 1998). The reaction mechanism shown in Figure 6 was developed

through physical kinetic studies of the degradation of model compounds in sub and supercritical water. These model compounds include cellulose, glucose, dihydroxyacetone, and glyceraldehyde.

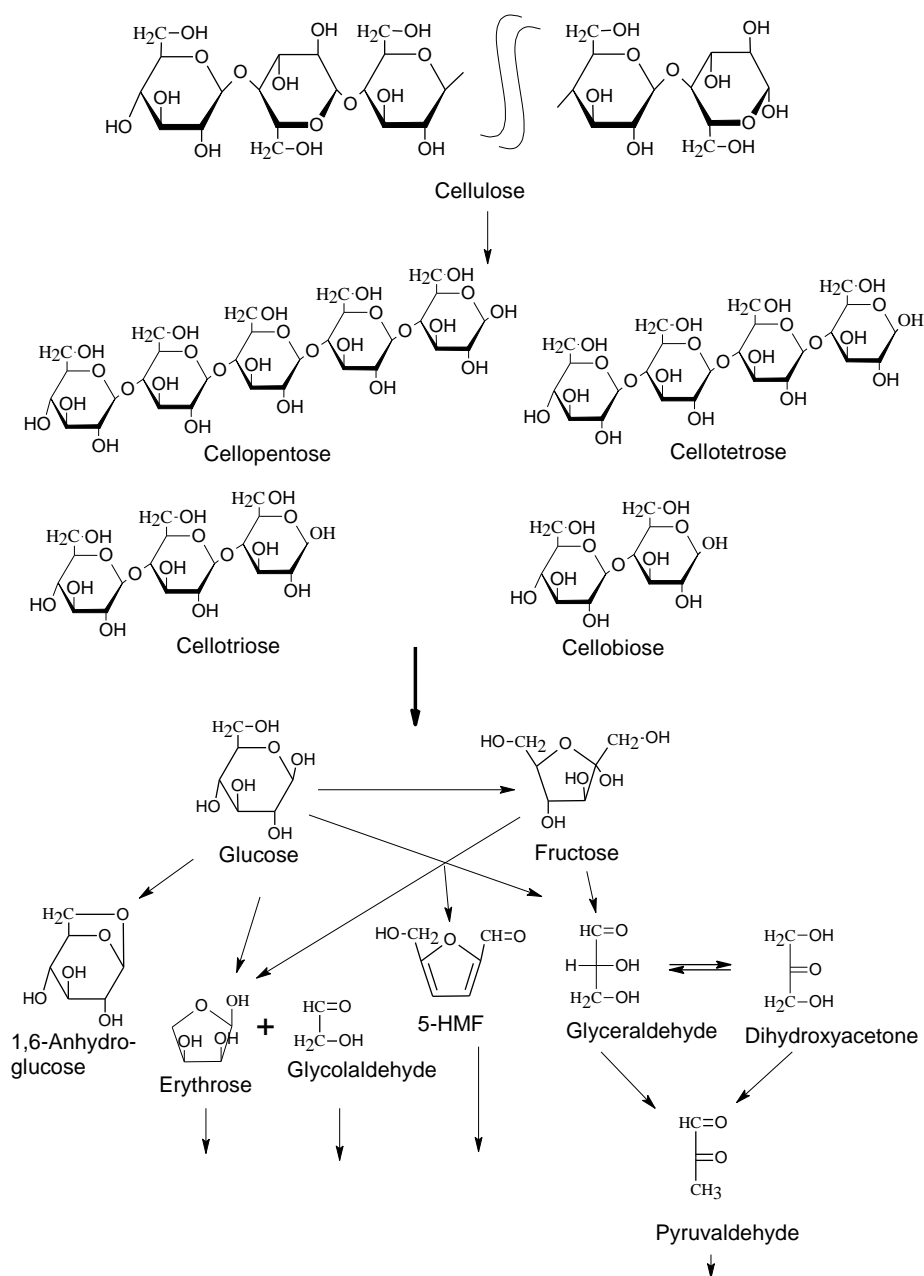


**Figure 6: Reaction Pathway for Cellulose Decomposition Adapted from Sasaki (Sasaki, 1998)**

A mechanism was later proposed by Sasaki and Matsumura which summarized major reaction pathways and the most common intermediates and products of hydrothermal liquefaction in supercritical water. The proposed mechanism organized cellulose breakdown into two major reaction pathways (Figure 7). The first pathway (1) speculated that oligomers (cello-

oligosaccharides) undergo either a hydrolysis reaction or retro-aldol condensation. The resulting products decompose further into glucose and other molecules via hydrolysis, dehydration, and retro-aldol condensation. Glucose is also expected to form fructose via isomerization which would then decompose further. The second reaction pathway (2) identified as thermal cleavage, was observed to occur as temperature increased and pressured decreased (Matsumura, 2006). The reaction pathway developed in Figure 7 was determined through experiments performed on microcrystalline cellulose in supercritical water. The reaction mechanism was estimated based on the analysis of the products formed.



Aida et al. organized literature results of glucose reactions and developed a more detailed reaction mechanism for the isomerization and breakdown of D-glucose and D-fructose as shown in Figure 8 (Aida, 2007). Several reactions can take place involving any of the intermediate isomerization steps to form different by-products. The reaction mechanism shown in Figure 8 was determined through experimental conversion of D-fructose and D-glucose in sub and supercritical water. The reaction mechanism was based on major products produced from the reactions. For this study, Figure 7 and Figure 8 will be used as the basis for the cellulose and glucose decomposition reactions for further study and understanding.

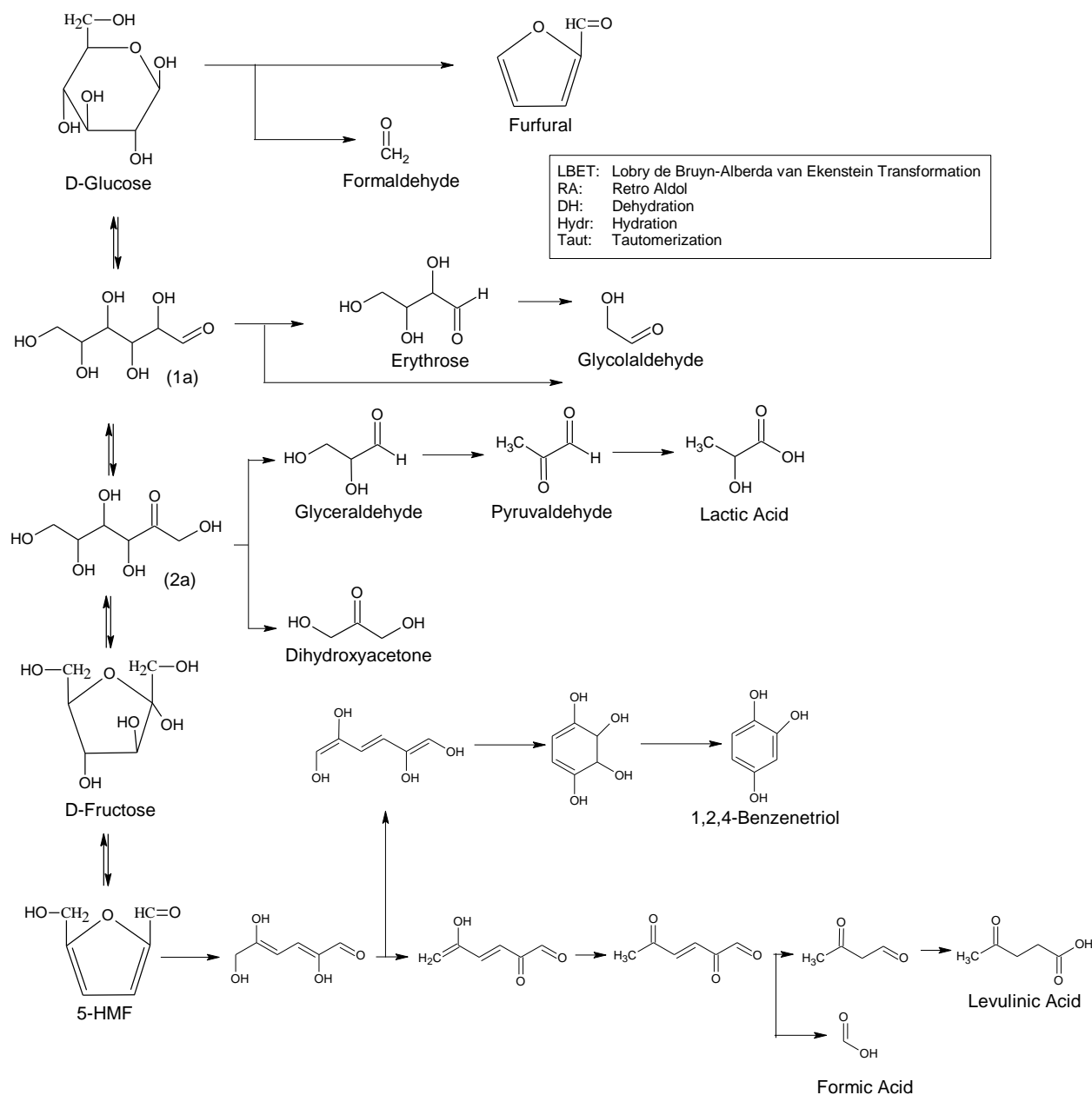


**Figure 8: Detailed Glucose Decomposition Adapted from Aida (Aida, 2007)**

### 2.4.2 Lignin Decomposition

Because of the complex structure of lignin, little is known definitively about the degradation mechanism under HTL conditions. Liu found that the three most likely compounds that were generated from lignin decomposition were compounds very similar to lignin including 2-methoxy-phenol, 3,4-dimethoxy-phenol, and 1,2-benzenediol (Liu, 2006). Based on a model segment of the lignin polymer, Liu was able to propose a simple mechanism for the decomposition of lignin, shown in Figure 9. As reviewed by Toor, many sources indicate that degradation of lignin results in phenols and methoxy phenols (Toor, 2011). These products arise from the hydrolysis of ether bonds in lignin that degrade further by hydrolysis of the methoxy groups (Toor, 2011). Degradation of lignin is catalyzed by alkaline pH hydrolysis reactions.

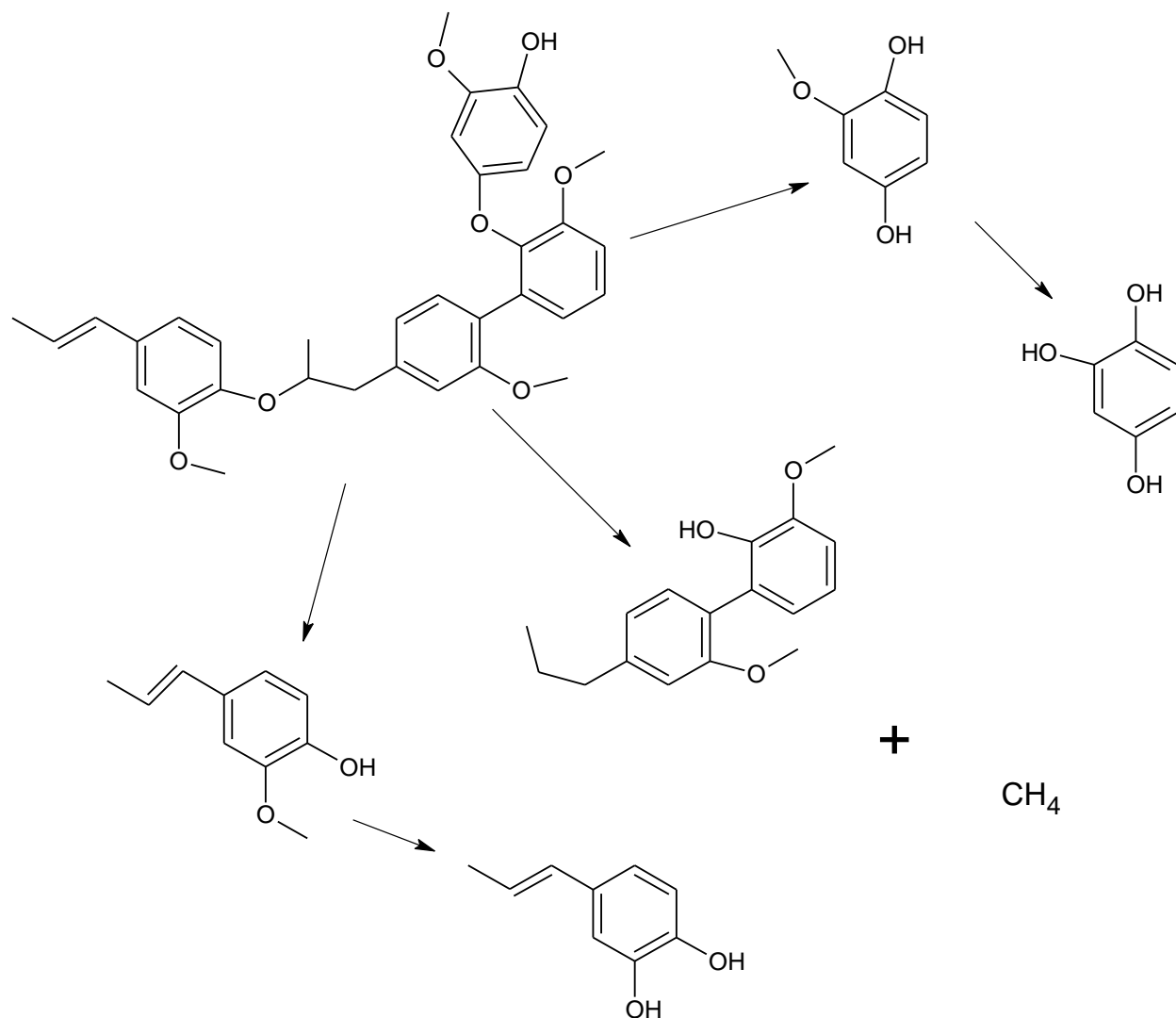


Figure 9: Lignin Decomposition Adapted from Liu (Liu, 2006)

### 2.4.3 Hemicellulose Decomposition

Hemicellulose, like lignin, is difficult to represent in a degradation mechanism because of the various compounds that can exist within the copolymer. The differences in copolymer molecules appear to be dependent on plant types. As reviewed by Toor, hemicellulose is mostly comprised of xylose, mannose, glucose, and galactose (Toor, 2011). Grass hemicellulose tends to be composed of xylan, while wood hemicellulose tends to be richer in mannan, glucan, and galactan. Hemicelluloses are easily hydrolyzed in hydrothermal conditions, giving rise to similar degradation mechanisms as cellulose. Aida proposed that D-xylose can degrade via a retro-aldol reaction, and can isomerize via Lobry de Bruyn-Alberda van Ekenstein transformation based on experimental studies, shown in Figure 10 (Aida, 2010).

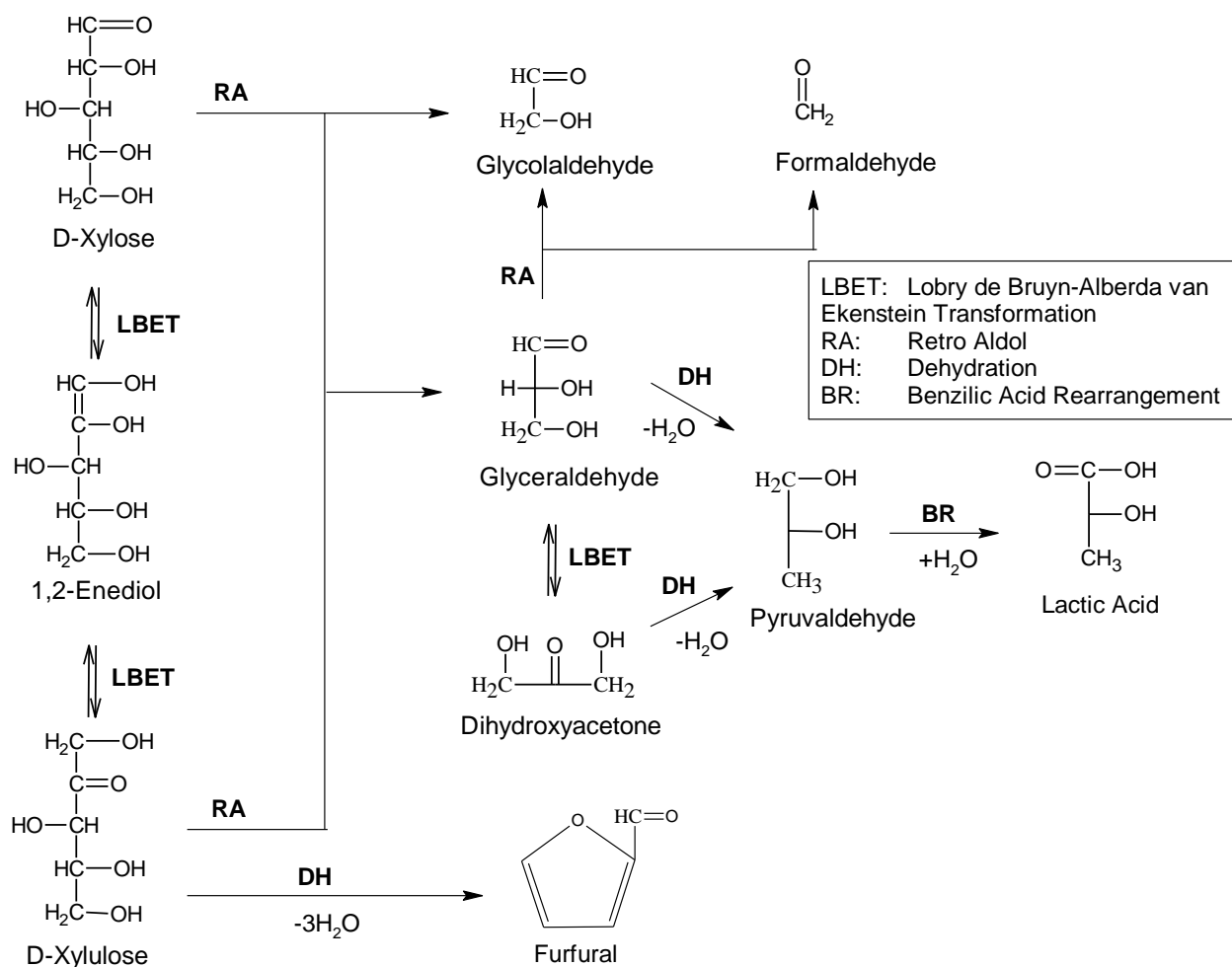


Figure 10: Reaction Mechanism of the Degradation of Xylose Adapted from Aida (Aida, 2010)

### 2.5 Modeling Key Reactions of the HTL Process

Key reactions that take place during the degradation of cellulose and hemicellulose include the isomerization reaction between glucose and fructose, and reactions producing furfural and 5-

HMF. It has been shown that glucose and xylose decomposition can produce furfural, and that fructose can react to form 5-HMF. It was also shown in Figure 8 that glucose or fructose can decompose into a broad range of chemicals. Sugars such as fructose and glucose are important, for instance for their use as fermentation feed. 5-HMF is also useful as it is a precursor to furfural alcohol and furans which can be reacted to form useful solvents.

Assary et al. performed a study on the thermochemistry of the conversion of glucose to levulinic acid (Assary, 2010). This conversion involves the isomerization of glucose to fructose, the conversion of fructose to 5-HMF, and the conversion of 5-HMF to levulinic acid. Assary et al. performed calculations on these reactions at several levels of Gaussian theory, where the Gaussian 4 (G4) method was claimed to be the most accurate of all methods tested. The G4 method was evaluated on 454 experimental energies in the G3/05 test set and showed an absolute deviation of 0.83 kcal/mol from experiments (Curtiss, 2007). The G3/05 test set compares energies generated by computational methods to 454 different experimentally determined energies with uncertainties less than  $\pm 1$  kcal/mol (Curtiss, 2005). The test compares computational values to experimental energetic values found in several sources of literature, many of which are NIST reference documents or NIST JANAF tables. The G3/05 test set is composed of enthalpies of formation, ionization energies, electron affinities, proton affinities, and hydrogen-bond energies. Therefore, the G4 theory is assumed to be accurate and representative of experimental results. Assary et al. also performed computations for several other glucose decomposition reactions (Assary, 2012). Enthalpy and free energy changes of reactions calculated using the G4 method are summarized in Table 1. Reaction 1 refers to glucose to fructose isomerization, reaction 2 refers to fructose to 5-HMF conversion, reaction 3 refers to glucose to glycolaldehyde and erythrose conversion, reaction 4 refers to fructose to dihydroxyacetone and glyceraldehyde conversion, and reaction 5 refers to glyceraldehyde to pyruvaldehyde conversion.

**Table 1: Enthalpies and Free Energies Calculated for Several Reactions Using the G4 method.**

Energy (kcal/mol)	Reaction 1	Reaction 2	Reaction 3	Reaction 4	Reaction 5
$\Delta H^0$	2.1	12.4	34.3	26.9	-6.9
$\Delta G^0$	1.9	-22.9	18.1	10.3	-18.7

Nimlos et al. performed computational calculations on the energetics of the closed ring D-xylose decompositions using Gaussian 3 CBS-QB3. A change in energy of 16.5 kcal/mol was determined from a protonated molecule of xylose to a protonated molecule of furfural including the dissociation of water clusters formed from dehydration reactions (Nimlos, 2006). Excluding the dissociation of water clusters because of being in an aqueous solution, the energy change was found to be -13.2 kcal/mol. Data from Nimlos et al. provides a means of determining method accuracy by comparing energies between this study and the study by Nimlos et al.

## 2.6 Optimum Conditions for Bio-oil Yield

The products formed from performing HTL can result in a wide range of compounds and reactant conversions depending on many factors throughout the process. Factors proven to be most critical include biomass type, reaction conditions, heating rate, and residence time (Akhtar, 2011). Other factors that have shown to affect product composition and conversion include particle size, and the inclusion of foreign chemicals such as solvents or catalysts. The main products of HTL include bio-crude oil, char, gas, and other water soluble substances (Sun, 2011). In a study by Karagöz, at least 25 compounds were detected in bio-crude oil derived from a rice husk substrate, at least 15 compounds were detected in bio-crude oil derived from a sawdust substrate, and at least 18 compounds were detected in bio-crude oil derived from cellulose and lignin (Karagöz, 2005). Seven different gaseous compounds were also detected, but the majority consisted of carbon dioxide for all runs. The study by Karagöz emphasizes the wide range of products that can be formed from biomass substrates such as cellulose and lignin. Generally, HTL results in an aqueous carbohydrate solution which can be converted into other fuels if desired such as alkanes or hydrogen (Kumar, 2009). The solutions produced consist almost entirely of a combination of sugars (glucose, fructose etc.), aldehydes, ketones, and oligomers (Akhtar, 2011). Because of the relevance to this study, the effect of residence time, reaction conditions, heating rate, and particle size will be summarized based on a review performed by Akhtar of previously completed studies (Akhtar, 2011).

### 2.6.1 Residence Time

Residence time of biomass materials under HTL conditions affects the composition of substances in the final mixture. Kumar et al found that when biomass underwent HTL from temperatures of 235-260 °C from 0-60 minutes, there was an optimum residence time of approximately 10 minutes which increased the total organic carbon (TOC) in the aqueous phase. As residence time increased past that optimum point, the total organic carbon concentration in the aqueous phase began to decrease (Kumar, 2009). A similar phenomenon was observed by Qu, in which *Cunninghamia lanceolata* underwent HTL from 10-30 minutes at temperatures ranging from 280-360<sup>0</sup>C (Qu, 2003). Qu did not observe an optimum, but observed a decrease in yield of bio-crude as time continued for all reaction temperatures. It may be that an optimum in bio-oil yield had existed, but the optimum occurred in the reaction before the products were removed and analyzed. Another study by Karagöz focused on the effects that temperature and residence time have on total yields from sawdust biomass (Karagöz, 2004). They found that at lower temperatures (180<sup>0</sup>C), increased reaction times resulted in greater yields, but at higher temperatures (250<sup>0</sup>C), longer residence times resulted in lower yields. This phenomenon was attributed to increased production of gaseous products at higher temperatures and longer residence times. An optimum residence time appears to exist but varies based on the target temperature of the experiment. In general, optimum residence time increases with decreasing target temperature.

### 2.6.2 Temperature and Pressure

Higher temperatures have been shown to cause biomass depolymerization. As temperature increases towards the critical temperature of water, gas formation becomes dominant. Certain temperatures exist that result in a maximum bio-oil recovery from initial biomass feed. Sugano performed hydrothermal liquefaction on eucalyptus with paper regeneration wastewater as a solvent and found that there was an optimum temperature for creating bio-oil (Sugano, 2007). Oil yields were low at temperatures below 250°C, but increased as temperatures rose to 300°C and began to decline again around 350°C. This phenomenon was observed in many studies and is summarized by Akhtar. It is energetically unfavorable for biomass degradation to occur at low temperatures. At higher temperatures, gas formation reactions begin and decomposition of products continues. Reactions driven by free radicals also cause recombination and the formation of char at high temperatures (Akhtar, 2011). Decomposition is speculated to produce the most liquid bio-oil at temperatures from 300-350°C. Pressure is thought to play a few very important roles. Sufficient pressure allows the medium to remain in one phase, eliminating the need to provide additional enthalpy for vaporization. Liquid solvent phase would allow reaction sites to be more attainable for the catalytic solvent. If the pressure is maintained above the critical pressure, the temperature can be varied in order to control reaction rates and bio-oil conversion without phase changes. Controlling temperature and pressure allows the user to be more selective with respect to liquid or gaseous products.

### 2.6.3 Heating Rate

Heating rates have shown to increase liquid oil yields in HTL as the heating rate increases. It may also assist in inhibiting char formation but may not be crucial because hot compressed water tends to stabilize intermediate species. Zhang found that increasing heating rates from 5-140 °C/min increased liquid oil yields from 63% to 76% by weight (Zhang, 2009). Char formation may increase with decreased heating rate because of the subsequent increase in residence time and therefore more opportunity for recombination of solids.

### 2.6.4 Particle Size

Particle size reduction of biomass materials under hydrothermal conditions has been observed to provide little benefit to bio-oil yield. Zhang found that there was no increase in bio-oil yield when particle size was reduced from one inch to half a millimeter at 350 °C (Zhang, 2009). Akhtar proposed that the degree of hydrolysis and fragmentation of biomass is more heavily related to heat transfer limitations rather than availability limitations related to particle size. Given subcritical water can help overcome the heat transfer limitations because of its role as both a “heat transfer medium and an extractant” (Akhtar, 2011), particle size then becomes an ancillary parameter. Bio-oil yield is speculated to be unaffected by varying particle sizes. However, less discussion exists regarding whether changes in particle size affect the chemical distribution within liquid and solid phases.

## 2.7 Previous Methods, Biomasses, and Analysis Techniques

Many relevant studies in which raw biomass materials are converted to bio-oil and solid residue are summarized in the table below. Table 2 summarizes the conditions and biomass feed used for the conversion process. The resulting weight percentage of solid products and liquid products are listed. Understanding these conditions and subsequent product distribution quickly allows for method verification and to quickly understand how differences in methodology may affect results. Post processing methods of samples are also listed on the summary table along the tools for analysis of those samples. Sample preparation and analysis illustrate any restrictions that may have been put on component identification given some analysis techniques can only detect certain compounds.

**Table 2: Literature Summary of HTL Processes**

<b>Reference</b>	<b>Biomass Material and solvent</b>	<b>Particle Size (microns)</b>	<b>Biomass Feed to Solvent Ratio</b>	<b>Temp (°C)/heat rate (°C/min)</b>	<b>% Solid Product by Mass</b>	<b>% Liquid Product by Mass</b>	<b>Separations Performed on Product Samples</b>	<b>Analysis Tool</b>
Karagöz (2005)	Sawdust, rice husk, lignin, cellulose. Performed in water	N/A	1:6	280/3	41.7	58.3	Products acidified, diethyl ether and ethyl acetate extraction. Evaporation	Oils: GCMS
Xu and Lad (2008)	Jack pine in water	800	1:10	300-380/ N/A	21-40	28-57	Filtration, reduced pressure evaporation at several temperatures	Oils: GCMS
Qu (2003)	Cunninghamia in water	70	1:10	280-300	19-37	20-52	Acetone wash, reduced pressure evaporation	Analyzed C, N, and O composition with EA analyzer
Zhang (2010)	Paper/pulp in water	N/A	1:10	400-450/10	25-30	25-33	Ethyl acetate extraction, reduced pressure evaporation	GCMS
Sun (2011)	Paulownia in water with catalyst	200	1:6	280-360/5	20-25	30-45	Filtration, acetone wash, reduced pressure evaporation	Shimadzu FTIR and GCMS
Mostiero-Romero (2014)	Spruce wood in water	400-800	1:10	250-350/25-30	23-57	29-68	Water wash, hexane wash and extraction, filtration	Liquid: GCMS Solid: PSA & SEM
Cheng (2010)	White pine in water	800	1:10	300/10	30	64	Acetone wash, filtration, reduced pressure evaporation	Shimadzu GC-MS

## 3. Experimental

### 3.1 Equipment

#### 3.1.1 Reactor

The liquefaction of the wood biomass occurred in a 500 mL stainless steel Parr reactor rated at 2000 psi and 350 °C. The reactor was fitted with a magnetic motor and was sealed with a Teflon O-ring rated at 350 °C to ensure a proper seal. The temperature and stirring motor were controlled by a Watlow temperature controller. To ensure the metal stirrer did not overheat and seize a VVO Scientific Products Water Circulator directed cold water from a bath through an inlet and outlet nozzle at the base of the stirrer. A Swagelok sampling valve with an extended metal hose was attached to the cap of the reactor if sampling was needed during experiments. A Swagelok safety release valve was attached in case of over pressurizing to prevent the reactor from catastrophically failing. The entire set up is shown in Figure 11.

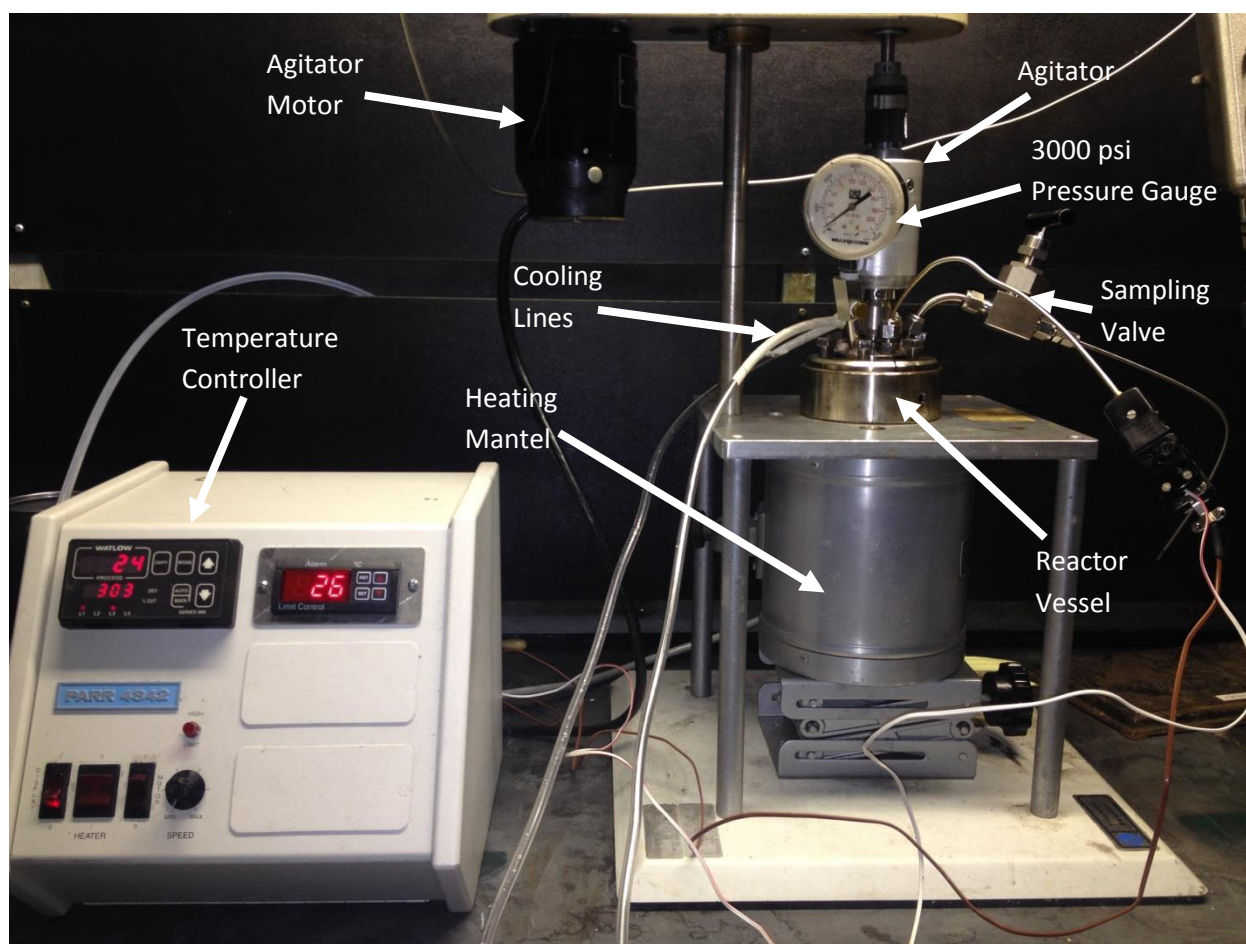


Figure 11: Reactor Set Up

### **3.1.2 HPLC**

The HPLC is a Shimadzu Liquid Chromatograph Model LC-10AD comprised of many machines connected to a computer interface. Two devices existed in the HPLC that detected the compounds in samples, a Shimadzu UV-VIS spectrometer Model SPD-10A and a Sedere LT-ELSD Sedex 90. The sample runs through these detectors in the order listed. The sample is separated into its components through a Phenomenex 00H-0138-K0 column heated by a Shimadzu Column Oven Model CTO-10A. The second sensory equipment, Sedere LT-ELSD Sedex 90, has its own heating apparatus for evaporating purposes for the samples and was controlled separately.

### **3.1.3 Rotary Evaporator**

To concentrate the biomass samples for analysis, excess water is evaporated off with a Buchi Rotavap. A separate hot bath was used to heat the sample to 60<sup>0</sup>C and the system was vacuumed to 8 cmHg to more readily facilitate the evaporation of the water. The system was left running for 20-30 minutes for each separation.

### 3.2. Procedure and Analytical Technique

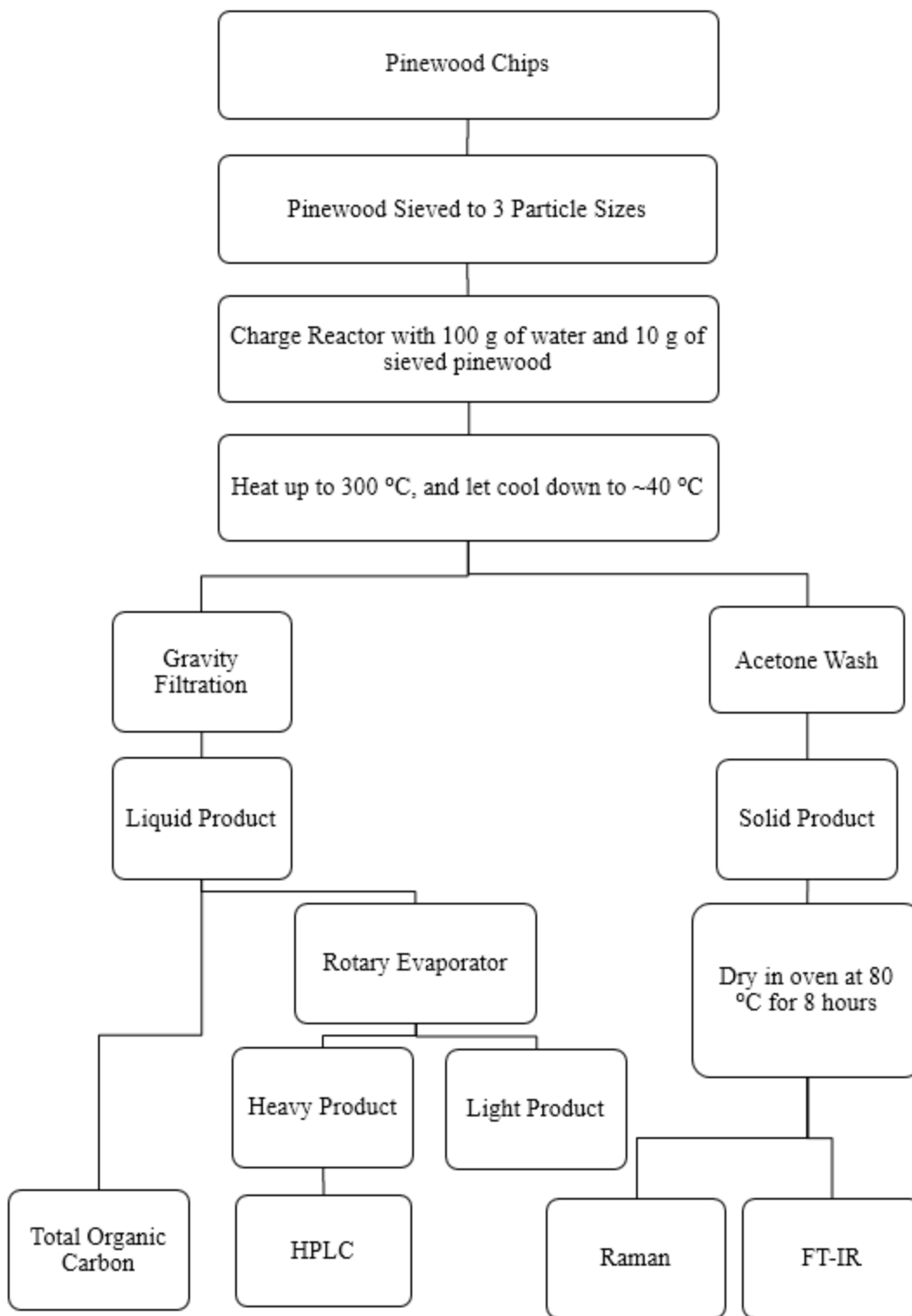


Figure 12: Experimental and Analytical Procedure

### 3.2.1 Feed Stock Preparation

Testing was performed on the pine wood under hydrothermal conditions. Pine wood was ground in a coffee grinder from 10 seconds to 1 minute depending on the size of particles desired. The resulting mixture was separated based on particle size by utilizing sieve trays of specific sizes including 106-150, 212-300, and 1680-2000 microns. Different biomass particle sizes used for experimentation are shown below in Figure 13.



Figure 13: Feed Stock Particle Size

As the particle size decreases, the overall surface area increases, and limitations from mass transfer would decrease, which is the focus of this study. All other conditions remained constant when different particle sizes were used in order to identify significant changes in the products. Experiments were performed using pure water as the solvent.

### 3.2.2 Converting Biomass

The liquefaction was performed using a mixture of water and biomass which was charged to the 500 mL Parr reactor at a ratio of 1:10 biomass to water by weight at atmospheric conditions. The reactor was sealed, cooling water was initiated to the stirrer, and heat was applied. Using a thermocouple, the final temperature of the slurry was set to 300 °C which was identified as being in the range of temperature necessary to convert biomass. Table 3 outlines the conditions used for each experiment. Each particle size had two experimental procedures performed under the same conditions, in order to study reproducibility.

Table 3: Hydrothermal Liquefaction Reaction Parameters

Parameter	Experiment #1	Experiment #2	Experiment #3
Temperature (°C)	300	300	300
Pressure (psig)	1300	1300	1300
Heat Up Rate (°C/min)	4	4	4
Residence Time Upon Target Temperature (seconds)	0	0	0
Particle Size (μm)	106-150	212-300	1680-2000

### 3.2.3 Sample Retrieval and Analyzing Product

Samples were removed when the reactor cooled to 40 °C after reaching the set point of 300 °C. The reactor was opened and contents were filtered by gravity through Macherey-Nagel MN 640 W No. 40 filter paper. Liquid product collected under filter was considered “recoverable product” or product that is recoverable by simple means. The recoverable product and wet solids in filter paper were massed. The wet solids were massed again after drying in order to understand how much liquid product was contained by the solids. Residual solid products in the reactor were washed with a known amount of acetone. The acetone slurry was massed in order to discover the total mass of wet residual solid particles from the reactor. The acetone slurry was left to dry in a fume hood and was dried completely in an oven at 80°C for at least 8 hours. The mass of dry solids were taken to identify the mass of liquid product present in the solid residue. The difference between the total mass charged to the reactor and the liquid and solid products obtained was assumed to be a combination of gas products and products lost when transferring material. Gas products are known to be produced in very small yields, around 6 wt % of initial biomass, which was assumed in our study, as found in the literature (Cheng, 2010). Considering small amounts solid product was lost, all lost product was considered to be liquid product except for 0.6 grams contributed by gas products. The filtered liquid products were evaporated in a rotary evaporator at a pressure of 8 cmHg and a temperature of 60°C for 20-30 minutes. The heavy product recovered from evaporation was expected to contain most desired products such as sugars, oligomers, 5-HMF, furfural, and acetic acid. The heavy product was analyzed using the HPLC. Component peaks were identified by comparing elution time to standard solutions run under the same conditions. HPLC chromatograms were compared across different experiments to understand the effect of particle size distribution on compound distribution.

### 3.2.4 HPLC Methodology

Initially, standards of expected products were analyzed using the HPLC in order to produce peaks that could later be compared to the bio-oil produced. All standards and liquid product HPLC runs were performed at same conditions save for injection volume and concentration of solutions. The HPLC column oven was operated at 30°C, the UV detector was set at a wavelength of 254 nm, and the flow rate of fluid through the column was set to 1.000 mL/min. The ELSD temperature, pressure, and gain were set to 60°C, 44-46 psi, and 4, respectively. The mobile phase consisted of a 0.002M aqueous solution of sulfuric acid. Liquid samples were injected with a volume of 90 µL and standards were injected with a volume of 30 µL to avoid reaching the maximum limits of the detectors. Chemicals that were used in standard solution development and their weight percentages are outlined in Table 4.

**Table 4: Chemicals and Weight Percentages in Water Used for Standard Solution Development. All standards were injected using an injection volume of 30  $\mu$ L**

Chemical	Weight %					
D-Glucose	1.098	0.77	0.60	0.40	0.20	0.05
D-Fructose	1.0	0.80	0.60	0.40	0.20	0.05
D-Xylose	1.0	0.78	0.55	0.40	0.20	0.05
Cellobiose	1.0	0.80	0.60	0.40	0.20	0.05
5-HMF	1.0	0.80	0.60	0.40	0.20	0.05
2-Furaldehyde	1.0	0.80	0.60	0.40	0.20	0.05

Raw filtered liquid from the experiment and concentrated bio-oil were analyzed using the HPLC. The resulting peaks were analyzed against the standards in order to determine what components were produced by the hydrothermal liquefaction of pine wood. The chromatograms produced for each particle size was also compared to note any significant changes in compound distribution when utilizing different particle sizes.

### 3.2.5 FT-IR Methodology

Infrared spectra ( $500\text{-}4500\text{ cm}^{-1}$ ) were recorded by a Nicolet IR100 FT-IR (Fourier Transform InfRared) spectrometer equipped with a silicon beam splitter with a  $1\text{ cm}^{-1}$  resolution. Using this, IR radiation was passed through bio-char produced from each experiment to understand the absorbance. Consequently, this created a spectrum which represents the absorption at different wavenumbers for each of the samples. The samples were prepared by drawing a small sample from the bio-char and gently placing it on the beam path.

### 3.2.6 Raman Methodology

After the bio-char was thoroughly dried in an oven at  $80\text{ }^{\circ}\text{C}$  overnight the samples were prepared for the Horiba XploRA Raman Microscope by taking a small sample of bio-char and creating a smooth layer over a microscope slide. The laser was set to observe in the range of  $532\text{ nm}$ . The microscope was set to take readings over the Raman shift range of  $500\text{-}2100\text{ cm}^{-1}$  where the presence of the D and G peaks occur. An acquisition time of 5 seconds, an accumulation of 30, and a 10% filter were inputted for the acquisition parameters of the Raman microscope. The resulting Raman spectra was exported and interpreted using the MagicPlot software.

### 3.2.7 Total Organic Carbon Analysis Methodology

Raw liquid products from each sample were analyzed in a Shimadzu TOC 5000A for total carbon content using the SM 5310B High Temperature Combustion Method as cited in Standard Methods for the Examination of Waters and Wastewaters (APHA, 1998). The samples analyzed were composed of raw liquid product diluted with water by a factor of approximately 300 which was expected to result in a solution with a carbon concentration below  $100\text{mg/L}$  solution. This dilution rate was crucial in order to remain in the range of the calibration curve used to determine total carbon concentration.

### 3.2.8 Modeling Thermochemistry

The thermochemistry of key reactions within the hydrothermal liquefaction process was also predicted using the analytical chemistry interface WebMO. Several calculation theories were used in order to find the most effective theory for quickly approximating the thermochemistry of key reactions in the HTL process. Ideally, predicted energies would be verified by comparing values to experimentally determined energies for the expected reaction. In the absence of energies determined experimentally, predicted energies were compared to energies of the same reactions calculated at very high levels of theory in the literature. The most effective modeling method was identified based accuracy of energies calculated and qualitative trends (if energy changes were positive or negative). The geometry of species was either created manually or imported from PDB or MOL files. The chemical structure would first be optimized using the PM3 method followed by geometry optimization using the B3LYP 6-31G\* or Hartree-Fock 6-31G\* method. Once the geometry was optimized, the structures vibrational frequencies were calculated at different levels of theory and compared to literature values.

## 5. Results and Discussion

### 5.1 Physical Observations and Mass Balance

The products formed from the reactions included gas, solid, and liquid products. When the reactor was opened, gas product quickly released from the vessel producing a hissing noise. Gas products were not collected but were assumed to account for 0.6 g of final products which was the quantity of gas formed in a study by Cheng performed under similar conditions. Cheng also loaded 100 g of water and 10 g of pine wood feedstock into a stirred batch reactor, though the heat up rate used was 10 °C/min rather than 4 °C/min performed in this study (Cheng, 2010). The actual mass of gas product produced could not be inferred from a mass balance because a significant mass of liquid product had to be inferred from the mass balance. Liquid product could not be measured fully because of liquid phase that was lost or unaccounted for during transfer and washing steps. The pressure gauge used to monitor pressure within the reactor measured up to 3000 psig and had poor resolution close to atmospheric pressure. Due to this, only pressures greater than or equal to 50 psig could be detected within the reactor. The reactor was assumed to be perfectly sealed during operation, and initially sealed at atmospheric pressure. Given carbon dioxide is the primary gas expected to be produced, 2.3 g of carbon dioxide would need to be produced to result in a pressure of 50 psig, as determined from the ideal gas law. Due to the uncertainty, 0.6 g of gas produced will be assumed with a possible error of +1.7 g. The final mass balance therefore will attribute 0.6 g of missing mass to gas with an error of +1.7 g.

Solid and liquid products formed slurry at the bottom of the reaction vessel. Transferring solids inherently produced experimental error from uncollected residue lodged in crevices of the reactor. Because of this, total masses of solids are assumed to have an error of +0.2 g. Solid product or bio-char, tended to stick to the reaction vessel and agitator, with more char adhering to the agitator when smaller particle sizes were used for feed. The bio-char was a dark brown color and varied in particle size depending on the particle size of initial feed. Visual inspection indicated that smaller feed particles resulted in smaller char particles and more adherences to internal components. Using smaller particles then has the disadvantage of more adherence to internal components due to smaller char particles having more surface area and less mass per particle, allowing sticking more easily. Internal components needed to be cleaned for small scale experiments in order to ensure future mass balances and products were unpolluted by old experiments. This sticking may also prove cumbersome in large scale batch processes as the material adhering to components is expected to be lignin which may remain and accumulate over several runs due to its resistance to react. The resulting particles of each particle size experiment can be seen in Figure 14.



**Figure 14: Bio-char from Three Different Particle Sizes; Top Left 106-150  $\mu\text{m}$ ; Top Right 212-300  $\mu\text{m}$ ; Bottom 1680-2000  $\mu\text{m}$**

More liquid product was observed to be collected from simple gravity filtration when larger particle sizes were used. This is because larger particle sizes have larger spaces between individual particles, requiring more energy to keep liquid suspended in the wet char. Liquid product after filtration accounted for the majority of mass in the reactor given much of the liquid product consisted of water. All liquid products appeared to be water soluble, and no liquid phase separation was observed in the liquid product. Because liquid product produced was calculated by the difference between total initial mass and the sum of solid and gas products, the error associated with the total mass of liquid products is -1.9 g. -1.9 g is the opposite sum of error of solid and gas products. Recovering more liquid from reaction products is beneficial assuming the quality and quantity of bio-oil produced from raw biomass remains the same. Therefore, larger particle sizes have the advantage of collecting more liquid product through simple methods like gravity filtration. Below, Figure 15 displays the types of liquid product recovered as well as products from the rotary evaporator. The light yellow liquid on the left was raw liquid recovered from gravity filtration of raw products removed from the reactor. The dark colored liquid in the center was heavy key recovered from the rotary evaporation of the raw liquid product on the left. The clear liquid on the right is the light key recovered from the rotary evaporation of the raw liquid product on the left.



**Figure 15: Liquid Products; Left Raw Liquid Product; Middle Concentrated Liquid from Rotary Evaporator; Left Evaporated Liquid from Rotary Evaporator**

With every experiment, a certain mass of material was lost or could not be accounted for in the final mass balance. These losses and materials that were unaccounted for were likely due to evaporation of product and acetone during the acetone rinse. When collecting product, 55.4 g of acetone was used to rinse wet char from the inside of the reactor while the reactor vessel temperature varied from 30-40 °C. During the process, a significant portion of the acetone could have evaporated which would appear as lost product in the final mass balance. Because all solids were dried and accounted for, the lost products were identified as liquid products except for the 0.6 g of gas assumed to be formed. Figure 16 shows the mass balance for each run performed on the different pine particle sizes. Liquid product reported is a combination of gravity filtered liquid and liquid suspended in solid particles. The first run performed using 106-150  $\mu\text{m}$  particles shows significantly more lost product and gas than the other experiments. This discrepancy is attributed to experimental error and is not reflected as a consequence of using that particular particle size. Figure 16 shows that no significant trend appears to exist between particle size and the amount of liquid product or solid product formed. If there were significant mass transfer limitations present under these conditions, it may be expected that less liquid product would be formed for larger particle sizes; however, this does not seem to be the case.

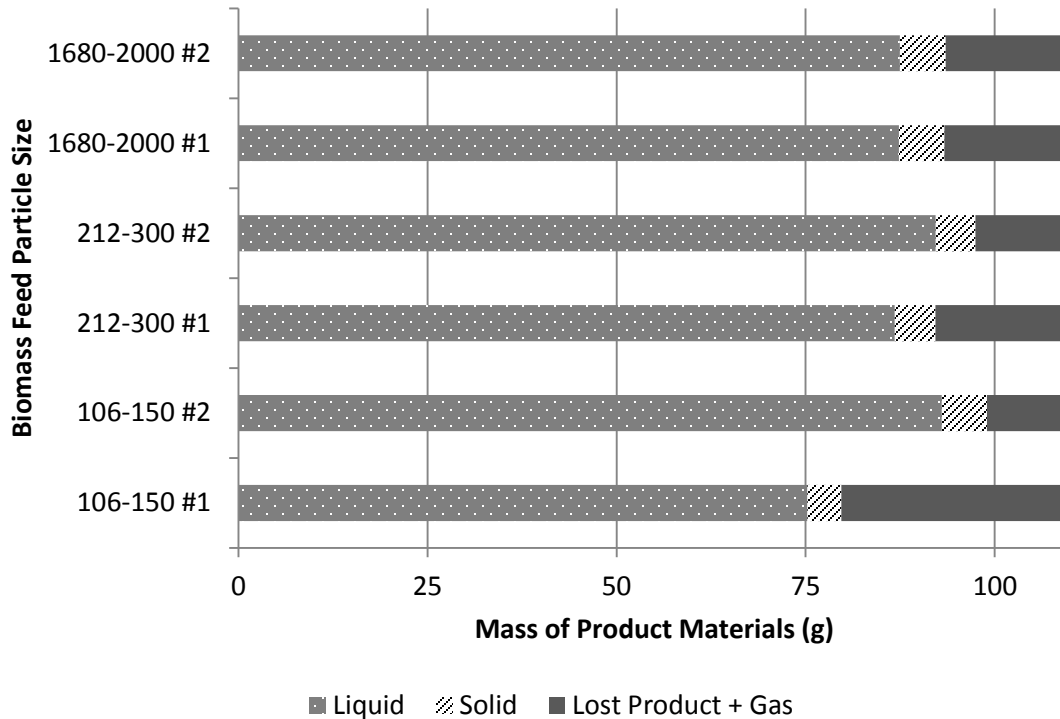


**Figure 16: Mass of Liquids and Solids Directly Measured. Mass of Material Lost, Unaccounted for, or Produced as Gas. Reactor was Initially Filled with 100g of Water and 10g of Biomass.**

Below, Figure 17 shows the mass distribution of product phases produced from the initial biomass feed, excluding the 100 g of water initially added as solvent. The plot appears to indicate a trend showing an increase in liquid product with a decrease in particle size. This conclusion may not be valid, however, when error bars are introduced to the plot. Because liquid product produced from biomass was determined by the difference between initial feed and the sum of solid and gaseous products, the total liquid present holds an uncertainty equal to the sum of the uncertainties of the solid and gaseous product. The error associated with each phase is represented with error bars, with the liquid phase experiencing a possible error of -1.9 g, the solid phase experiencing a possible error of +0.2 g, and the gas phase experiencing a possible error of +1.7 g. Regardless of error, it is clear that solid products are responsible for a majority of the mass produced from pine biomass, around 4-7 g with uncertainty included. It has been shown from a mass balance perspective that no significant trend exists between particle size and quantity of specific phases. It would be more advantageous to utilize larger particle sizes from a liquid yield perspective as yield remains the same and cost required to mill particles is reduced. It is possible that slight increases in liquid products occur with decreasing particle size but more studies with more experiments would have to be performed to verify this.

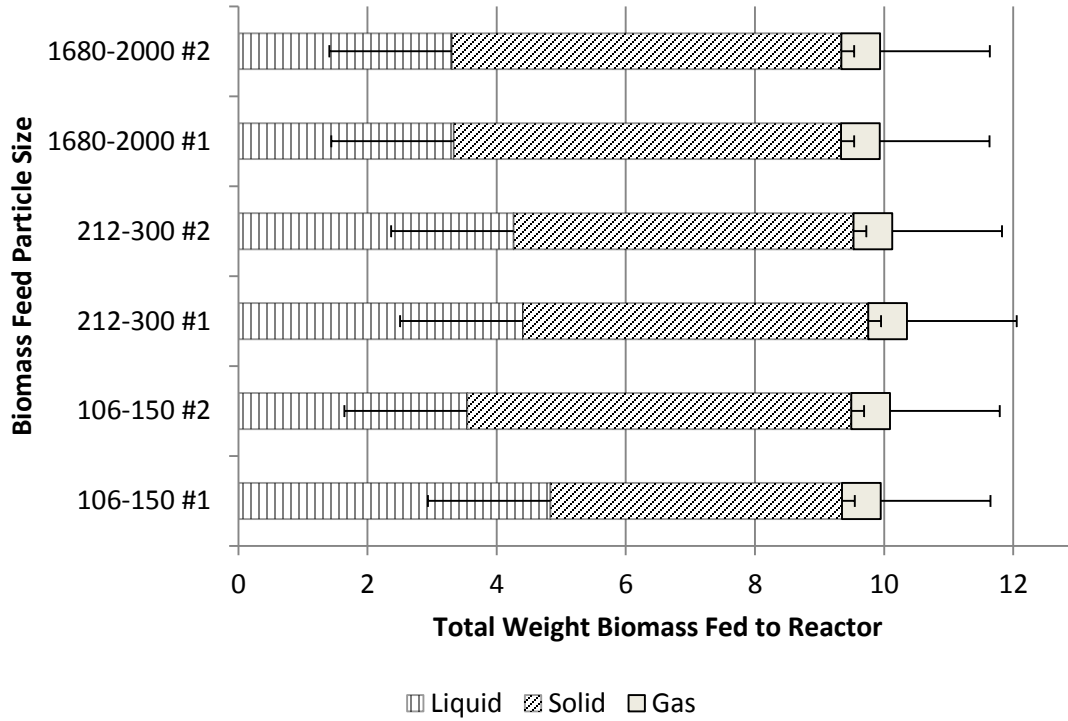


**Figure 17: Percentage Weight of Initial Biomass Feed Converted into Different Phases of Product with Error Bars**

Figure 18 shows how temperature within the reactor varied across time for each run, excluding the first experiment involving 106-150  $\mu\text{m}$  particles. Variation exists among time taken to heat the reactor to target temperature across experiments. These variations lead to differences in heating rates, cooling rates, and residence times which can be seen in Table 5.

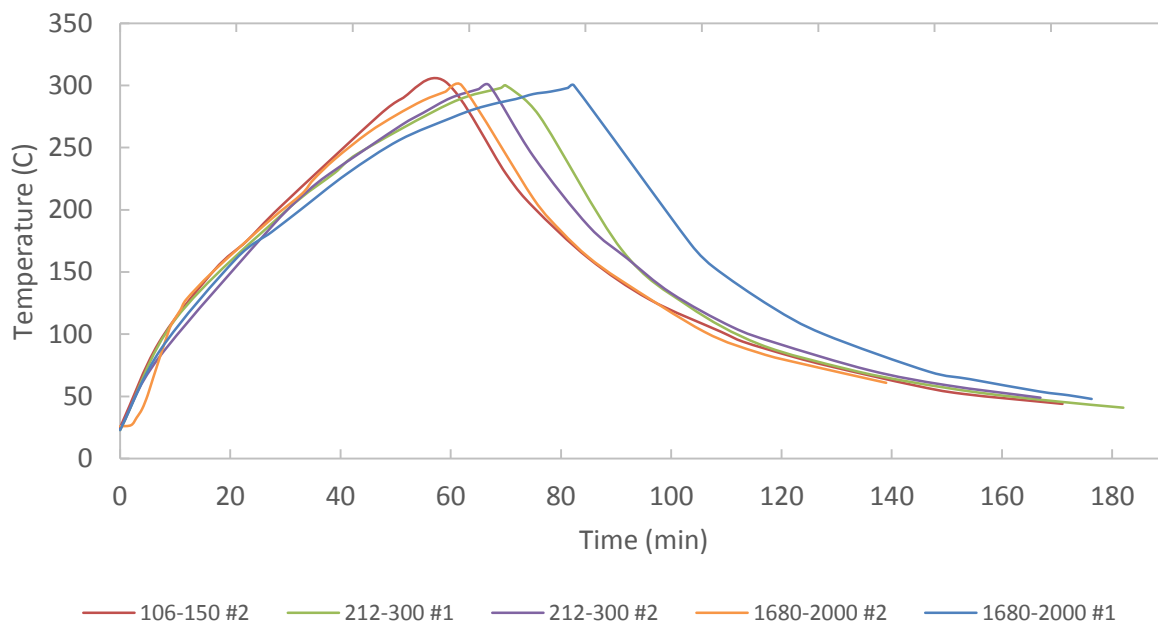


**Figure 18: Plot Showing Temperature of Reactor over Time**

The table below shows overall heating rates across the entire experiment and heating rates when the reactor temperature was rising above 200 °C as that is the point where reaction are expected to begin. Therefore 200-300 °C is an important temperature range to study for analysis purposes.

**Table 5: Outline of Overall Average Heating Rate (HR Overall), Average Heating Rate While the Reactor Temperature was Increasing Above 200 °C (HR Above 200 °C), and Residence Time While the Reactor was Above 200 °C (RT Above 200 °C) for each Experiment**

<b>Experiment</b>	<b>HR Overall (°C/min)</b>	<b>HR Above 200 °C (°C/min)</b>	<b>RT Above 200 °C (min)</b>
106-150 #2	4.17	3.366	44
212-300 #1	3.96	2.53	52
212-300 #2	4.12	3.16	48
1680-2000 #1	3.55	2.13	60
1680-2000 #2	4.42	3.11	44

The variations in heating rate vary slightly from run to run, even though test procedures remained the same concerning the temperature controller, set temperature (300 °C), and room temperature (~23 °C). Therefore, it is concluded that the heating rate differences can be largely attributed to the varying air flow rate through the hood which the experiments took place in. Depending on the position of the window on the hood and the reactor position within the hood, convective cooling could have reduced the heating rate. In order to minimize the effects of this, future experiments should utilize an insulating jacket around the heating mantel.

## 5.2 HPLC, UV/Vis, and ELSD Analysis

Standard solutions were prepared to develop calibration curves comparing weight percentage in solution to total area of associated peaks. These standards were also useful for identifying elution time for each compound. Standard curves for sugars cellobiose, glucose, xylose, and fructose are included in Figure 19. The standard curves indicate the elution times for each chemical and indicate that glucose, xylose, and fructose elute very closely, therefore causing overlap between chromatograms. This behavior would lead to a chromatogram with multiple connected peaks of increasing intensity. Standard curves for 5-HMF and furfural are included in Figure 20. Because of the column design, larger sugar molecules are expected to elute faster than small sugars, which contain less carbon. Acetic acid and formic acid standards were developed and were detected by the UV/Vis detector. However, the peaks were insignificant in size. For example, a standard sample containing 20 wt % of acetic acid in water resulted in a peak with an intensity of 20 mV. Since the concentrated bio-oil samples caused spikes in the UV/Vis detector of a magnitude of 2000 mV, it would not be beneficial to compare the standard peaks of acetic acid and formic acid to the UV/Vis chromatograms. It is likely that the column, which is an acid column, is being protonated with the formic acid and acetic acid solutions. The protonation would result in the acids getting stuck in the column. This is likely attributed to the concentration of the acidic mobile phase which was decreased from the recommended concentration in order to prevent excessive noise on the ELSD.

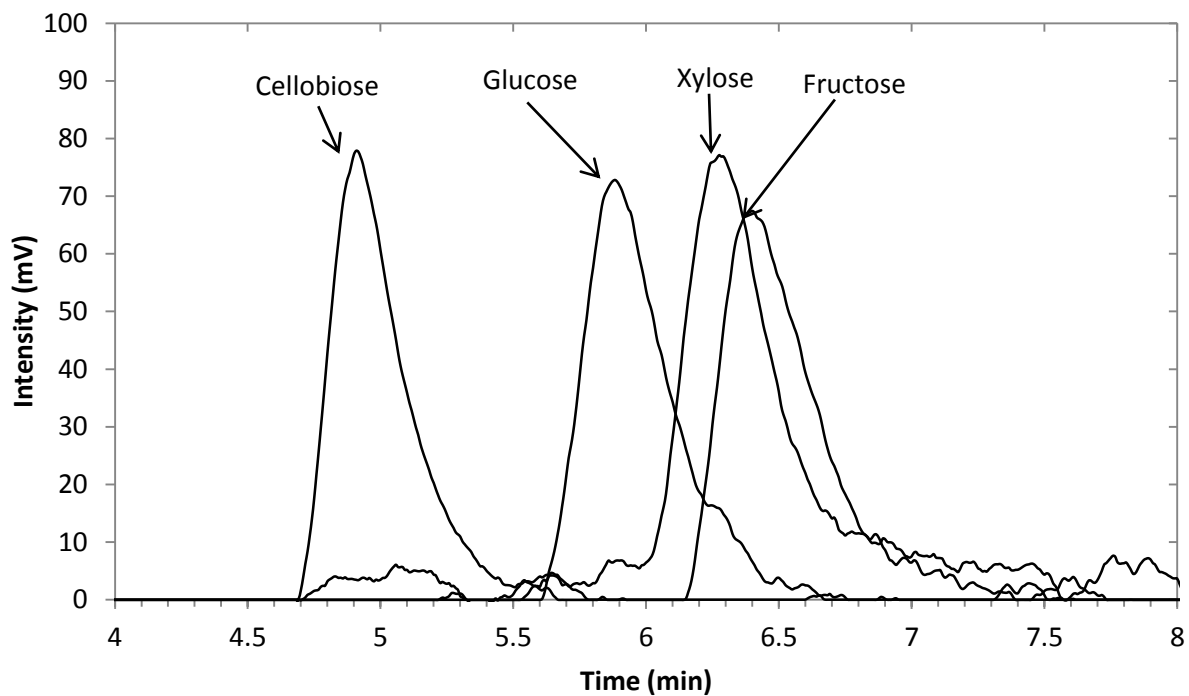


Figure 19: ELSD Chromatograms of Sugars: Cellobiose, Glucose, Xylose, and Fructose each of 0.05 Wt % in Water.

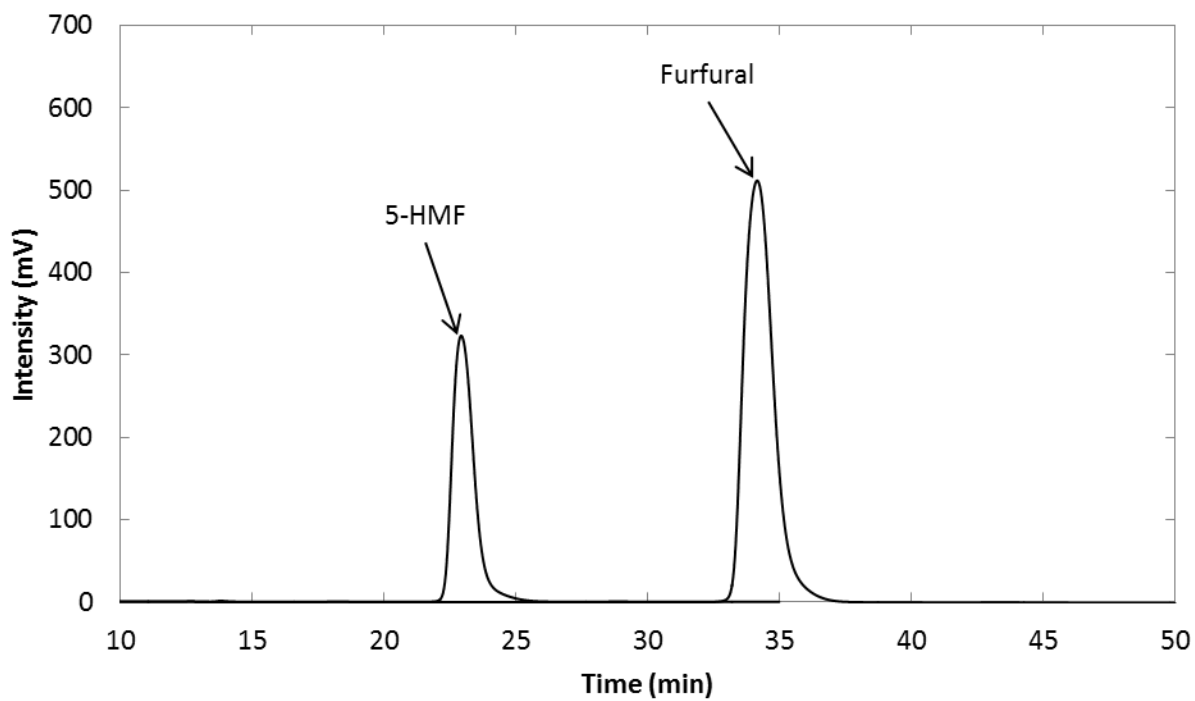
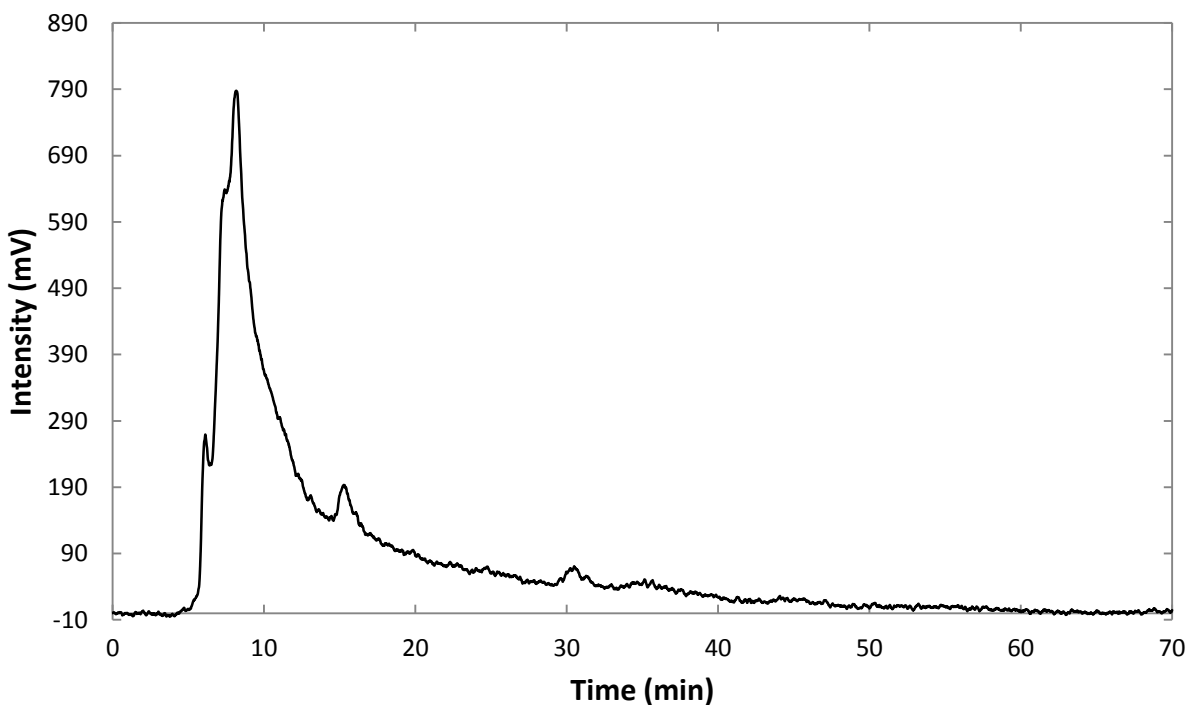
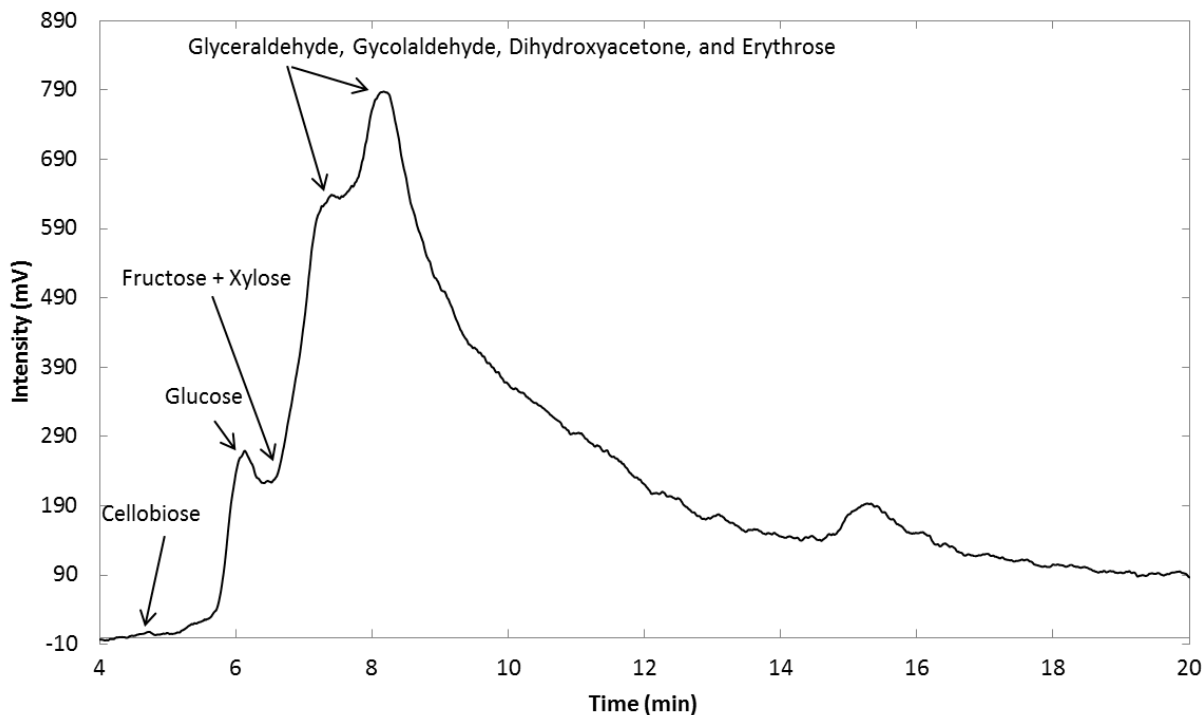


Figure 20: UV/Vis Chromatograms of 0.05 Wt % 5-HMF and Furfural in Water.

Figure 21 shows the chromatogram generated from the ELSD which demonstrates typical behavior of concentrated bio-oil samples. Figure 22 shows the first twenty minutes of the plot shown in Figure 21. These chromatograms were produced from a biomass particle size varying between 1680-2000  $\mu\text{m}$ . Four defined peaks can be identified at times near 6, 7, 8, and 15 minutes. The peak eluting at 6 minutes is generated from glucose, and the valley as well as the quick increase in the chromatogram directly after is caused by a combination of fructose, xylose, and other pentoses. This crowded behavior near glucose was expected since glucose, fructose, and xylose had overlapping elution times. The presence of individual chemicals between 6 and 7 minutes is difficult to identify due to the lack of distinct peaks, though the literature indicates that fructose and xylose should be present as products. A small peak also exists around 5 minutes which is the result of cellobiose. As demonstrated by the standards, larger sugars like cellobiose elute before smaller sugars like glucose. Based on the chromatogram, larger chained sugars have decomposed entirely into smaller molecules as almost no activity was detected before and near cellobiose. This is a strong indication that reactions are continuing towards completion during the time of the reaction since larger molecules that comprise the original structure have degraded. The peaks at 7 and 8 minutes are expected to be tetrose and triose sugars such as erythrose, glycolaldehyde, glyceraldehyde, and dihydroxyacetone. These plots indicate that the product solutions are rich in sugars of varying carbon amounts.

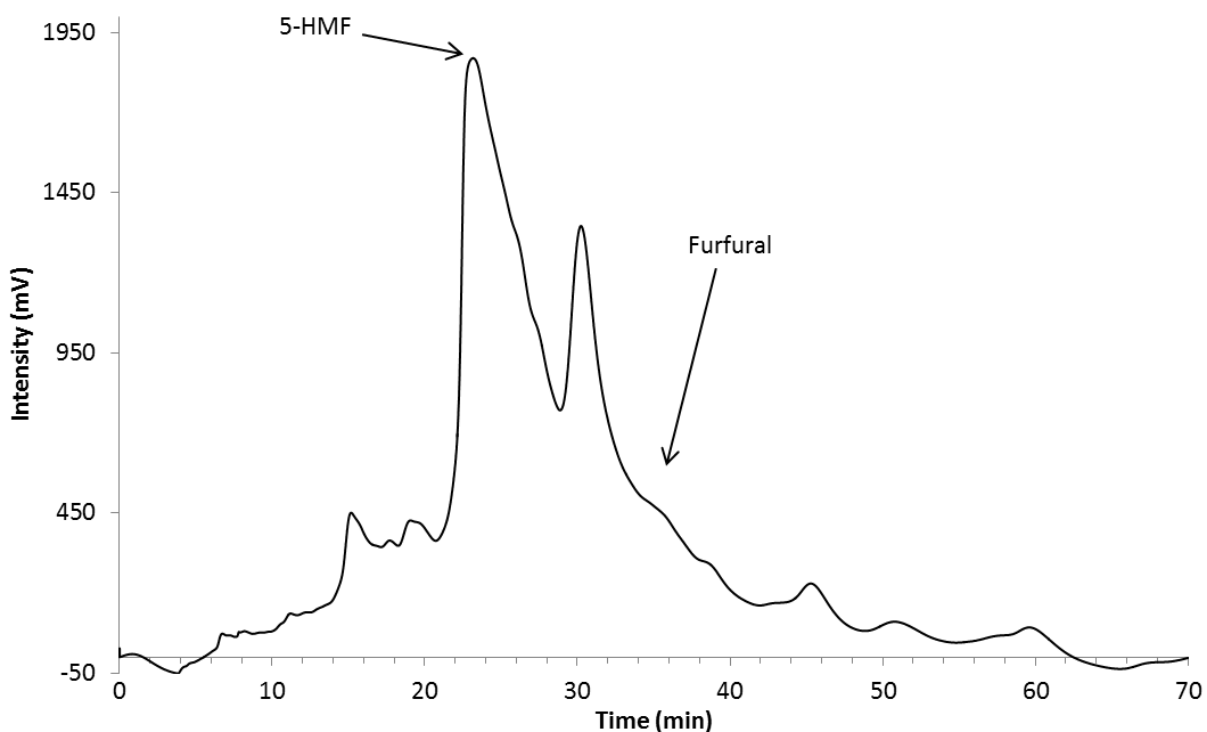


**Figure 21: ELSD Chromatogram for the Bio-oil Produced by 1680-2000  $\mu\text{m}$  #1 Pine Particles**



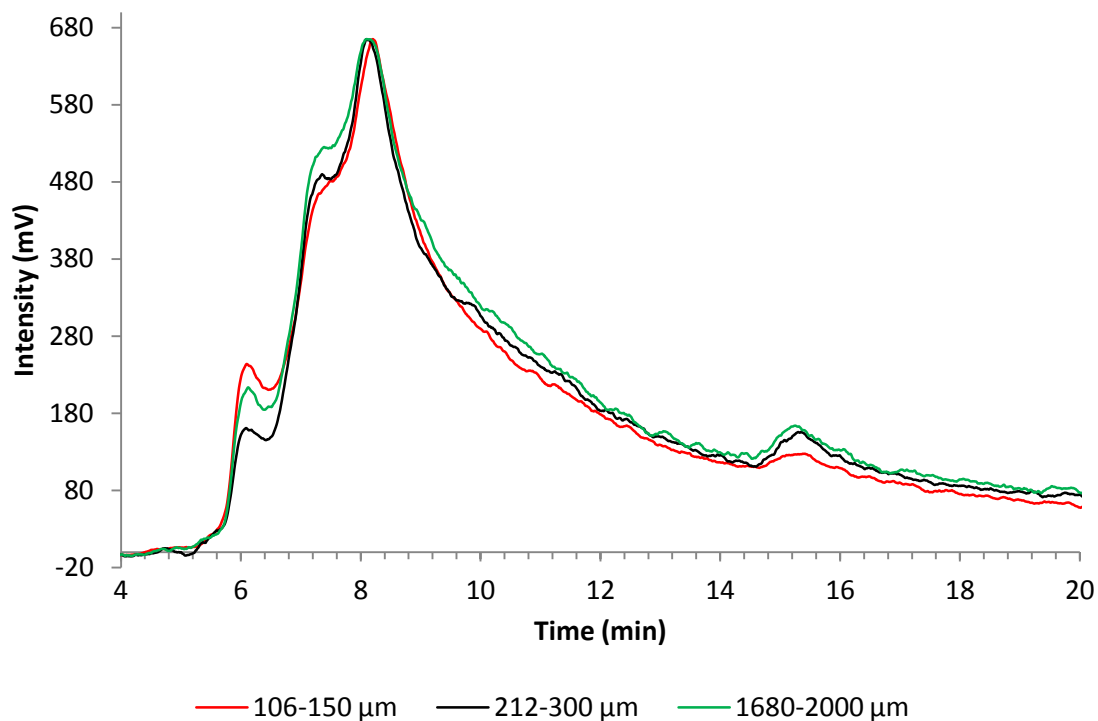
**Figure 22: ELSD Chromatogram for the Bio-oil Produced by 1680-2000  $\mu\text{m}$  #1 Pine Particles Zoomed**

Figure 23 shows the chromatogram generated from the UV/Vis detector of the same experiment using 1680-2000  $\mu\text{m}$  particles. A few major peaks exist including those at 15, 24, 30, and 45 minutes. Though there are a few major peaks, the chromatogram is dominated by a peak at 24 minutes generated by 5-HMF. This implies that 5-HMF is a major product of hydrothermal liquefaction as was expected. Furfural was also produced and can be seen as a small bump around 35 minutes but is distorted by the tail of the peak that exists around 30 minutes. Because the standard curve of furfural produced a peak with an intensity of 500 mV at a concentration of 0.05 wt %, the concentration of furfural in total sample is considered low. Intensities of peaks generated by separate molecules can vary widely; therefore little can be determined of the relative concentrations of compounds by peaks not corresponding to a particular standard. For instance, a 20 wt % acetic acid in water solution produced a peak that was 20 mV as compared to a 0.05 wt % solution of 5-HMF in water which produced a peak that was 300 mV.



**Figure 23: UV/Vis Chromatogram of Concentrated Bio-oil Produced from 1680-2000  $\mu\text{m}$  #1 Pine Particles**

Figure 24 displays averaged chromatograms for the bio-oils produced from each particle size overlapped and scaled to the highest peak. The behavior of the chromatogram for each particle size is very similar. These overlapped plots indicate that the same chemicals are produced from each particle size under the current conditions. However, slight differences in relative product concentrations can be seen between different particle sizes. For instance, the glucose peak at 6 minutes appears in greater concentration for the particle sizes of 106-150  $\mu\text{m}$  and 1680-2000  $\mu\text{m}$ . This is not likely due to particle size variation as there is no trend relating increasing particle size with more glucose. The slight difference in relative intensities is likely due to a combination of factors. First, there is natural variation (noise) in the chromatogram likely caused by fluctuations in flow rate through the detectors. Second, some products were subject to degradation through storage over several days. Solid degradation products were visually noticed within samples after being refrigerated for extended periods. Third, the pressure, temperature, and duration that samples were evaporated for varied slightly, which could lead to degradation or fluctuation in the amount of compounds removed from the heavy phase. Overall this information implies that particle size has little to no effect on compound distribution in the heavy oil under the current experimental conditions.



**Figure 24: Plot of Overlapped ELSD Chromatograms Produced for each Particle Size**

Upon examination of UV/Vis chromatograms produced from the liquid products of each particle size, it was clear that they also had very similar trends. This indicates that the same chemicals are likely formed when hydrothermal liquefaction is performed on each particle size of pine under the current experimental conditions. However, significant variations in peak shape were noted in runs of the same particle size. Specifically, the 5-HMF peak varied between experiments. To some lesser extent, the small peak produced by furfural also had a variable shape. The differences in the 5-HMF peak were noted for experiments where the samples were analyzed in the HPLC at different time intervals after being initially formed.

For samples analyzed several days after being produced, the 5-HMF peak appears to broaden, as shown below in Figure 25. This was observed for particle size experiments 212-300  $\mu\text{m}$  and 1680-2000  $\mu\text{m}$ . The samples physically showed darkened color and solid particles which formed after being stored for several days. 5-HMF has been shown to form in sugar solutions and contribute a dark color to the solution. It is then inferred that the samples degrade over time and create additional 5-HMF which contributes to darker color in solution. The same trend was investigated for ELSD plots of identical particle size runs but no trend was identified. This implies that either degradation occurs between products detected by the UV/Vis or there is insufficient resolution in the ELSD to see the minute changes caused by degradation.

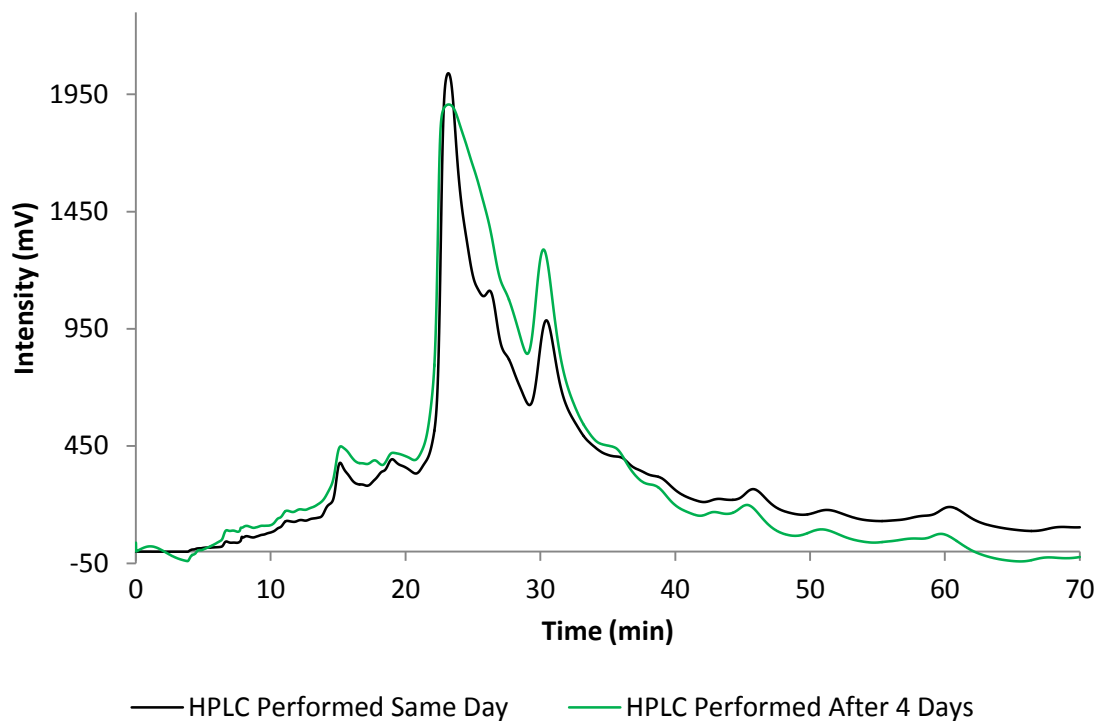


**Figure 25: HPLC Chromatogram Comparing Degradation of Samples**

### 5.3 FT-IR Analysis

In studying the role that particle size played on the products, one solid sample from each experimental run (total of 6) as well as raw pine wood were studied using the FT-IR. Evaluating the spectrum gives useful information such as identification of the type of bonds present in the sample based on where the peak lies versus the wavelength, and the relative amount of the components present based on the size of the absorption peaks (Byrd, 1998). Additionally, based off of literature, the absorption peaks were able to be identified as to whether they were contributed from lignin, cellulose, or hemicellulose.

Before each sample was placed on the beam path in the machine, a background spectrum was measured for the purpose of creating a baseline where the sample can be compared to. With our samples, it was found that even with the background spectrum eliminated, the high sensitivity of the FT-IR resulted in different baselines, as shown in Appendix A: FT-IR Spectrums. The baselines are supposed to be equivalent, therefore it was necessary to adjust the spectrums so that absorption peak height could be accurately determined and compared from one sample to another. Below, in Figure 26, the same two samples are brought to an equivalent arbitrary absorption rate base of  $0.01$  at  $4500\text{ cm}^{-1}$  and an average of the two spectrums is included.

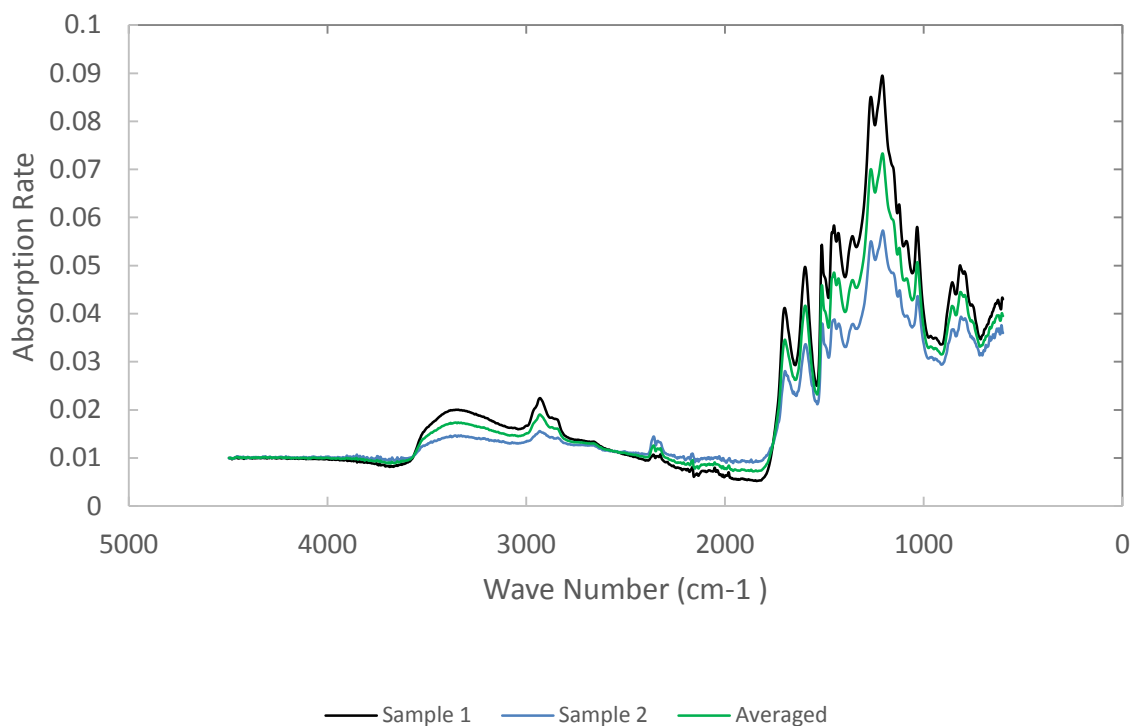


**Figure 26: FT-IR Spectrum of Two Separate 212-300  $\mu\text{m}$  Experiments with Normalized Baseline**

As shown above, with both of the experiments having a normalized baseline, the absorption peak heights can be compared. This method is used throughout the rest of the experimental FT-IR analysis. From Figure 26 it is noticeable that the absorption peak heights are varied throughout the 500-1700  $\text{cm}^{-1}$  wave numbers. This is the general absorption rate gap that was also present in the other two particle sizes studied, 212-300  $\mu\text{m}$  and 1680-2000  $\mu\text{m}$ . But, the average of the two spectrums will be used to represent each particle size bio-char, as it is most important in determining the bond type present, and the amount of components present will therefore have associated error.

All of the bio-char particle sizes were compared against one another, along with a sample of the raw pine wood. It is important to notice the substantial difference in peak heights as well as their respective wave numbers. This can be seen in Figure 27 below.

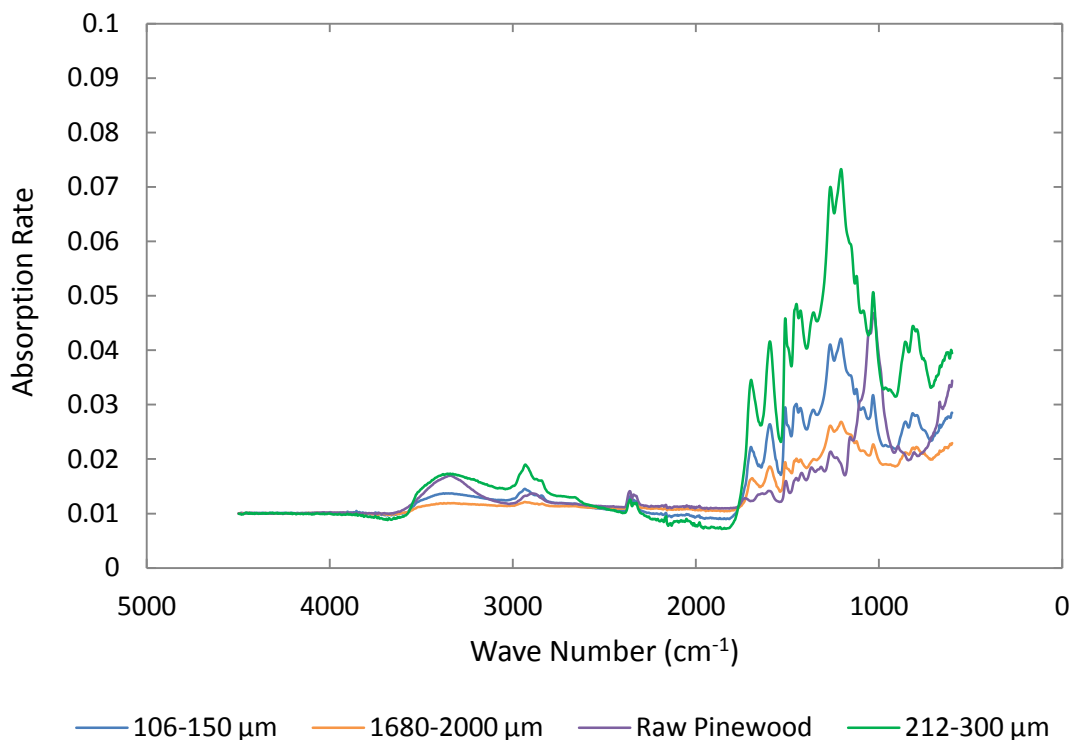


**Figure 27: FT-IR Spectrum Overlapped for Each Particle Size and Raw Pine wood**

From Figure 27, the first spectrum analyzed was the raw pine wood since each of the bio-char samples were compared to this to understand how the solids have changed from reacting. The raw pine wood exhibits a similar overall shape compared to the bio-char with differences in relative intensities. To analyze the bond types and compound types, the wave number where the experimental absorption rate peaks appear were compared with literature values (Byrd, 2014). It is important to note that functional groups fell into certain band ranges. Within these ranges, peak wave numbers were identified as the wave number corresponding to the top of each peak. Therefore, the literature and experimental peak values are not exactly the same, but are comparable. Below, Table 6 shows the functional groups that appear from the IR spectrum of all tested samples and their associated band range and peak wave numbers.

**Table 6: FT-IR spectra of bio-char (Byrd, 2014)**

Position of the Bands and Peaks (cm <sup>-1</sup> )			Functional Group
Literature Band Range	Literature Peak Value	Experimental Value	
675-1000	820	820	C=H Alkenes
675-1000	850	860	C=H Alkenes
1000-1280	1050	1030	C-O Esters
1050-1280	1240	1210	C-O Esters
1050-1280	1280	1270	C-O Esters
1350-1470	1470	1455	C-H Alkanes
1500-1600	1500	1515	C=C Aromatic Rings
1500-1500	1600	1600	C=C Aromatic Rings
1670-1760	1700	1700	C=O Aldehydes
2930-2960	2940	2934	C-H Alkanes
3080-3500	3390	3380	C=H Alkenes

As shown above, the wave numbers found in the literature correlate very well with the experimental values, and provide bond types that were expected. Analyzing the raw pine wood, one prominent absorption peak was at 1030 cm<sup>-1</sup>, indicating that C-O bonds were present in the form of esters, which represents cellulose (Byrd, 1998). Thus, it is important to note that the bio-char at this same wavelength had much less of that type of C-O ester present, indicating that the cellulose was decomposed into the bio-oil (Kumar, 2010).

Absorption that occurred in the bio-char but not in the raw pine wood appeared within 1210-1700 cm<sup>-1</sup>. In this range, C-O esters, C=C aromatic rings, and C=O aldehydes were present. This demonstrates that as the reactions took place, aromatic rings started to recombine at higher temperatures. Most importantly, these aromatic rings can be largely attributed to the lignin and cellulose decomposition, since hemicellulose reacts readily. This is supported by previous studies which showed only about 40% conversion of lignin, and therefore the rest is decomposed cellulose (Karagöz, 2005). The C-O esters and C=O aldehydes present in the spectrums also exist in the depolymerization of cellulose and hemicellulose, as shown previously by Sasaki and Aida (Sasaki, 1998), (Matsumura, 2006), (Aida, 2006), (Aida, 2007). Yet, with the hemicellulose reacting readily, these functional groups represent decomposed cellulose. Therefore, the large intensity of the C-O esters, C=C aromatic rings, and C=O aldehydes present in the bio-char versus the raw pine wood can be attributed to lignin (aromatic rings) but also the cellulose breaking down and remaining in solid form (esters, aromatic rings, and aldehydes). (Kumar, 2010).

But, the effect of particle size on the bond types in bio-char is inconclusive. The bio-char represented the same bonds, but at different intensities without any particular order. This is true with the exception of the 1680-2000 µm particle size at 2934 cm<sup>-1</sup> and at 3380 cm<sup>-1</sup>. At these

wavelengths every sample, including the raw pine wood, had absorption rates indicating that C-H alkanes and C=C alkenes were present (Byrd, 1998). Interestingly, this was not due to the method of averaging the 1680-2000  $\mu\text{m}$  spectrums, and instead was consistent between them, as seen in the Appendix.

Since every spectrum is an average of only two samples for each particle size, it would not be an accurate representation to calculate the amount of each type of bond present. Likewise, a sample size of two for each particle size makes it difficult to conclude that there are consistent trends. Instead, further analysis would need to be performed with more samples from each particle size.

#### 5.4 Raman Analysis

A Raman microscope was used in order to attain a further understanding of the bio-char produced from the hydrolysis of the different particle sizes of pine wood feedstock. Raman spectroscopy is a powerful method for the analysis of graphitic materials. Even though the bio-char produced is relatively amorphous, it does have similar properties to graphite especially with its  $\text{sp}^2$  bonds. By comparing the intensity ratios of the disordered peaks (D peak) and the graphitic peaks (G peak) the size and how ordered the  $\text{sp}^2$  carbon bonds of the bio-char are can be characterized. The existence of a D peak ( $1000\text{-}1500\text{ cm}^{-1}$ ) in the sample describes highly ordered benzene ring structures in the material. The G peak ( $1510\text{-}1700\text{ cm}^{-1}$ ) of the sample characterizes  $\text{sp}^2$  stretch vibrations of olefinic compounds and related chains (Schwan, 1996). The relative shape and distribution of the D and G peaks describe the overall order and structure of the carbon material as either amorphous or graphitic (Ferrari, 2000). The intensity ratio of the D peak to the G peak (ID/IG) describes the size and number of  $\text{sp}^2$  clusters in the material (Petrova, 2011).

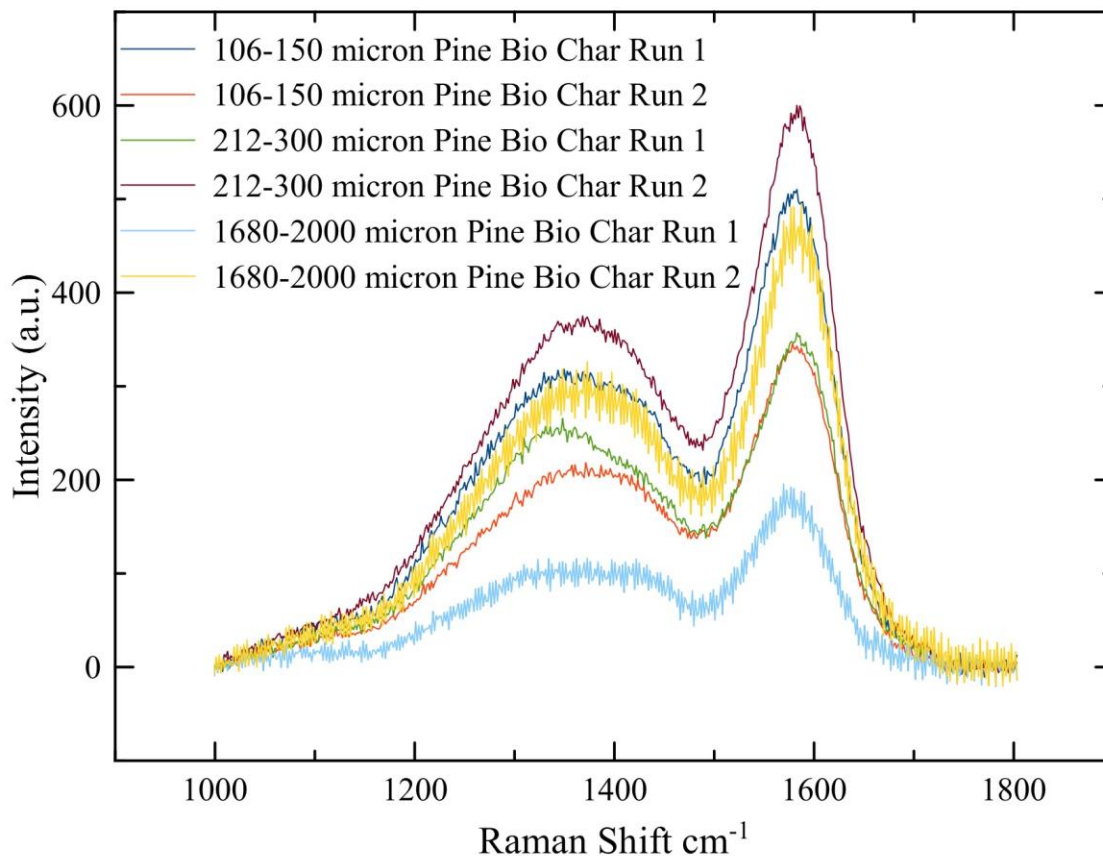


**Figure 28: Raman Spectra for Bio Char of all Particle Sizes and Runs**

Figure 28 is a plot of all the Raman spectra of all the bio chars together. The overall shape of each run are similar the only change is in the varying intensities of each D and G peak for each run. The D and G peaks all apex at the same Raman shift. The D peaks maximum occurs at  $1350\text{ cm}^{-1}$ . The much sharper G peaks reach maximum intensity at  $1580\text{ cm}^{-1}$ . The D peak is a much less intense and more rounded peak than the G peak. This indicates a disordered clustering of highly ordered carbon ring formations of 6 carbons or more but in a randomly ordered network. The sharper G peaks indicates graphitic crystalline structures and aromatics of 5 carbons or less (Kim, 2011). These compounds are the closest to the aromatic structures that could be found in the bio-oil. Since they are found in the bio-oil and no furan structure was found using the Raman microscope, all furan ring compounds and smaller must all have been hydrolyzed. This makes sense due to the presence of furfural and 5-HMF in the bio-oil samples found with the HPLC.

The varying change of intensities of the peaks for the different samples can be explained by different error factors. These could be due to changing of the specimen, different focusing of the laser, or background noises. Even so the respective peak shapes do not change very much and indicate reproducibility of the experiments and confirm the presence of high carbon count rings

and aromatics of 5 carbons or less. The location of the apexes of the D and G peaks did not change at 1350 cm<sup>-1</sup> and 1580 cm<sup>-1</sup> respectively.

Below is the intensity ratio formula which was used to describe the Raman spectra of the different particle size runs for comparison. With this formula, Table 7 demonstrates the calculated values for each run and particle size.

$$\frac{ID}{IG} = \frac{\text{Intensity of D peak}}{\text{Intensity of G peak}}$$

**Table 7: Particle Size and Intensity Ratio**

<b>Particle Size (µm)</b>	<b>Run 1 ID/IG ratio</b>	<b>Run 2 ID/IG ratio</b>
106-150	0.6	0.571
212-300	0.714	0.617
1680-2000	0.684	0.644

The ID/IG ratios varied from 0.517-0.714 but in no particular order. This shows no trend in the increasing particle sizes as far as the material properties of the bio-char. The Raman spectra did support the information found by the HPLC analysis of the bio-oil and FT-IR analysis of bio-char. The D peak revealed the formation of aromatics containing 6 or more rings, much like the structure of lignin. The G peak demonstrated the bio-char as having amorphous sp<sup>2</sup> bonded carbons and aromatics with 5 benzene rings or lower. This does not conclude any new findings however it does support the findings of the other measurements used to analyze the bio-oil and bio-chars as well as show material properties of the bio-char. It could be concluded that the leftover bio-char was the remaining lignin and limited cellulose left over from the original biomass that did not hydrolyze.

### 5.5 Total Organic Carbon Analysis

The total carbon concentration of raw filtered liquid from the reactor was found using a TOC analyzer. Samples were diluted from the reactor by a factor of approximately 300 before being analyzed to ensure that the final signal fell within the calibration curve of the instrument. Carbon concentrations of raw liquid filtered from the reactor are summarized in Figure 29. Carbon concentrations of bio-oil produced from raw pine wood are summarized in Figure 30. Figure 30 includes error bars because of the uncertainty associated with the total quantity of bio-oil produced from raw pine wood. Total carbon analysis showed significant changes in carbon concentration for different experiments.

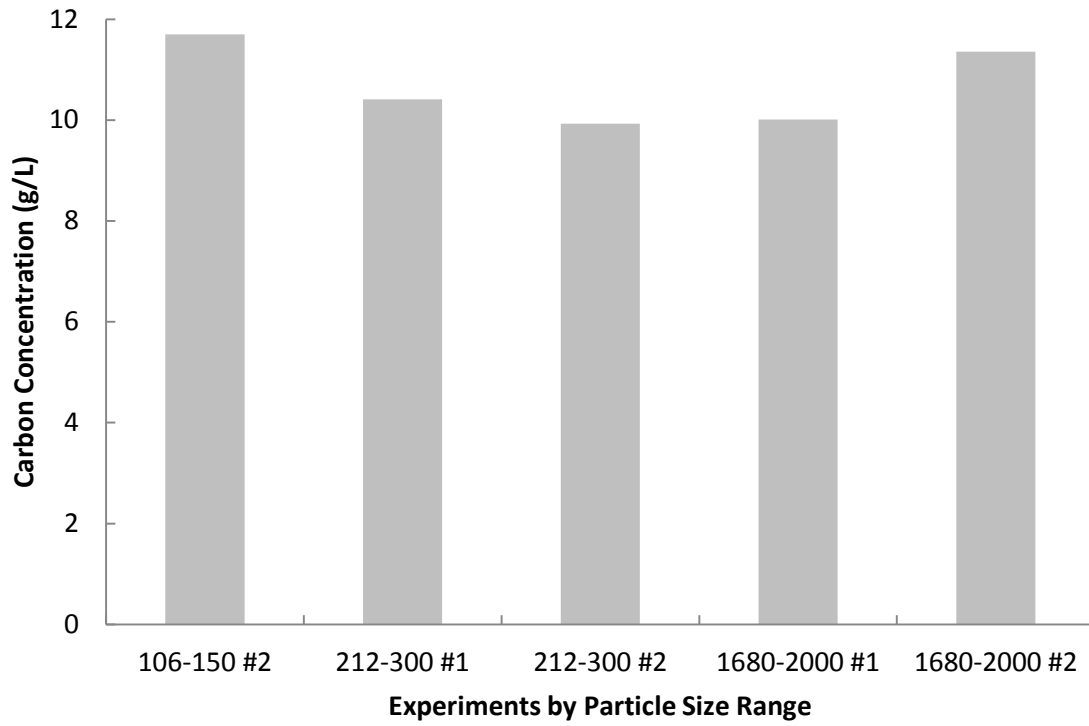


**Figure 29: Carbon Concentration of Raw Filtered Liquid Removed from Reactor upon Experiment Completion**

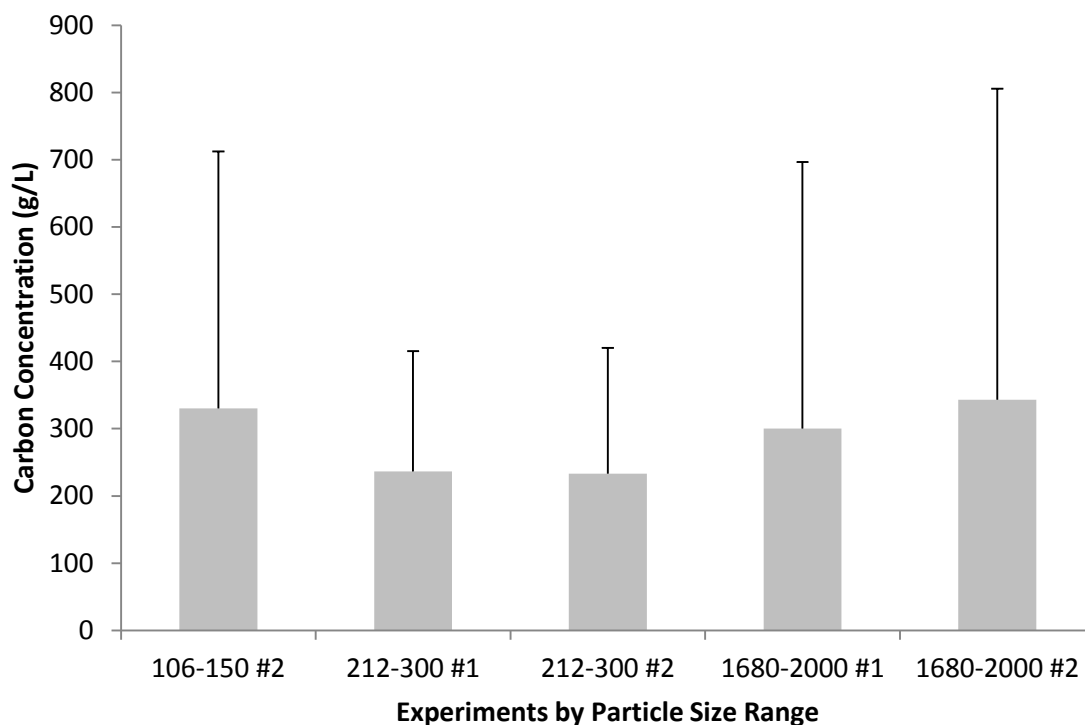


**Figure 30: Carbon Concentration of Bio-oil Produced from Pine Wood**

Experiments 212-300  $\mu\text{m}$ , and 1680-2000  $\mu\text{m}$  #1 have significantly lower carbon concentrations than other experiments. Though there does not appear to be a trend correlating particle size to carbon content, the changes in carbon concentration appear significant enough to be attributed to some change in experimental conditions or procedure. Degradation is not speculated as being the cause of differences since the 1680-2000  $\mu\text{m}$  #2 run and the 106-150  $\mu\text{m}$  #2 run represent the shortest and longest duration between analysis and production, respectively. These two experiments then would be expected to vary greatly; however, their carbon content is very similar. Rotary evaporation can be eliminated as a cause of carbon concentration differences since the TOC analysis was performed on raw gravity filtered liquid removed from the reactor. Slight variations in mass of solids fed to the reactor could contribute to slight differences in carbon concentration but it is not predicted to affect carbon concentrations to the extent shown. Because target temperature and target pressure remained constant across all experiments, the heating rate and cooling rate would then be possible factors for carbon concentration differences. Lowering heating and cooling rates could lead to longer residence times and the possibility of increasing solid residue or gas formation. Solid residue can form over time as secondary reactions and recombination occurs.

The relationship between heating rate and TOC concentration was studied and is represented in Figure 31. Specifically, the average heating rate for each run was considered when the temperature was rising above 200  $^{\circ}\text{C}$  towards the target temperature of 300  $^{\circ}\text{C}$ . 200  $^{\circ}\text{C}$  was

chosen as a temperature where heating rate appeared to change linearly with temperature and 200 °C is near the temperature when reactions forming bio-oil are expected to begin. These heating rates equate to residence times varying between 44-60 minutes. Figure 31 demonstrates that there is a slight correlation between the heating rate and the total carbon concentration with an  $R^2$  value of 0.398. It is important to note that the significance of the correlation would increase without the outlier at 3.18 °C/min. Due to the low quantity of data points, this phenomenon should be tested for repeatability and over a greater range. If it was found that no correlation existed between heating rate and TOC concentration, this would further support literature findings from Kumar who found that residence times past 40 minutes causes a plateau in TOC concentration of the liquid phase (Kumar, 2009). This concludes that with the limited data used from our findings, carbon concentration trends with varying residence times do not agree with Kumar. But, in order to gain a better understanding of these experimental results, more studies must be performed.

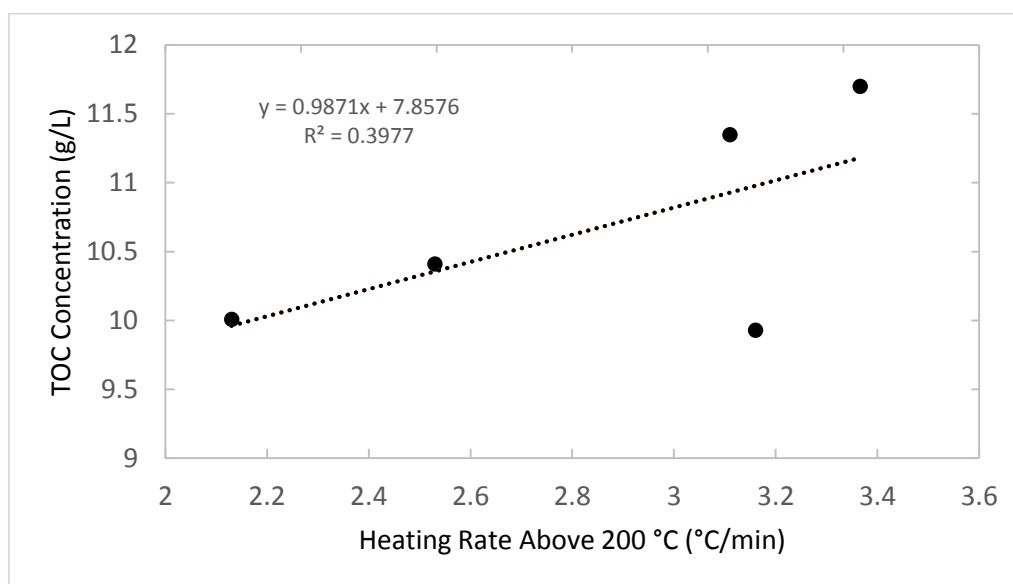


**Figure 31: TOC Concentration Compared to Heating Rate when the Reactor Temperature was Increasing Above 200 °C**

## 5.6 Computations

The thermochemistry of key reactions were modeled using several levels of theory and were compared with energies calculated using higher levels of theory in the literature (Assary, 2010), (Assary, 2012), (Nimlos, 2006). Reaction formulas for the reactions studied appear in Figure 32 and reaction energies for reactions 1 and 2 are listed in Table 8. Total reaction enthalpies and landscapes were observed to vary greatly depending on the theory used for calculation. Energies compared for the first two reactions indicate that B3LYP 6-31G\* and Hartree Fock 6-31G\* emulate the reaction enthalpy changes and free energy changes calculated by the G4 level of theory. A landscape diagram of these reactions is shown in Figure 33. Free energy changes indicate that the formation of 5-HMF from fructose is favored, posing a potential explanation as

to why 5-HMF produced such an intense peak in chromatograms generated by the UV/Vis detectors.  $\Delta E(e)$  refers to total electronic reaction energy changes.  $\Delta E(0)$  refers to reaction energy changes with zero point energies included.  $\Delta H(298K)$  refers to reaction enthalpy changes at 298K.  $\Delta G(298K)$  refers to reaction free energy changes at 298K.

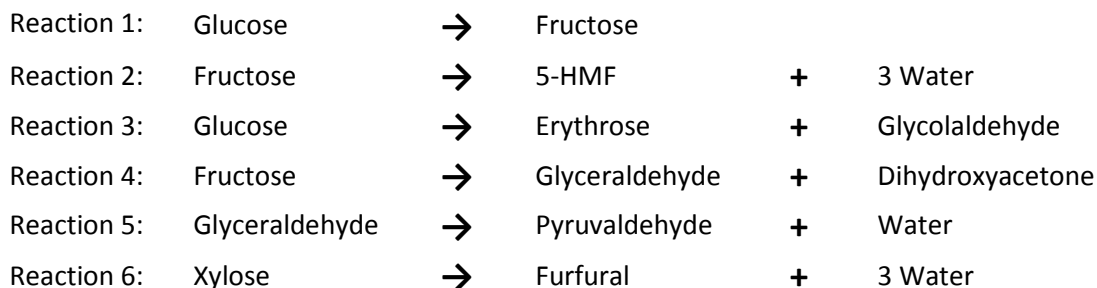


**Figure 32: Six Reactions Modeled Using Various Levels of Theory**

**Table 8: Energies Calculated for 2 Reactions Compared to the Same Reactions Modeled Using the G4 Theory.  $\Delta E(e)$  Represents Total Electronic Energy,  $\Delta E(0)$  Represents Reaction Energy Changes with Zero Point Energy Included,  $\Delta H(298K)$  Represents Reaction Enthalpy at 298K, and  $\Delta G(298K)$  Represents Free Energy Changes at 298K. Reaction 1 is the Glucose to Fructose Isomerization. Reaction 2 is the Reaction of Fructose to 5-HMF**

Energy in kcal/mol Method	Reaction 1				Reaction 2			
	$\Delta E(e)$	$\Delta E(0)$	$\Delta H(298K)$	$\Delta G(298K)$	$\Delta E(e)$	$\Delta E(0)$	$\Delta H(298K)$	$\Delta G(298K)$
G4 (Assary et al.)	2.6	2	2.1	1.9	36	7.8	12.4	-22.9
B3LYP 6-31G*	4.9	-0.9	4.3	3.4	23.4	-12.5	15.1	-19.3
HF 6-31G*	5.5	-0.9	4.8	5.7	51.9	-18.0	37.3	5.0
B3LYP 6-311+G**	5.1	-1	4.5	3.5	-1.2	-12.1	-9.2	-43.2
PM3	-4.9	0.33	-4.4	-5.8	34	-10.5	27.0	-5.0
AM1	-0.2	-0.4	-0.4	-1.7	-0.5	0.2	-0.3	-0.3

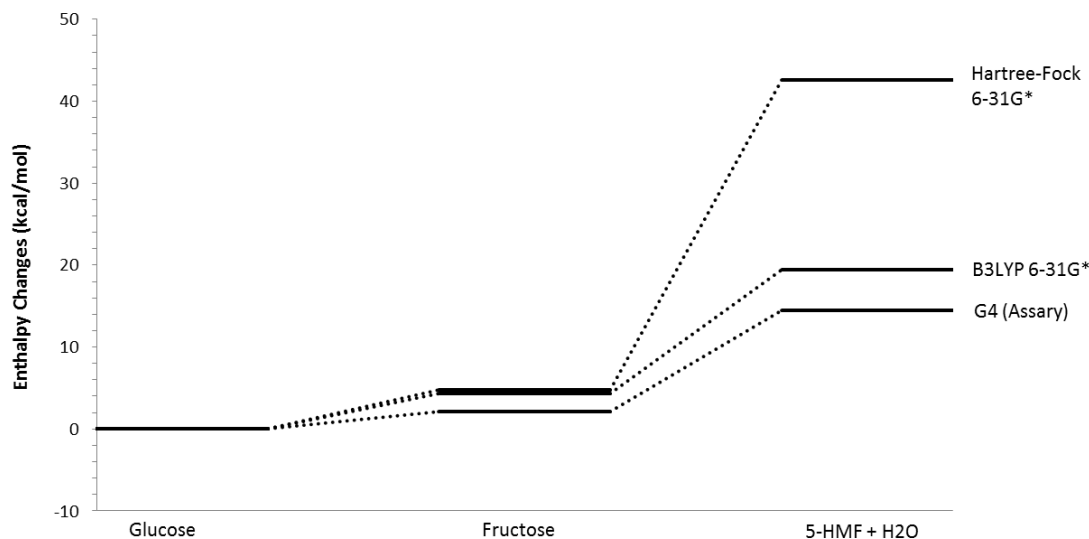


**Figure 33: Enthalpy Landscape Diagram Comparing Calculation Methods for Glucose to Fructose Isomerization and Fructose to 5-HMF**

Energies of reactions 3, 4, and 5 were compared with the results generated from Assary et al in Table 9. In reaction 3, B3LYP 6-31G\* and AM1 emulate the sign or endothermic behavior (qualitative data) of the energy generated by the G4 theory, though none of the attempted theories match the G4 theory quantitatively. Reaction 4 demonstrates that none of the proposed theories could quantitatively or qualitatively agree with the energies generated from the G4 level of theory. Reaction 5 shows that all theories agree qualitatively with the data generated from the G4 level of theory except for AM1. The negative free energy changes seen in reaction 5 also indicate that the production of pyruvaldehyde from glyceraldehyde is favored. Hartree-Fock 6-31G\* showed strong quantitative agreement with the energies calculated using the G4 level of theory and B3LYP 6-31G\* showed mild quantitative agreement with the G4 level of theory. In most of the reactions proposed thus far, the B3LYP 6-31G\* and Hartree-Fock 6-31G\* methods proved qualitatively accurate with inconsistent quantitative agreement. The discrepancies in reaction 3 and 4 from our attempted methods with the G4 method are attributed to slight variations in fructose and glucose geometries. It was observed that rotations of hydroxyl groups could result in significantly different energies. Geometries of glucose and fructose should be unified between methods of comparison in order to determine the effectiveness of theories used for reactions involving glucose and fructose.

**Table 9: Energies Calculated for 3 Reactions Compared to the Same Reactions Modeled Using the G4 Theory.  $\Delta H(298K)$  Represents Reaction Enthalpy at 298K, and  $\Delta G(298K)$  Represents Free Energy Changes at 298K. Reaction 3 is the Conversion of Glucose to Erythrose and Glycolaldehyde. Reaction 4 is the Conversion of Fructose to Glyceraldehyde and Dihydroxyacetone. Reaction 5 is the Conversion of Glyceraldehyde to Pyruvaldehyde and Water.**

Energy in kcal/mol Methods	Reaction 3		Reaction 4		Reaction 5	
	$\Delta H(298K)$	$\Delta G(298K)$	$\Delta H(298K)$	$\Delta G(298K)$	$\Delta H(298K)$	$\Delta G(298K)$
G4 (Assary et al.)	34.3	18.1	26.9	10.3	-6.9	-18.7
B3LYP 6-31G*	18.1	1.3	-0.8	-16.0	-1.2	-12.8
Hartree-Fock 6-31G*	15.3	-0.7	0.6	-15.0	-5.2	-17.2
PM3	2.3	-13.0	-2.2	-17.7	-2.3	-14.0
AM1	18.0	3.7	6.5	-8.5	8.1	-3.9

Table 10 shows energies calculated for the conversion of xylose to furfural and water. Calculated energy changes including zero point energies appear to agree well with the energies calculated by Nimlos et al. All tested methods agree qualitatively and quantitatively. However, enthalpy and free energy changes disagree across methods considered. Because Hartree-Fock 6-31G\* is a higher level method and has been shown to model previous reactions well, it is considered qualitatively accurate with respect to enthalpy and free energy changes of reaction 6. Therefore the reaction from xylose to furfural is considered favorable due to the negative free energy change.

**Table 10: Energies Calculated for Reaction 6, the Conversion of Xylose to Furfural and Water.  $\Delta E(e)$  Represents Total Electronic Energy,  $\Delta E(0)$  Represents Reaction Energy Changes with Zero Point Energy Included,  $\Delta H(298K)$  Represents Reaction Enthalpy at 298K, and  $\Delta G(298K)$  Represents Free Energy Changes at 298K. Calculated Energies Are Compared to Calculated Reaction Energy from Nimlos et al.**

Energy in kcal/mol Methods	Reaction 6			
	$\Delta E(e)$	$\Delta E(0)$	$\Delta H(298K)$	$\Delta G(298K)$
CBS-QB3 (Nimlos et al.)	N/A	-13.2	N/A	N/A
6-31G*	31.2	N/A	N/A	N/A
HF 6-31G*	23.6	-15.6	13.4	-23.0
PM3	13.6	-11.5	7.6	-29.2
AM1	44.3	-14.8	38.5	2.9

## 5.7 Final Discussion and Considerations

Measurement and product collection techniques resulted in significant error associated with the final mass balance. First, gas products produced could not be collected for composition analysis

and proper pressure gauges were not present to understand the pressure exerted by gases formed. Second, a significant amount of wet solid product could not be removed entirely without performing an acetone wash. Acetone is highly volatile and although a known amount was measured to wash, unknown amounts of acetone were lost to evaporation before proper massing could take place. Because only dried solids could be massed definitively, liquid product that was present in the solid was inferred based on the sum of total solid mass produced and an assumed amount of gas produced. The assumed amount of gas produced was based on the gas produced in a study which used very similar conditions to this study (Cheng, 2010). Third, volatile liquid products were likely to have evaporated during the retrieval of products from the reactor. These three factors introduced significant error to the mass distribution of all phases. Interestingly, several procedures in the literature involve performing an acetone wash followed by a reduced pressure rotary evaporation. None of the studies investigated discussed the issues surrounding the volatility of acetone. However, most studies that were investigated rigorously measured the quantity and composition of gas produced from the reaction allowing any product that is unaccounted for to be attributed to the liquid phase.

Final mass balances indicated that there was no correlation between liquid oil yield and particle size within the parameters of this study while considering the uncertainty involved. This conclusion was supported by the HPLC, TOC, Raman, and FT-IR analyses which showed no significant changes in product quality between varying pinewood particle sizes. The conclusion agrees with what was found in a study by Zhang who showed no increase in bio-oil yield when particle size was decreased (Zhang, 2009). The HPLC analysis demonstrated that no significant variations existed in product compound distribution across the different particles sizes chosen in this study. This result was somewhat anticipated considering the high residence time within the reactor which varied between 139-182 minutes overall and 44-60 minutes above 200 °C. Kumar had found that during a reaction with a target temperature of 235 °C, the bio-oil TOC concentration plateaued after 40 minutes of residence time (Kumar, 2009). Though this does not directly imply that the compound distribution would be maintained after 40 minutes, it does show that the different phases of the product reach equilibrium with no additional reactions occurring that would alter the phase distribution. Given the current study operated at a target temperature of 300 °C, it is expected that the equilibrium point would be reached sooner than found by Kumar. Although the product compound distribution was unaffected by the particle size and appeared to reach equilibrium, there was still slow degradation occurring within the bio-oil phase demonstrated by the HPLC UV/Vis chromatograms. This was observed physically by the darkening of bio-oil solutions and the precipitation of solid particles within bio-oil samples several days after being produced. This demonstrates that reactions still proceed, but they proceed very slowly.

Significantly more solid residue was formed during this study than was reported to have been formed by studies listed in Table 2. Solid residue produced accounted for 45-60 wt % of initial biomass fed to the system during this study, while other sources, such as Cheng et al., reported

that solid residue accounted for only 30 wt % of initial biomass (Cheng, 2010). A possible explanation for the increased solid residue is the relatively low heating rate, and therefore high residence time compared to other studies. Akhtar discussed how low heating rates led to char formation due to secondary reactions and recombination (Akhtar, 2011).

The FT-IR analysis showed that cellulose and lignin existed in the final solid residue. However, the FT-IR spectrum of solid residue from reactions showed a lesser presence of cellulose than the FT-IR spectrum of raw pine wood. Karagöz et al. found that pure cellulose experienced a 70.1 wt % conversion under HTL conditions while lignin experienced only a 40 wt % conversion (Karagöz, 2005). This agrees with the FT-IR findings of the solid product because more lignin appears to be present in the final solid residue than cellulose when compared to raw pine wood. But, with ample amounts of esters, aromatic rings, and aldehydes present in the bio-char FT-IR spectrum, some cellulose depolymerized and remained as a solid. Further experiments would have to be performed to gain enough data to accurately quantify the conversion.

The Raman analysis indicated that there is no relation between particle sizes and material properties of the bio-char. Although no new information was discovered, the Raman supported the analyses of the HPLC UV/Vis chromatograms and the FT-IR spectrums. The G peak shape and intensity indicated that there were aromatic structures of 5 carbons or less and amorphous  $sp^2$  bonded carbons (Kim, 2011). These structures relate most similarly to the aromatic ring structures found in the HPLC analysis. Due to the presence of furfural and 5-HMF found with the UV/Vis detector, this signifies that all furan ring compounds and smaller must have been hydrolyzed. Also the D peak revealed aromatic structures of 6 or more rings, similar to that of lignin. As expected, this represents the low conversion of lignin and supports the findings of the FT-IR spectrums.

The TOC analysis did not indicate that particle size affects the TOC concentration of the liquid product produced from the HTL process. However, the significant variations in TOC concentrations across samples implied that other factors were significantly affecting the TOC concentrations. Heating rate was considered as it was a measured and variable parameter that was difficult to unify across all experiments. A trend was noted when TOC concentration was compared to the heating rate of material while the reactor was heating from 200-300 °C, which was considered a temperature range high enough to initiate reactions. The trend indicated that TOC concentration increased with increased heating rate. Zhang et al. found that increasing heating rate from 4 °C/min to 140 °C/min resulted in an additional 13 wt% of initial biomass converted to bio-oil (Zhang, 2009). The additional bio-oil yield was matched by an equal decrease in solid residue while the gas produced remained the same. Findings from Zhang et al. support the trend observed in this study with respect to TOC concentration of liquid products retrieved from the reactions. Oddly, a similar increase in bio-oil production was noted in this study (14 wt % from TOC analysis) and the study by Zhang et al despite having extremely different increases in heating rate. Because of this, the increase in TOC concentration across experiments is considered to be affected by more factors than heating rate alone. Future studies

identifying and controlling single parameters would have to be performed to understand why there is variation in TOC concentration.

Computational studies of key reactions in the HTL process revealed that the B3LYP 6-31G\* and Hartree-Fock 6-31G\* theories were sufficient for approximating some of the key reactions in this process. The high accuracy energy results attained from the literature were used for comparison between methods also indicated which reactions were most favorable. The formation of 5-HMF was noted to be a favorable reaction from the negative free energy change. 5-HMF was also noted as a significant product from the UV/Vis chromatograms. The formation reactions of C3 and C4 sugars such as glyceraldehyde, glycolaldehyde, and dihydroxyacetone were found to be unfavorable though these sugars appeared to dominate the final solution according to ELSD chromatograms. This analysis does not consider reaction rates, which could be much higher for the formation of these C3 and C4 sugars, leading to greater formation.

## 6. Conclusions

A series of experiments were performed in order to investigate the effects that particle size of biomass feed has on product phase distribution and compound distribution. Particle size was shown to have no effect on product phase distribution when considered within the bounds of uncertainty. Hydrothermal liquefaction primarily resulted in solid char formation and water soluble liquid products. Small amounts of gas were produced but were not measured in this study. Although the phase distribution remained unchanged across all feed particle sizes, it was found that more liquid phase could be easily separated from the product slurry when larger particle sizes were used. This is due to larger spaces between particles and less available surface area to adhere to. It was also found that larger feed particle sizes resulted in less adherence to internal components of the reactor. Concentrated liquid samples from the liquefaction process were analyzed using an HPLC system with a UV/Vis detector and ELSD. Cellobiose, glucose, 5-HMF, and furfural were definitively identified within the concentrated samples. Xylose, fructose, and tetrose and triose sugars are assumed to elute shortly after glucose, but lack of standard solutions or defined peaks make that determination difficult. The chromatograms indicated that almost no cellobiose or larger saccharides were present in the concentrated solutions, indicating that the reaction depolymerized all saccharides present. The chromatograms indicated that particle size of initial feed had little effect on the liquid phase compound distribution. The total organic carbon analysis supported the other analyses in that it showed no correlation between carbon concentration and particle size. The total organic carbon analysis did demonstrate how other factors such as heating and cooling rates are significantly affecting the final carbon concentration. It appears that no additional mass transfer limitations are introduced by increasing particle size under the current reaction conditions. Larger particle sizes considered during this study should provide equal quality bio-oil compared to bio-oil produced from smaller particle sizes with the benefit of reduced milling costs and less adherence to internal equipment.

There was relatively no change observed in the FT-IR and Raman spectra with the different particle sizes tested. The FTIR and Raman tests did confirm that most of the larger lignin structures were left behind after the hydrolysis was performed. The FTIR detailed the actual components of the bio-char while the Raman confirmed the findings of the FTIR by identifying the larger 6 and 5 ring aromatic structures of the char. These larger multi-ring formations are indicative of the large random networks of aromatics that lignin is composed of. This means that most of the lignin is left behind as bio-char after the hydrothermal liquefaction has taken place in a batch reactor system.

The computational analysis of several levels of theory on the thermochemistry of reactions taking place during hydrothermal liquefaction indicate that the B3LYP 6-31G\* and Hartree-Fock 6-31G\* are suitable for approximating enthalpy and free energy trends. This is assuming accurate molecule geometries are used. The calculated free energies also indicate that the production of 5-HMF from fructose, the production of pyruvaldehyde from glyceraldehyde, and the production of furfural from xylose are favored reactions.

## 7. Recommendations

For future studies that perform hydrothermal liquefaction in a batch setup, it is recommended to include some means to measure the total mass of the gas phase. This could be accomplished by attaching an accurate low pressure gauge and gas bag to the reaction vessel. The pressure gauge would allow the user to measure the pressure of the newly produced gas phase and the gas bag would allow gas capture for composition analysis. Once gas composition and pressure is known, a calculation using the ideal gas law can be performed to understand total mass of the gas phase. Product handling methods should be improved to reduce error on the final mass balance. Acetone is an excellent solvent for the materials being recovered from the reactor but has a high vapor pressure and therefore undesirably evaporates. The evaporation disrupts the final mass balance and introduces error. A solution to this issue would be to cool the reactor, its contents, and the acetone wash to a temperature near the freezing point of water in order to lower the evaporation rate. Because heating and cooling rates potentially affected the total organic carbon analysis, it is recommended to monitor and control the conditions of the experiment as closely as possible. In combination, future studies may perform multiple reactions with the same parameters but different heating and cooling rates to understand the specific effect that heating and cooling rate has on the products formed.

Because it was shown that mass transfer limitations were not affected by particle size at the current conditions, it is recommended to test fast hydrothermal liquefaction. This can be done by injecting pressurized slurry of biomass into preheated compressed water. The process should be followed by immediate quenching, thus reducing residence time by as much as possible. This immediate heating and cooling should illuminate mass transfer limitations, kinetics, and potential intermediate reactions of the hydrothermal liquefaction of pine wood.

Though the B3LYP 6-31G\* and Hartree-Fock 6-31G\* methods appear to accurately approximate the thermochemistry of many of the reactions participating in hydrothermal liquefaction, there appears to be significant sensitivity issues regarding molecule geometry. Specifically, geometries of larger sugar molecules such as fructose and glucose are very sensitive when determining final energy changes. Higher levels of theory should be tested to understand if sensitivity to geometries can be reduced in order to produce more consistent thermochemical trends.

## 8. References

- Aarhus University. "Hydrothermal Liquefaction – the most promising path to a sustainable bio oilproduction." *Science Daily* (2013).
- Aida, Taku Michael, et al. "Reactions of d-fructose in water at temperatures up to 400° C and pressures up to 100MPa." *The Journal of supercritical fluids* 42.1 (2007): 110-119.
- Aida, Taku Michael, et al. "Reaction kinetics of D-xylose in sub-and supercritical water." *The Journal of Supercritical Fluids* 55.1 (2010): 208-216.
- Akhtar, Javaid, and Nor Aishah Saidina Amin. "A review on process conditions for optimum bio-oil yield in hydrothermal liquefaction of biomass." *Renewable and Sustainable Energy Reviews* 15.3 (2011): 1615-1624.
- Anderson, Nathaniel, et al. "A Comparison of Producer Gas, Biochar, and Activated Carbon from Two Distributed Scale Thermochemical Conversion Systems Used to Process Forest Biomass." *Energies* 6 (2013): 164-183.
- APHA, AWWA, and WEF (American Public Health Association, American Water Works Association, and Water Environment Federation). 1998. Part 5310 Total Organic Carbon: 5310 D. Wet- Oxidation Method. *Standard Methods for the Examination of Water and Wastewater*. 20<sup>th</sup> Edition. Washington, D.C.; APHA.
- Assary, Rajeev S., et al. "Computational studies of the thermochemistry for conversion of glucose to levulinic acid." *The Journal of Physical Chemistry B* 114.27 (2010): 9002-9009.
- Assary, Rajeev S., and Larry A. Curtiss. "Comparison of sugar molecule decomposition through glucose and fructose: A high-level quantum chemical study." *Energy & Fuels* 26.2 (2012): 1344-1352.
- Byrd, James. "Interpretation of Infrared Spectra." Infrared Absorption Frequencies. California State University Stanislaus, 1 May 1998. Web. 25 Feb. 2014. <<http://www.chem.csustan.edu/Tutorials/INFRARED.HTM>>.
- Cheng, Jay, Timilsina, Govinda. "Status and barriers of advanced biofuel technologies: A review". *Renewable Energy* 36 (2011): 3541-3549.
- Cheng, S., D'cruz, I., Wang, M., Leitch, M., Xu, C., 2010. "Highly Efficient Liquefaction of

- Woody Biomass in Hot-Compressed Alcohol – Water Co-solvents”. *Energy & Fuels* 24, 4659-4667.
- Curtiss, Larry A., Paul C. Redfern, and Krishnan Raghavachari. "Assessment of Gaussian-3 and density-functional theories on the G3/05 test set of experimental energies." *The Journal of chemical physics* 123.12 (2005): 124107.
- Curtiss, Larry A., Paul C. Redfern, and Krishnan Raghavachari. "Gaussian-4 theory." *The Journal of chemical physics* 126.8 (2007): 084108.
- Faeth, Julia L., Peter J. Valdez, and Phillip E. Savage. "Fast hydrothermal liquefaction of Nannochloropsis sp. to produce biocrude." *Energy & Fuels* 27.3 (2013): 1391-1398.
- Ferrari, A. C., and J. Robertson. "Interpretation of Raman spectra of disordered and amorphous carbon." *Physical review B* 61.20 (2000): 14095.
- Glazer, A. W., and Nikaido, H. (1995). *Microbial Biotechnology: fundamentals of applied microbiology*. San Francisco: W. H. Freeman, p. 340. ISBN 0-71672608-4
- Karagöz, Selhan, et al. "Comparative studies of oil compositions produced from sawdust, rice husk, lignin and cellulose by hydrothermal treatment." *Fuel* 84.7 (2005): 875-884.
- Karagöz, Selhan, et al. "Low-temperature hydrothermal treatment of biomass: effect of reaction parameters on products and boiling point distributions." *Energy & fuels* 18.1 (2004): 234-241.
- Kim, Pyoungchung, et al. "Surface functionality and carbon structures in lignocellulosic-derived bio-chars produced by fast pyrolysis." *Energy & Fuels* 25.10 (2011): 4693-4703.
- Kumar, Sandeep, and Ram B. Gupta. "Biocrude production from switchgrass using subcritical water." *Energy & Fuels* 23.10 (2009): 5151-5159.
- Kumar, Sandeep. *Hydrothermal Treatment for Biofuels: Lignocellulosic Biomass to Bioethanol, Biocrude, and Bio-char*. Diss. Auburn University, 2010. N.p.: n.p., n.d. Print.
- Lange, Jean-Paul. "Lignocellulose conversion: an introduction to chemistry, process and economics." *Biofuels, Bioproducts, and Biorefining* 1.1 (2007): 39-48.
- Liu, Aiguo, et al. "Product identification and distribution from hydrothermal conversion of walnut shells." *Energy & fuels* 20.2 (2006): 446-454.
- Malherbe, S., and T. E. Cloete. "Lignocellulose Biodegradation: Fundamentals and

- Applications." *Springer*. Kluwer Academic Publishers, n.d. Web. 31 Oct. 2013. <<http://www.easybib.com/cite/form/website>>.
- Matsumura, Yukihiro, et al. "Supercritical water treatment of biomass for energy and material recovery." *Combustion Science and Technology* 178.1-3 (2006): 509-536.
- Mosteiro-Romero, M., Vogel, F., Wokaun, A. "Liquefaction of wood in hot compressed water: Part1 – Experimental results." *Chemical Engineering Science*. (2014). Print.
- Nimlos, Mark R., et al. "Energetics of xylose decomposition as determined using quantum mechanics modeling." *The Journal of Physical Chemistry A* 110.42 (2006): 11824-11838.
- Pandey, K. K. "A study of chemical structure of soft and hardwood and wood polymers by FTIR spectroscopy." *Journal of Applied Polymer Science* 71.12 (1999): 1969-1975.
- Peterson, Andrew A., Frédéric Vogel, Russell P. Lachance, Morgan Fröling, Michael J. Antal, Jr., and Jefferson W. Tester. "Thermochemical Biofuel Production in Hydrothermal Media: A Review of Sub- and Supercritical Water Technologies." *Energy & Environmental Science* 1.1 (2008): 34-38. Print.
- Petrova, Elitza, Savcho Tinchev, and Petranka Nikolova. "Interference effects on the ID/IG ratio of the Raman spectra of diamond-like carbon thin films." *arXiv preprint arXiv:1112.0897* (2011).
- Qu, Yixin, Xiaomin Wei, and Chongli Zhong. "Experimental study on the direct liquefaction of *Cunninghamia lanceolata* in water." *Energy* 28.7 (2003): 597-606.
- Sanna, Aimaro. "Advanced Biofuels from Thermochemical Processing of Sustainable Biomass in Europe." *Bioenergy Research* (2013): n. page. Print.
- Sasaki, Mitsuru, et al. "Cellulose hydrolysis in subcritical and supercritical water." *The Journal of Supercritical Fluids* 13.1-3 (1998): 261-268.
- Sasaki, Mitsuru, et al. "Kinetics and mechanism of cellobiose hydrolysis and retro-aldol condensation in subcritical and supercritical water." *Industrial & engineering chemistry research* 41.26 (2002): 6642-6649.
- Scheller, Henrik V., and Peter Ulvskov. "Hemicelluloses." - *Annual Review of Plant Biology*, 61(1):263. Annual Review of Plant Biology, 29 Jan. 2010. Web. 31 Oct. 2013. <[http://www.annualreviews.org/doi/full/10.1146/annurev-arplant-042809-112315?url\\_ver=Z39.88-2003](http://www.annualreviews.org/doi/full/10.1146/annurev-arplant-042809-112315?url_ver=Z39.88-2003)>.

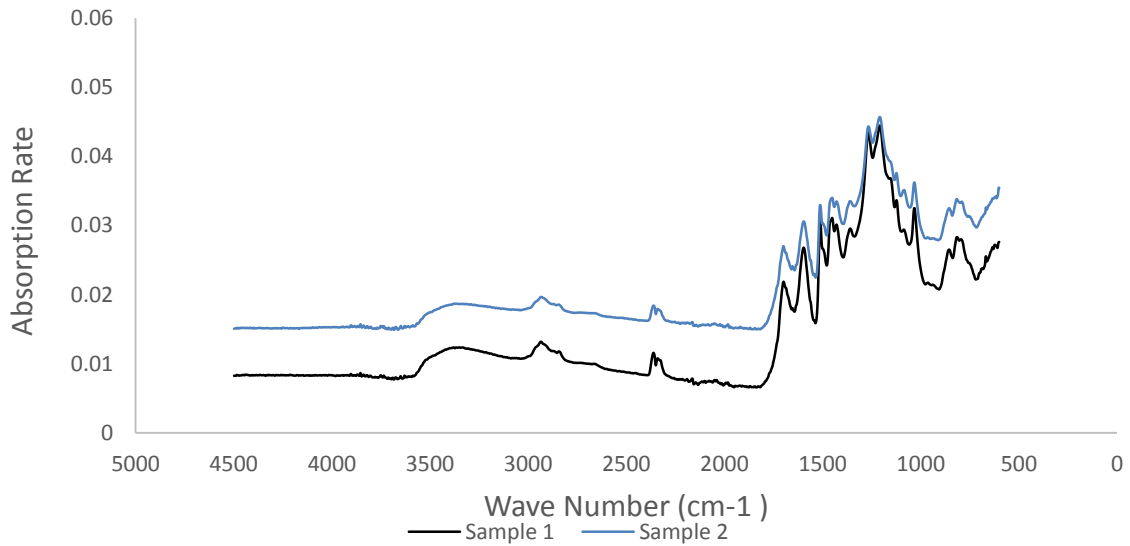
- Schwan, J., et al. "Raman spectroscopy on amorphous carbon films." *Journal of Applied Physics* 80.1 (1996): 440-447.
- Smith, Meghan, and Keener, Harold. "Hydrothermal Liquefaction." *Manure Processing Technologies*. The Ohio State University, 22 Feb. 2014. [http://www.oardc.ohio-state.edu/ocamm/images/MPT\\_3.7\\_hydrothermal\\_liquefaction.pdf](http://www.oardc.ohio-state.edu/ocamm/images/MPT_3.7_hydrothermal_liquefaction.pdf).
- Sugano, Motoyuki, et al. "Hydrothermal liquefaction of plantation biomass with two kinds of wastewater from paper industry." *Journal of Materials Science* 43.7 (2007): 2476-2486.
- Sun, Peiqin, Mingxing Heng, Shao-Hui Sun, and Junwu Chen. "Analysis of Liquid and Solid Products from Liquefaction of Paulownia in Hot-compressed Water." *Energy Conversion and Management* 52.2 (2011): 924-33. Print.
- Thermo Nicolet Corporation. *Introduction to Fourier Transform Infrared Spectrometry*. N.p.: Thermo Nicolet Corporation, 2001. *A Thermo Electron Business*. Web. 22 Feb. 2014. <<http://mmrc.caltech.edu/FTIR/FTIRintro.pdf>>.
- Toor, Saqib Sohail, Lasse Rosendahl, and Andreas Rudolf. "Hydrothermal liquefaction of biomass: A review of subcritical water technologies." *Energy* 36.5 (2011): 2328-2342.
- Vardon, Derek R. *Hydrothermal liquefaction for energy recovery from high-moisture waste biomass*. Diss. University of Illinois, 2012.
- Xu, C., Lad, N., 2008. "Production of Heavy Oils with High Caloric Values by Direct Liquefaction of Woody Biomass in Sub/Near-critical Water". *Energy & Fuels* 22 (1), 635-642.
- Zhang, Yuanhui. "Chapter 10." *Biofuels from Agricultural Wastes and Byproducts*. N.p.: Blackwell, 2010. 201-08. <Http://age-web.age.uiuc.edu/bee/research/IntroHTL.pdf>. Web. 31 Oct. 2013.
- Zhang, Xu, Champagne. "Energy recovery from secondary pulp/paper-mill sludge and sewage sludge with supercritical water treatment." *Biosource Technology*. 101.8 (2010): 2713-2721.
- Zhang, Bo, Marc von Keitz, and Kenneth Valentas. "Thermochemical liquefaction of high diversity grassland perennials." *Journal of Analytical and Applied Pyrolysis* 84.1 (2009): 18-24.

## 9. Appendices

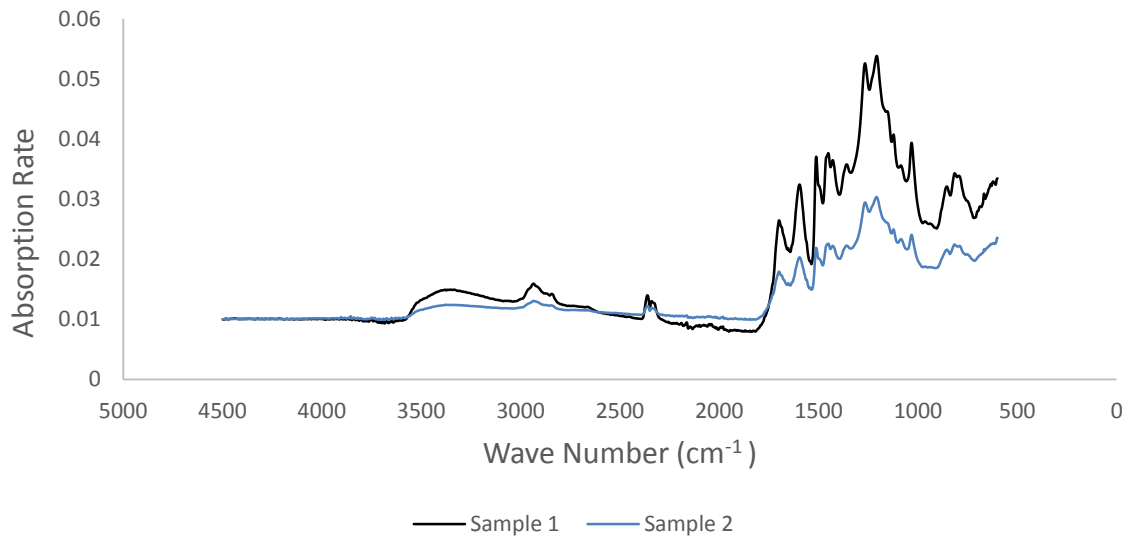
### 9.1 Appendix A: Additional Tables and Figures

#### 9.1.1 FT-IR Spectrums

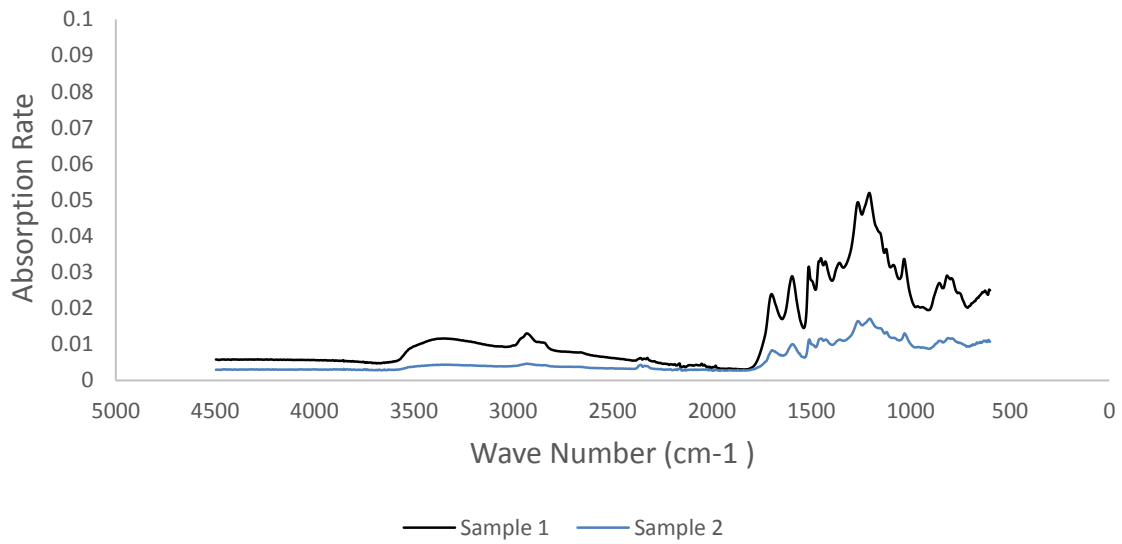
Below are the two spectrums after a background spectrum of the 106-150  $\mu\text{m}$  without normalized baselines.



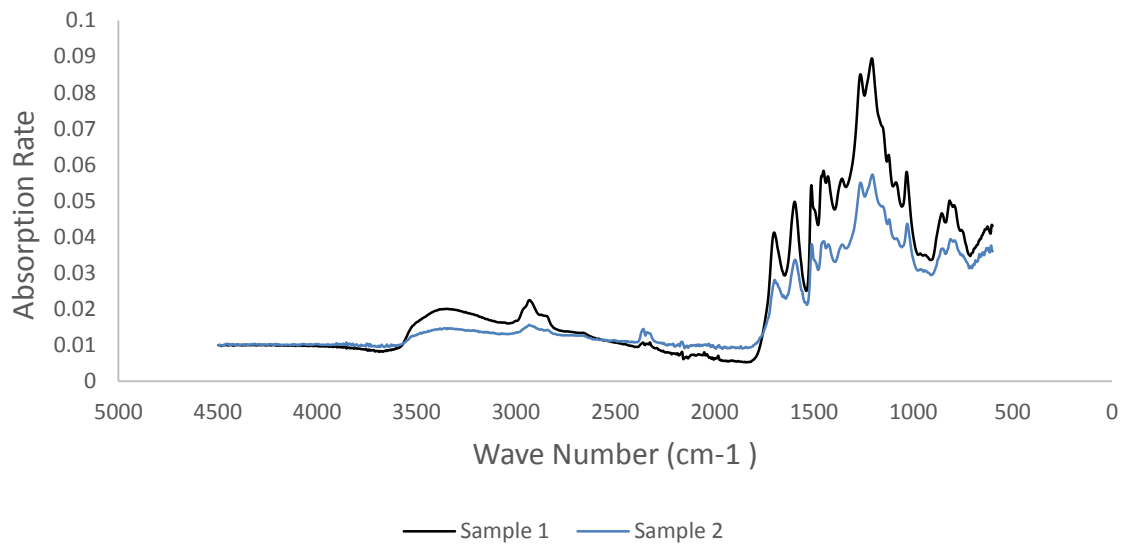
Below are the two spectrums after a background spectrum of the 106-150  $\mu\text{m}$  with normalized baselines.



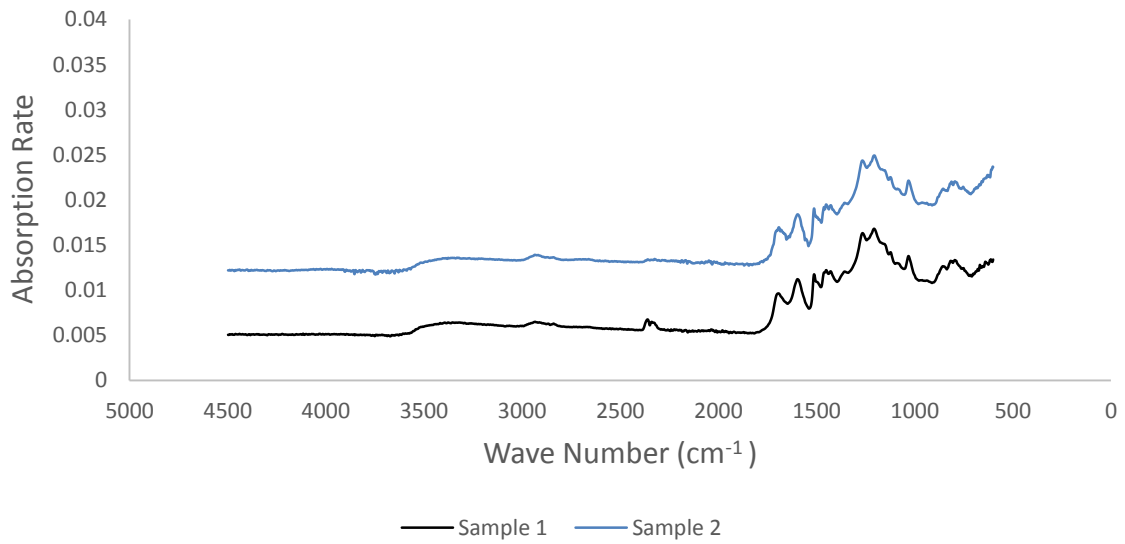
Below are the two spectrums after a background spectrum of the 212-300  $\mu\text{m}$  without normalized baselines.



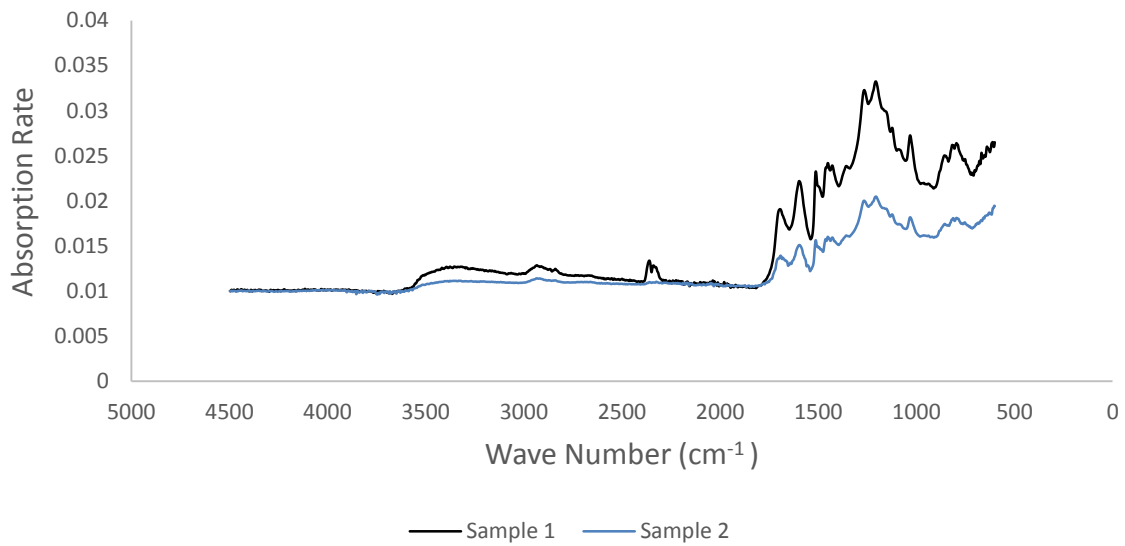
Below are the two spectrums after a background spectrum of the 212-300  $\mu\text{m}$  with normalized baselines.



Below are the two spectrums after a background spectrum of the 1680-2000  $\mu\text{m}$  without normalized baselines.



Below are the two spectrums after a background spectrum of the 1680-2000  $\mu\text{m}$  with normalized baselines.



### 9.1.2 Final Molecule Geometries

All geometries were optimized using B3LYP 6-31G\* except for Xylose which was optimized using Hatree-Fock 6-31G\*. All geometries listed are in XYZ file format.

15

5-HMF

C	0	0	0
C	-1.3125	0.65784	-0.2525
C	-1.6686	1.95872	-0.503
C	-3.0771	1.95809	-0.6873
C	-3.4878	0.65414	-0.5356
O	-2.409	-0.1416	-0.2678
C	-4.8148	0.06052	-0.604
O	-5.0711	-1.1172	-0.4332
H	-5.6085	0.80483	-0.8331
H	-3.7148	2.80468	-0.9034
H	-0.9966	2.804	-0.554
O	0.41215	-0.6812	-1.1826
H	1.13416	-1.2804	-0.9377
H	-0.1087	-0.6968	0.84419
H	0.72235	0.77653	0.2939

24

D-Glucose

C	0	0	0
C	-0.4343	-1.3657	0.53925
O	-1.8149	-1.6127	0.24603
C	-2.6904	-0.6497	0.83317
C	-2.3976	0.71411	0.18831
C	-0.9563	1.08791	0.49248
O	-0.5713	2.30193	-0.1405
H	-1.2539	2.9524	0.09486
H	-0.8415	1.18247	1.58615
O	-3.2394	1.75191	0.68565
H	-4.0953	1.62649	0.24255
H	-2.5174	0.60799	-0.896
C	-4.141	-1.0964	0.65276
H	-4.1639	-2.1941	0.63858
H	-4.7284	-0.7492	1.51502
O	-4.6649	-0.5429	-0.5566
H	-5.5356	-0.9369	-0.7145
H	-2.4905	-0.5854	1.91689
H	-0.3004	-1.3834	1.63734
O	0.31682	-2.3503	-0.0873
H	0.04535	-3.2045	0.28529
O	1.32161	0.26529	0.43518
H	1.49459	1.19111	0.19549
H	-0.0568	-0.0494	-1.0983

24

D-Fructose

C	0	0	0
C	1.35848	0.27916	0.63895
C	1.89418	1.69701	0.37547
C	3.39478	1.51236	0.61436
C	3.63664	0.05697	0.15881
O	2.32645	-0.553	0.04238
C	4.47279	-0.7934	1.11295
O	4.51054	-2.1413	0.68824
H	3.57865	-2.4036	0.59024
H	5.51025	-0.4354	1.13022
H	4.0571	-0.6995	2.12801
H	4.08219	0.04574	-0.8427
O	4.09945	2.50933	-0.1163
H	5.03352	2.47438	0.14096
H	3.58779	1.61283	1.69219
O	1.25771	2.62061	1.24461
H	1.72092	3.4694	1.16214
H	1.74123	1.97032	-0.6785
O	1.34368	0.04545	2.03665
H	1.04205	0.87649	2.44627
O	-0.3875	-1.3272	0.2977
H	-1.2482	-1.481	-0.1189
H	0.09178	0.16866	-1.0845
H	-0.7127	0.73888	0.40134

12

Dihydroxyacetone

C	0	0	0
C	1.31623	0.75585	0.04908
C	2.63248	2.9E-05	0.09816
O	3.73032	0.86513	0.01233
H	3.36155	1.76732	0.06484
H	2.65508	-0.7352	-0.7216
H	2.64794	-0.582	1.03701
O	1.31621	1.9781	0.04918
O	-1.0979	0.86513	0.08517
H	-0.729	1.76732	0.03313
H	-0.0227	-0.7349	0.82006
H	-0.0153	-0.5824	-0.9386

16

Erythrose

C	0	0	0
C	1.23401	-0.6225	0.64513
C	2.53915	-0.0216	0.11046
C	3.75744	-0.7404	0.6895
O	4.58204	-1.3369	0.04238
H	3.85888	-0.6261	1.79711
O	2.6308	1.36998	0.41705
H	2.60414	1.4671	1.38417
H	2.58263	-0.1053	-0.9783
O	1.27054	-2.0154	0.39918
H	0.36338	-2.3297	0.55906
H	1.18116	-0.425	1.73394
O	-1.1149	-0.7043	0.55228
H	-1.9003	-0.5007	0.0238
H	-0.0468	1.07515	0.2163
H	0.05634	-0.1398	-1.0896

11

2-Furfural

C	0	0	0
C	-1.4888	-0.1953	-9E-05
O	-1.9826	-1.484	-0.0005
C	-3.3478	-1.3573	0.00028
C	-3.7184	-0.0658	-0.0004
C	-2.5001	0.69736	-9E-05
H	-2.4108	1.772	-5E-05
H	-4.7234	0.32227	-0.0006
H	-3.92	-2.2766	0.00057
O	0.81901	-0.9057	-0.0002
H	0.2951	1.06236	0.00005

12

Glyceraldehyde

C	0	0	0
C	-1.1337	-0.745	-0.7377
O	-2.3569	-0.0728	-0.5398
H	-2.1822	0.85682	-0.769
H	-0.8741	-0.8128	-1.8073
H	-1.2537	-1.7612	-0.3465
C	1.34108	-0.6499	-0.2523
O	2.22524	-0.0651	-0.8461
H	1.4748	-1.6892	0.10807
O	0.01287	1.34526	-0.4266
H	0.86508	1.46791	-0.8902
H	-0.2153	-0.0409	1.07987

8

Glycolaldehyde

C	0	0	0
O	-1.1314	-0.8504	-1E-06
H	-1.9282	-0.3004	-7E-05
C	1.23959	-0.8796	-6E-06
H	1.0241	-1.9703	-6E-06
O	2.3657	-0.4394	-1E-05
H	0.04576	0.65249	-0.8874
H	0.04576	0.65246	0.88744

9

Pyruvaldehyde

C	0	0	0
C	-0.3373	-1.4681	-0.0002
O	0.4742	-2.3733	-0.0003
C	-1.8262	-1.8451	0.00044
H	-2.0009	-2.9412	0.00166
O	-2.7183	-1.0284	-0.0004
H	-0.4488	0.4895	-0.8722
H	-0.4341	0.4848	0.88238
H	1.08298	0.13312	-0.008

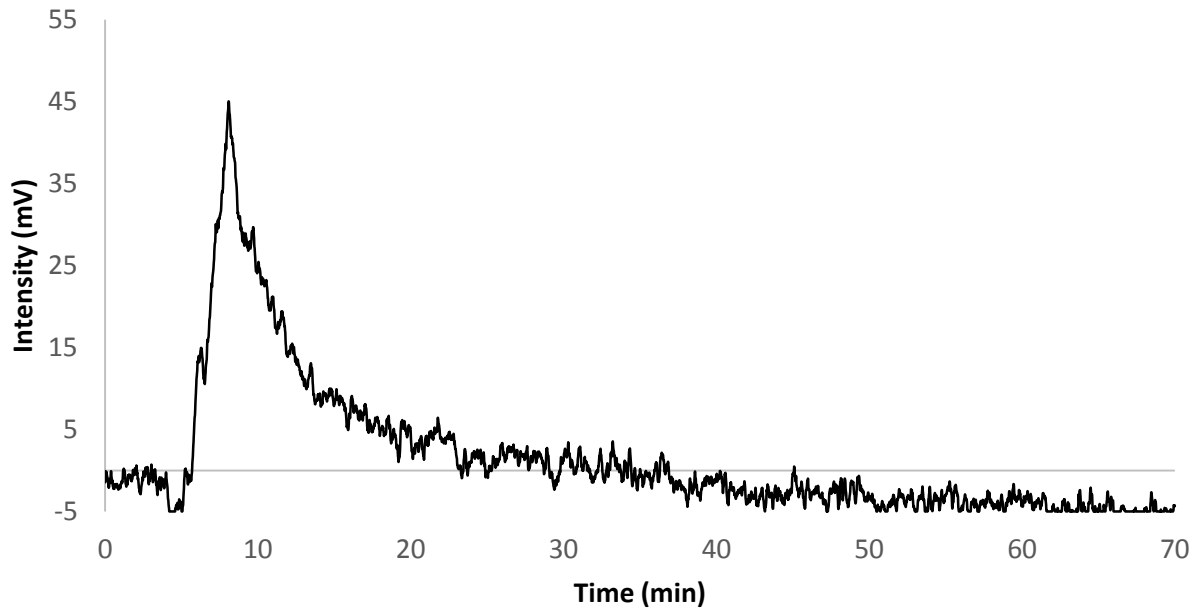
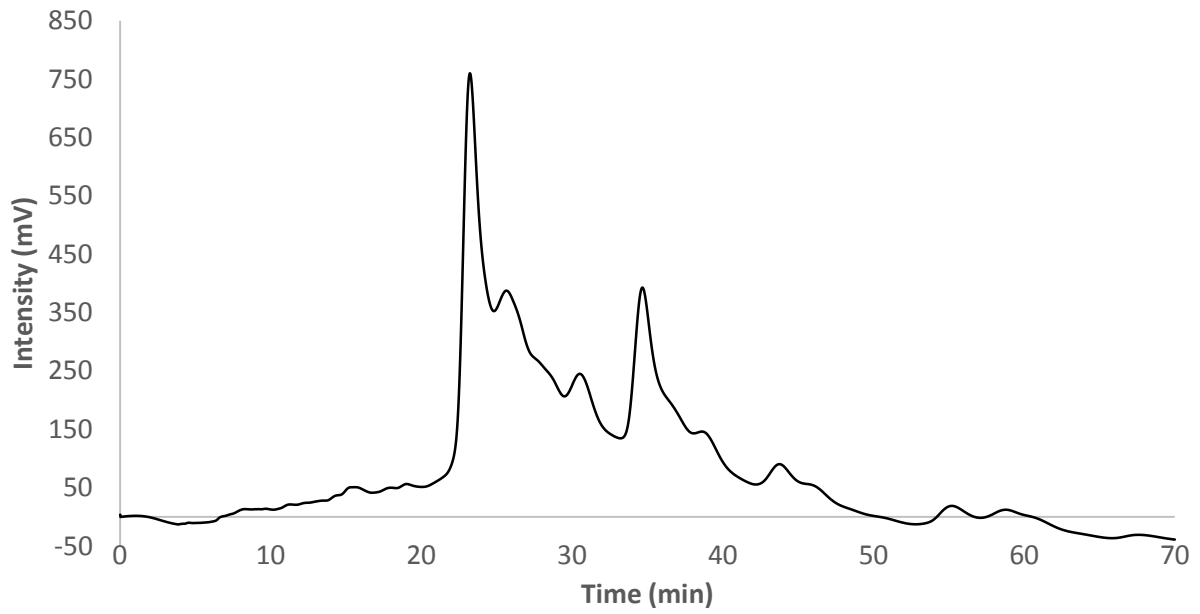
20

Xylose

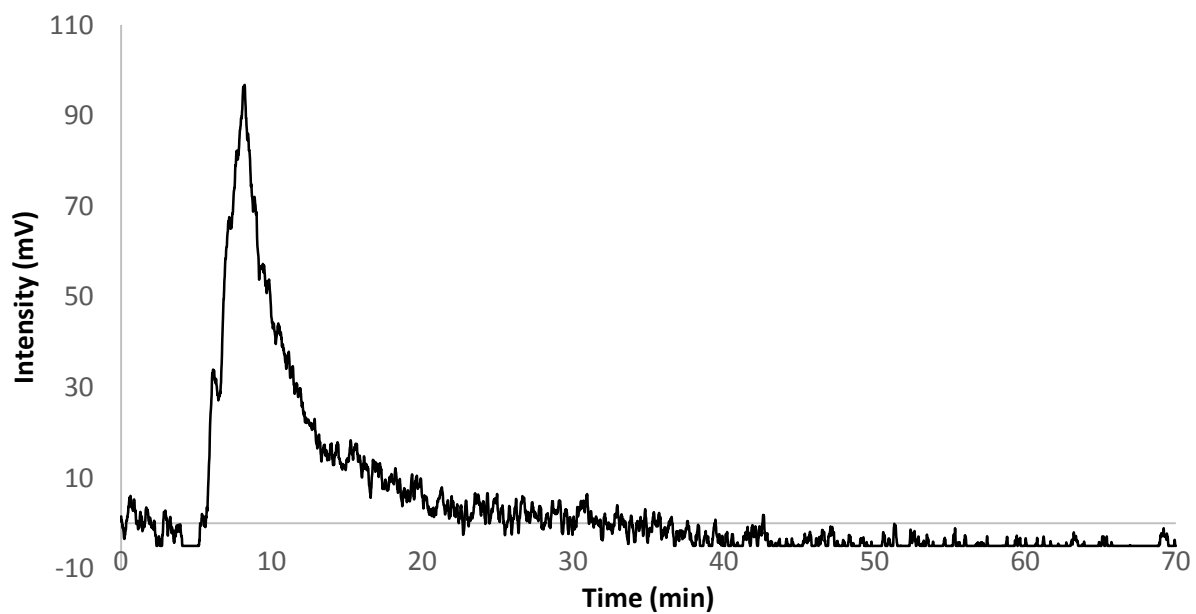
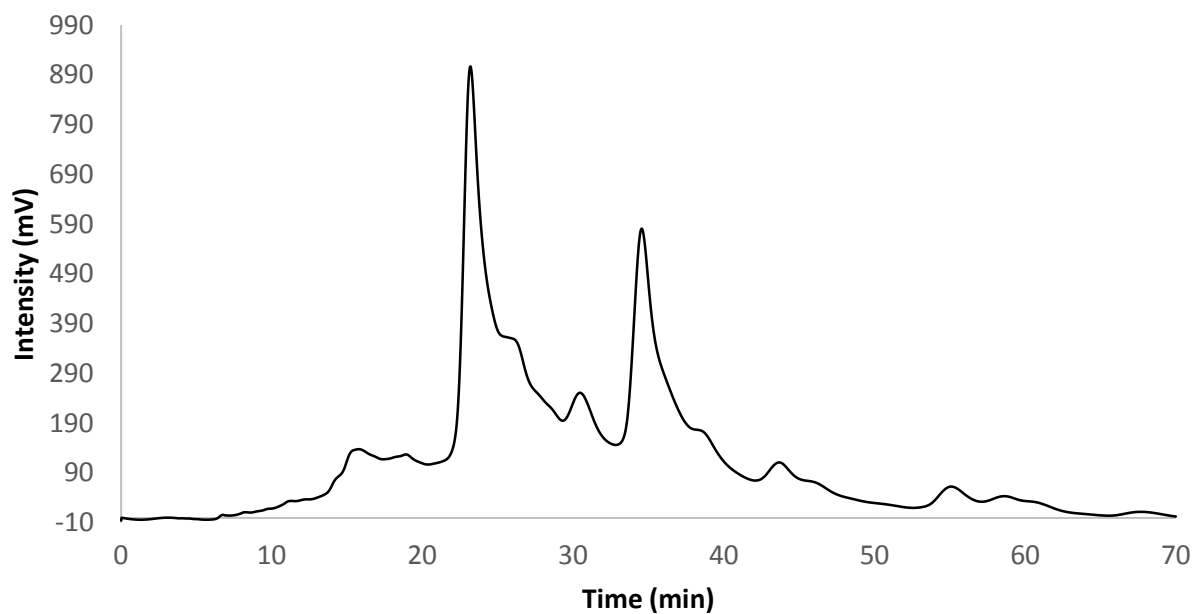
C	0	0	0
O	-1.3652	0.08767	-0.4134
C	-2.0246	1.23374	0.0916
O	-3.3635	1.2002	-0.32
H	-3.3555	0.99062	-1.2704
C	-1.3234	2.50685	-0.404
C	0.14167	2.49031	0.00923
C	0.80598	1.20857	-0.4863
O	2.12758	1.08456	0.00879
H	2.55907	1.93798	-0.1648
H	0.79912	1.22217	-1.5883
O	0.87193	3.5875	-0.5258
H	0.40732	4.39406	-0.2485
H	0.19186	2.50278	1.111
O	-1.9185	3.67267	0.14639
H	-2.8742	3.59918	-0.0157
H	-1.3821	2.51702	-1.5063
H	-2.0477	1.22571	1.19186
H	0.06972	-0.0676	1.09655
H	0.39374	-0.9247	-0.4268

### 9.1.3 Raw Liquid HPLC Chromatograms

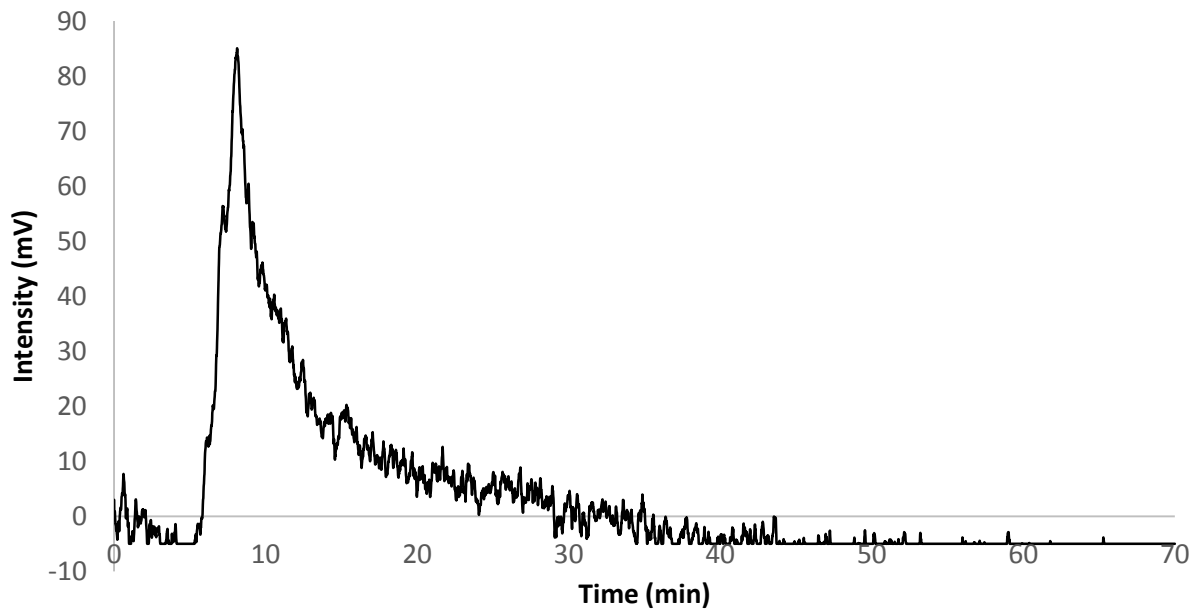
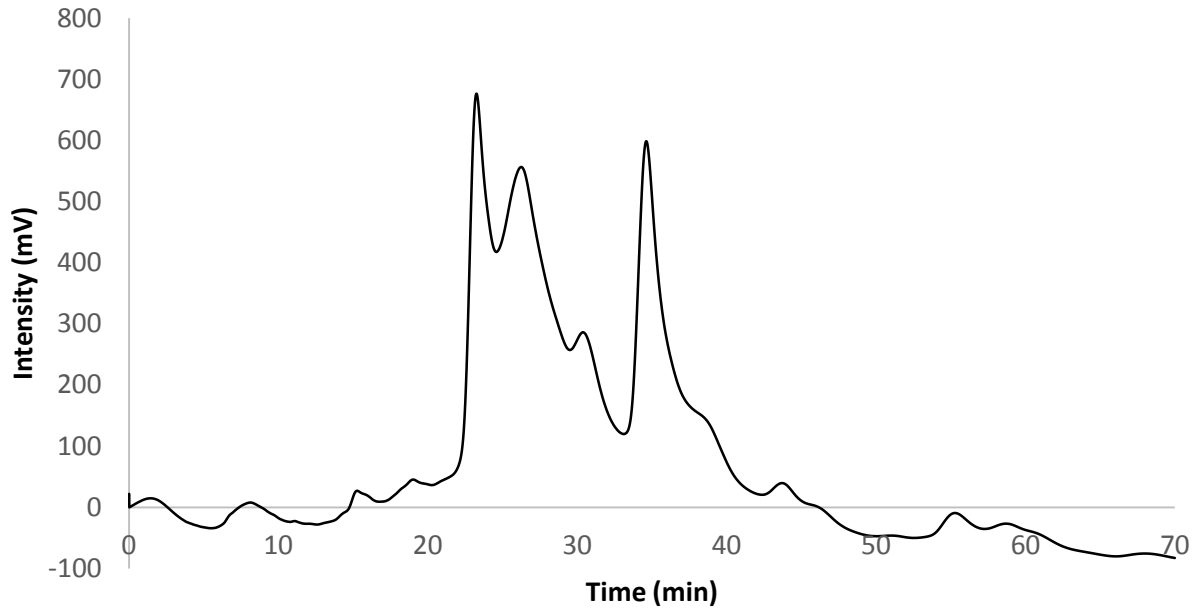
UV/Vis and ELSD chromatograms for 106-150  $\mu\text{m}$  #1:



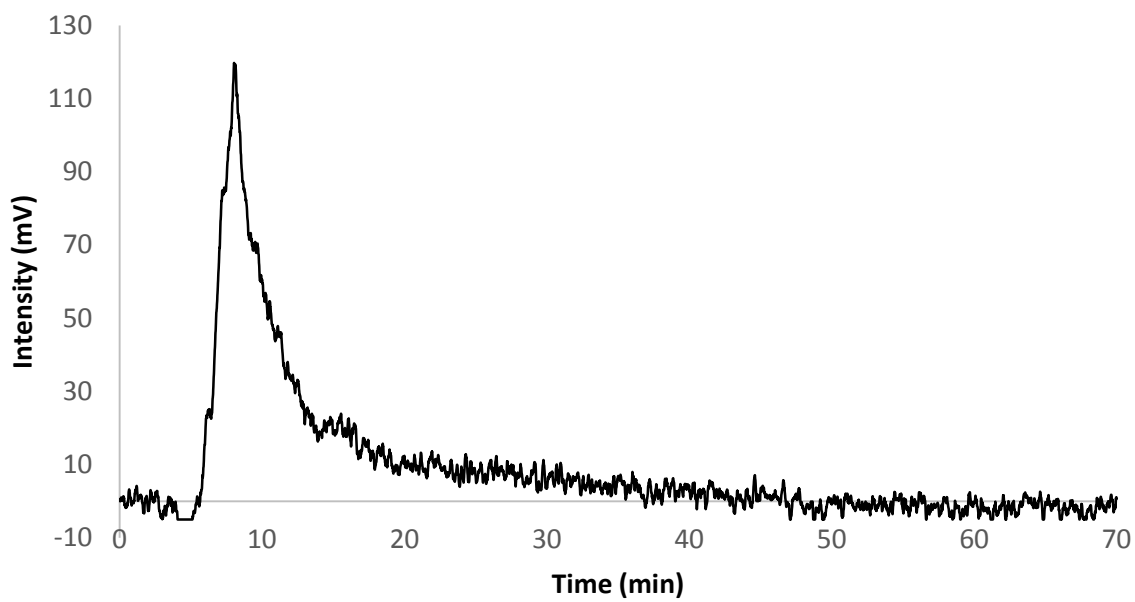
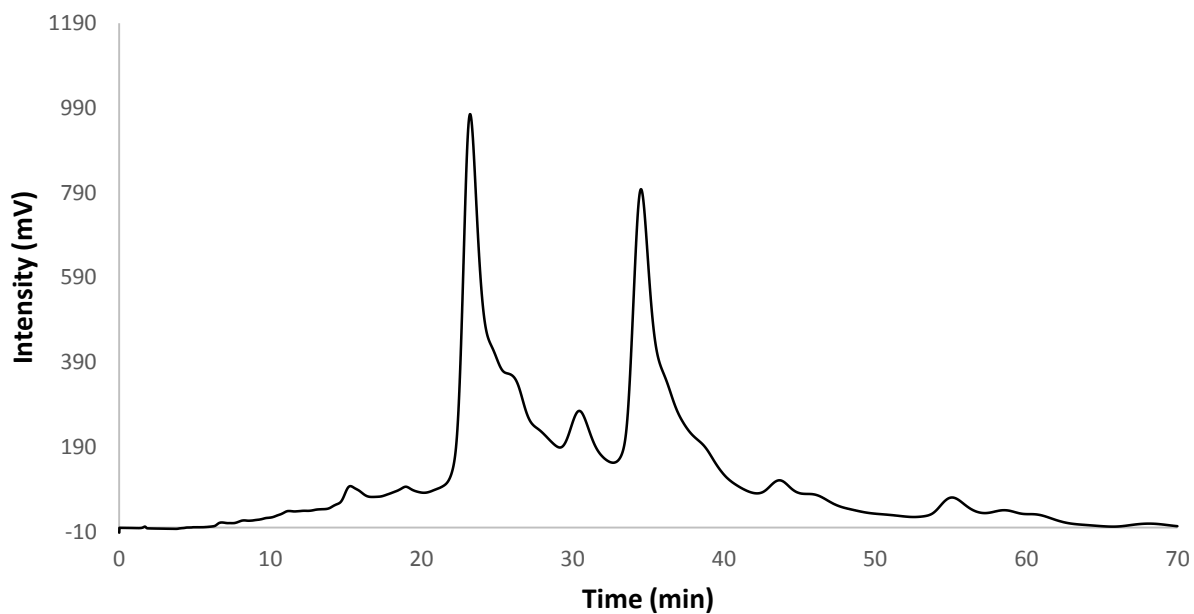
UV/Vis and ELSD chromatograms for 106-150  $\mu\text{m}$  #2:



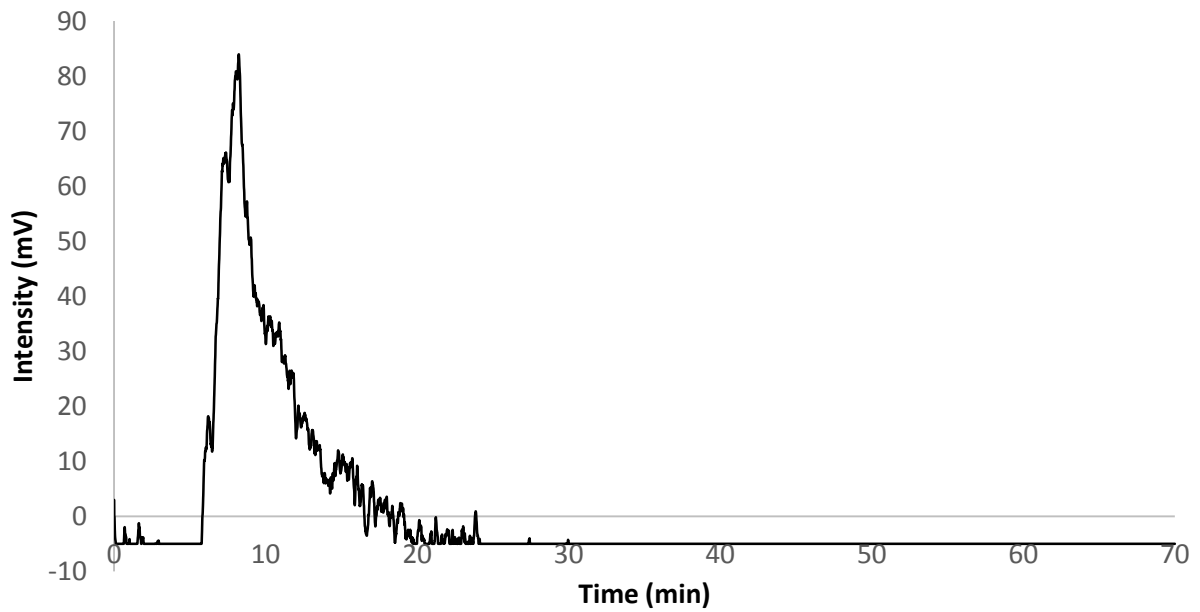
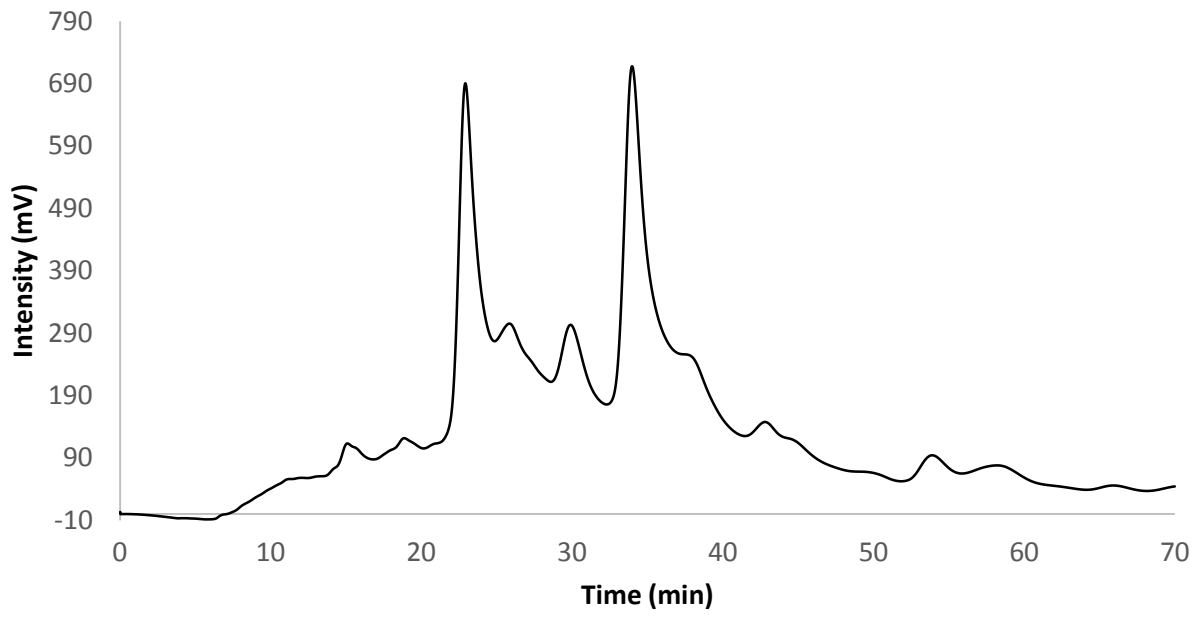
UV/Vis and ELSD chromatograms for 212-300  $\mu\text{m}$  #1:



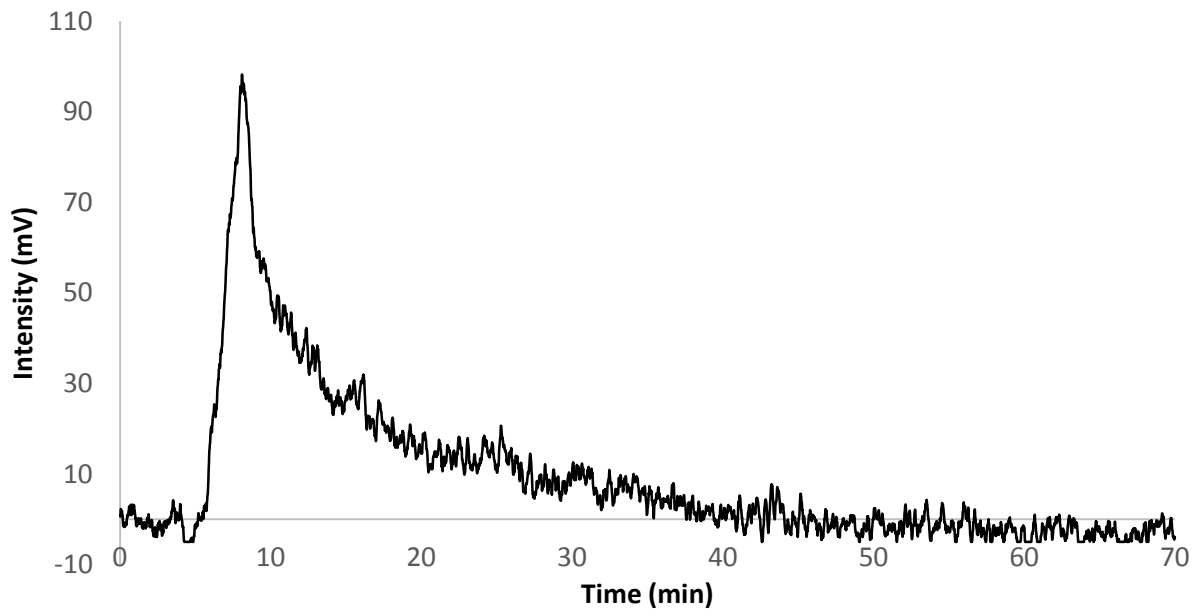
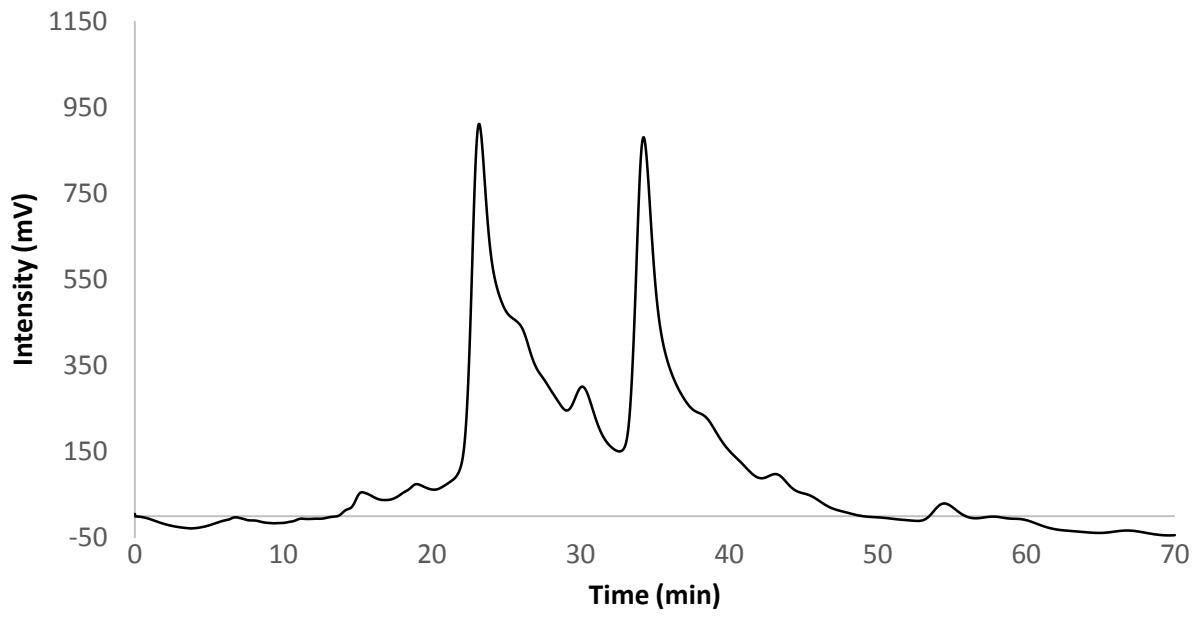
UV/Vis and ELSD chromatograms for 212-300  $\mu\text{m}$  #2:



UV/Vis and ELSD chromatograms for 1680-2000  $\mu\text{m}$  #1:

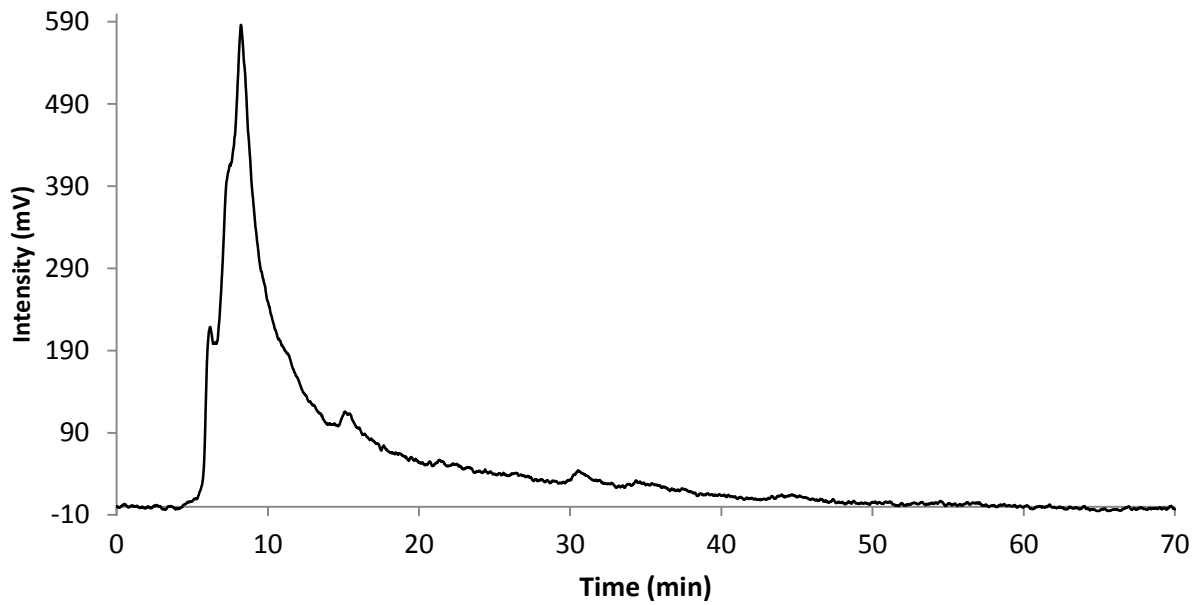
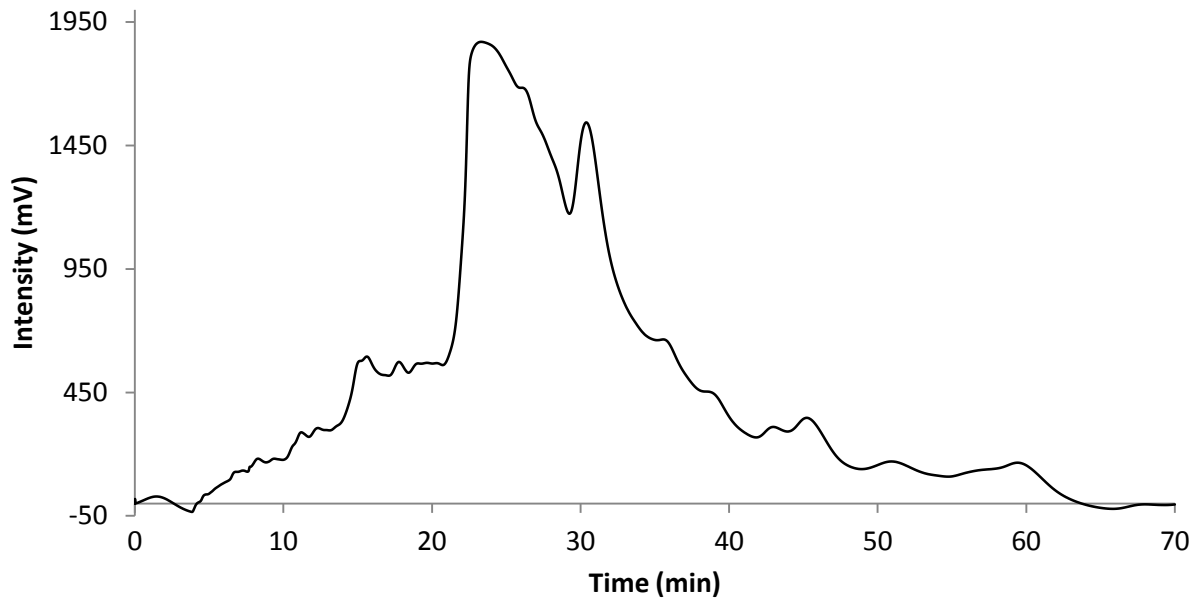


UV/Vis and ELSD chromatograms for 1680-2000  $\mu\text{m}$  #2:

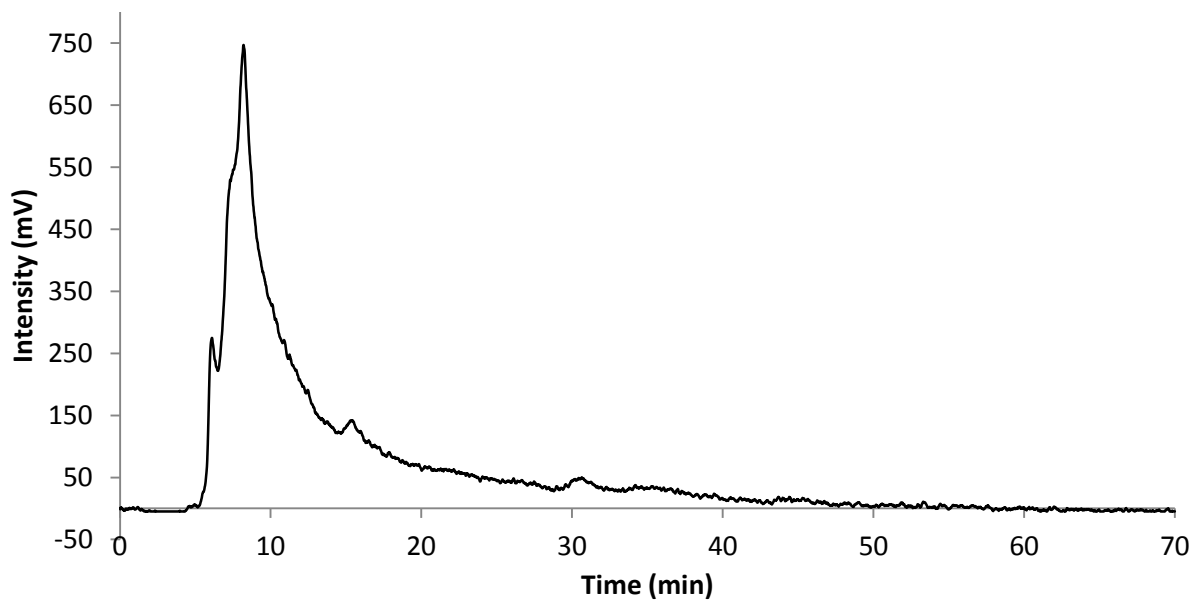
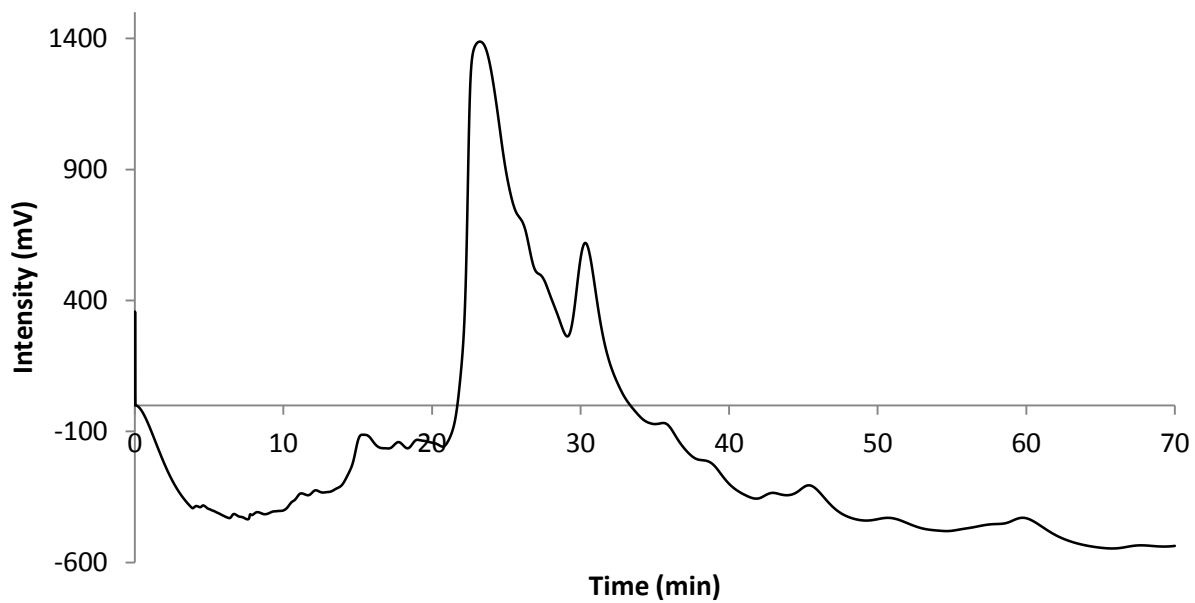


### 9.1.4 Concentrated Liquid HPLC Chromatograms

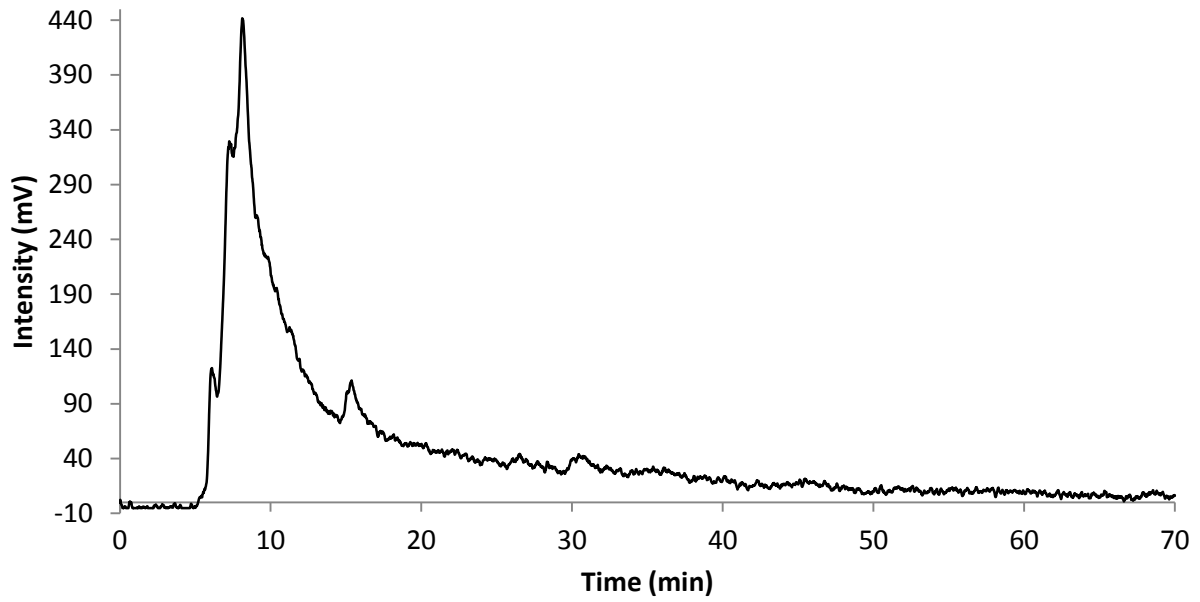
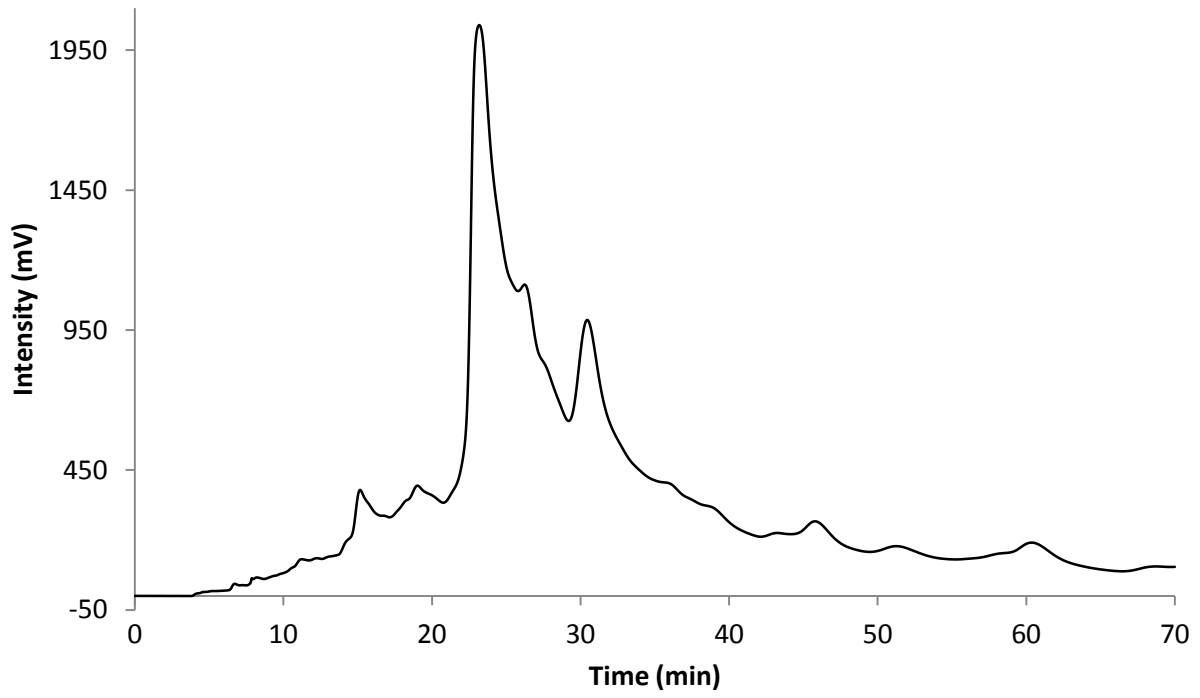
UV/Vis and ELSD chromatograms for 106-150  $\mu\text{m}$  #1:



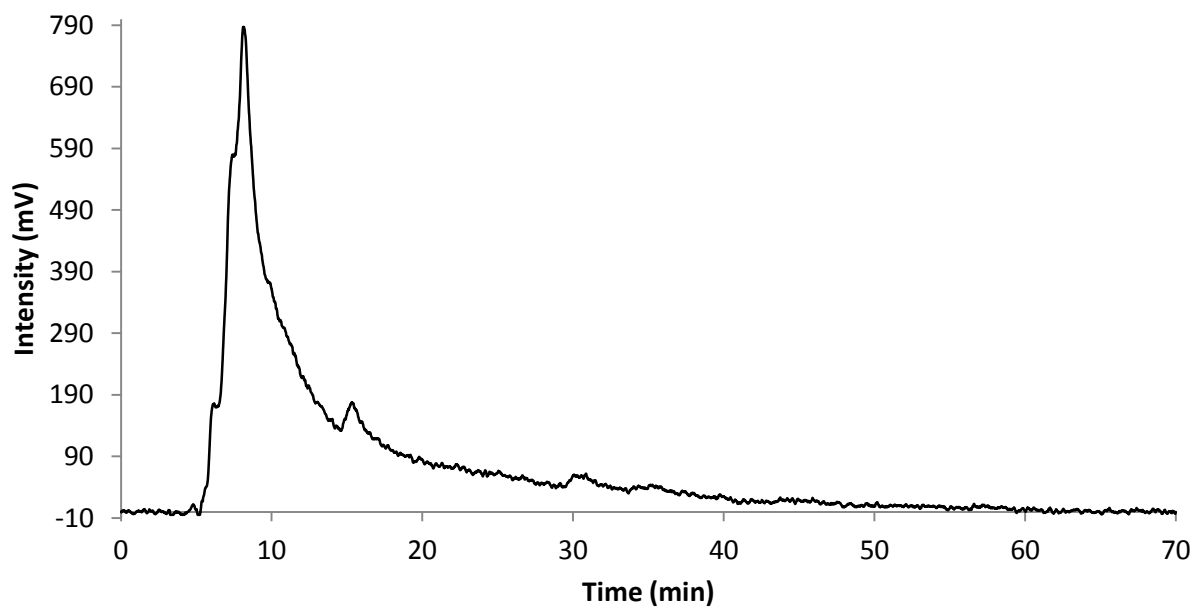
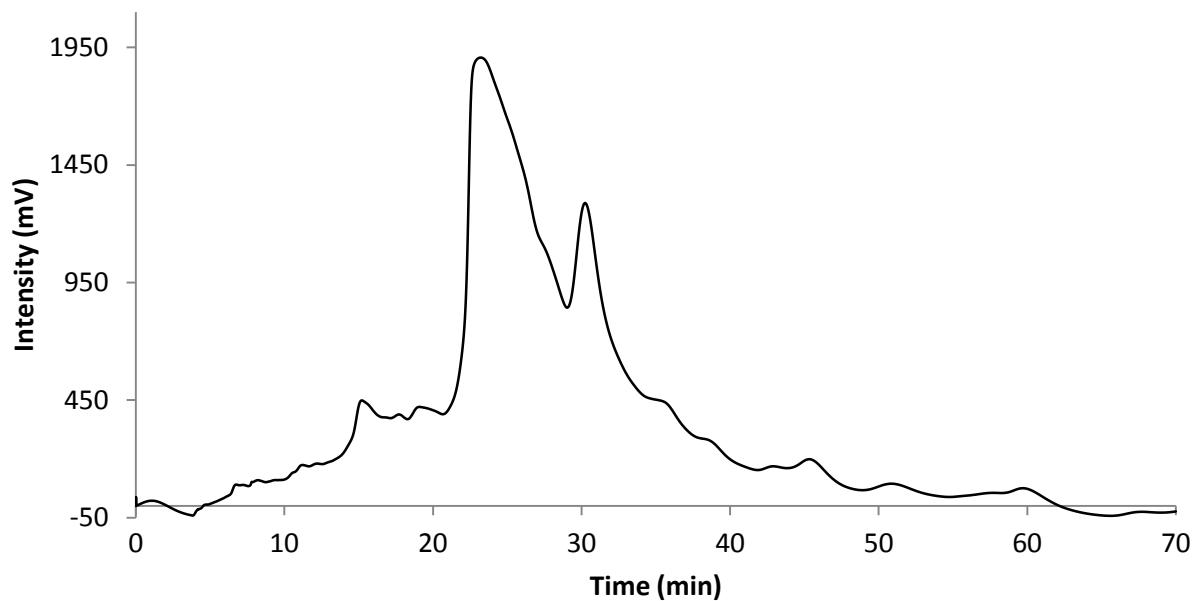
UV/Vis and ELSD chromatograms for 106-150  $\mu\text{m}$  #2:



UV/Vis and ELSD chromatograms for 212-300  $\mu\text{m}$  #1:



UV/Vis and ELSD chromatograms for 212-300  $\mu\text{m}$  #2:



UV/Vis and ELSD chromatograms for 1680-2000  $\mu\text{m}$  #2:

